PRODEX-ESA-SSTC Contract No. 170724

The Charged Particle Detector (CPD) on the ØRSTED satellite : description and evaluation

Technical Report A
(version 1.0)

M. Cyamukungu (UCL-FYNU)
Gh. Grégoire (UCL-FYNU)
J. Lemaire (UCL-ASTR/BISA)
P. Stauning (DMI)

Louvain-la-Neuve, September 1997

Contents

Preface

It was in May 1993, at the NATO Advanced research Workshop in Norway, that the official announcement of the future ØRSTED mission was made to the space physics community. It is there also that Peter Stauning (Danish Meteorological Institute, Copenhagen), proposed to J. Lemaire (BISA, Brussels), to become Co-I on the Charged Particle Detector (CPD) which was planned to be part of the payload ØRSTED satellite.

The cooperation agreement between the Danish Meteorological Institute (DMI) and the Institute for Space Aeronomy (BISA) was formalized during a couple of visits and meetings in Brussels and Copenhagen.

The main scientific objective of the ØRSTED mission is to survey the geomagnetic field distribution with unprecedented accuracy. An additional objective of this mission is to use this low altitude platform to study the flux of energetic magnetospheric particles precipitated in the atmosphere at auroral latitudes as well as in the region of the South Atlantic Anomaly where the mirror points of trapped radiation belt particles have their minimum minimorum altitudes. It is the observations in this region of the South Atlantic Anomaly that BISA is mostly interested in. Comparison will be undertaken between the ØRSTED observations, the results predicted from existing empirical models for the radiation belt environment and observations from other spacecraft like SAMPEX, UARS and the MIR station.

The CPD has been calibrated at GSFC (Greenbelt, Ma), in electron and proton beams of different energies. The results of this calibration were made available to BISA and to the Institute for Nuclear Physics (FYNU) of the Universite Catholique de Louvain (UCL) where software calibrations have been performed using the GEANT / Monte-Carlo simulation program to cross check the hardware calibration.

The response of the detector in the radiation belt environment has also been evaluated at UCL/FYNU using GEANT and energy spectra obtained from existing environment models available at BISA.

The present Technical Note contains the description of the CPD and of its installation on the ØRSTED satellite. The results of the hardware calibration are summarized and compared to those of Monte Carlo simulations.

This preliminary study constitute a part of the CPD User Manual, it will be useful for the analysis and interpretation of the CPD data when they will become available.

Useful addresses

Belgian Institute for Space Aeronomy
3 avenue Circulaire, B-1180 Brussels, Belgium
FAX: 32 2 374 8423 TEL: 32 2 374 8121

Danish Meteorological Institute
Solar-Terrestrial Physics Division
Lyngbyvej 100,
DK-2100 Copenhagen, Denmark
FAX: 45 39 27 10 80 TEL: 45 39 15 75 00

ESA/ESTEC - PRODEX
P.O. Box 299
Keplerlaan 1, 2200 AG Noordwijk, The Netherlands
FAX: 31 71 565 4693 TEL: 31 71 565 4350

Institut de Physique Nucléaire
Université Catholique de Louvain
2, chemin du Cyclotron,
B-1348 Louvain-La-Neuve, Belgium
FAX: 32 10 45 2183 TEL: 32 2 47 3273

SSTC
Rue de la Science, 8
1000 Brussels, Belgium
FAX: 32 2 230 59 12 TEL: 32 2 238 34 11

Useful e-mail adresses and phone numbers

Eigil Friis-Christensen	TEL: 45 39 15 75 00	Eigil.Friis@dmi.dk
Torsten Neubert	TEL: 45 39 15 75 00	neubert@dmi.min.dk
Peter Stauning	TEL: 45 39 15 74 73	pst@dmi.dk
Mathias Cyamukungu	TEL: 32 10 47 3213	cyam@fynu.ucl.ac.be
Ghislain Grégoire	TEL: 32 10 47 3216	gregoire@fynu.ucl.ac.be
Joseph Lemaire	TEL: 32 2 373 0407	joseph.lemaire@bira-iasb.oma.be
Daniel Heynderickx	TEL: 32 2 373 0417	daniel.heynderickx@bira-iasb.oma.be
Michel Kruglanski	TEL: 32 2 373 0417	michel.kruglanski@bira-iasb.oma.be
Carlos Lippens	TEL: 32 2 373 0383	carlos.lippens@bira-iasb.oma.be
Viviane Pierrard	TEL: 32 2 373 0416	viviane.pierrard@bira-iasb.oma.be
H. Olthof (PRODEX)	TEL: 31 71 565 46 93	
J. Wautrequin (SSTC)	TEL: 32 2 238 34 11	
J.W. Bernard (SSTC)	TEL: 32 2 238 35 83	
M.C. Limbourg (SSTC)	TEL: 32 2 238 34 11	

Acknowledgments

The authors of this Technical Report wish to thank Dr. P. Stauning and the OERSTED project manager, Dr. E. Friis-Christiansen for their offer to share the data of the Charged Particle Detector.

They would like to thank the Service des Affaires Scientifiques Techniques et Culturelles, for the financial support and the delegates of PRODEX for their cooperation and support with respect to administrative matters related to this project.

The authors are particularly grateful to Dr. D. Heynderickx, Dr. M. Kruglanski, Dr. C. Lippens and Dr. V. Pierrard (BISA, Brussels) for their advise and collaboration during the preparation of this document. All the BISA team is acknowledged for the fruitful access to the UNIRAD Library developed at BISA and the Space Environment Information System (SPENVIS). The useful discussions the authors had with P. Davidsen (CRI, Copenhagen) were much appreciated.

Dr. D.S. Evans (NOAA, Boulder) has sent to us plots of auroral electron spectra and contributed fruitful comments, which spurred us on to search for suitable solutions to the pulse pile-up problem.

Introduction

Detector arrays are used in space applications to measure energy spectra of different kinds of particles. The SSJ*/4 dosimeter on the DMSP [1], the SFD on EQUATOR-S [2], the REM detector on STRV-1B and MIR [3] are examples of very light weight detector arrays which flew or are planned to fly on satellites to detect the particle fluxes in the space environment.

The ideal detector would have a specific and dedicated channel for each kind of particle within a well defined energy range. During the Data Analysis phase, the informations contained in all the channels would be combined and lead to particle spectra, assuming that the detector characteristics (a.o the response to particle spectra) are precisely known.

A real detector however has to cope with many constraints giving rise to situations where much more delicate analysis is compulsory in order to extract the true spectra.

The Charged Particle Detector (CPD) instrument was designed by P. Stauning at the Danish Meteorological Institute. It will be used to measure the high energy particle (electrons, protons and α-particles) fluxes on ØRSTED satellite orbit. This document contains a detailed simulation of its functions, as well as the methods to extract spectra from its raw data.

In Chapter 1, the CPD is decribed with reference, when needed, to the more detailed document in Appendix. The accomodation of the instrument on the ØRSTED satellite is shown, along with the simulation model of the whole setup.

The CPD characteristics and the numerical calibration are presented in Chapter 2. The detection efficiency for each channel and particle are shown; finally the response of the detector to space environment radiation is presented.

In Chapter 3, the Data Analysis protocol is described and illustrated by several examples as close as possible to conditions likely to be encountered on ØRSTED orbit.

A final chapter summarizes the main results of this study and outlines the tasks to be undertaken after a successful launch of the ØRSTED satellite.

Chapter 1

The ØRSTED/CPD Instrument

The Charged Particle Detector (CPD) is aimed to detect electrons, protons and α-particles within an energy range which depends on the Signal to Noise ratio on ØRSTED orbit. A complete description of the CPD experiment can be found in Appendix A, along with its scientific background. We, herewith quote from Appendix A, the main purposes of the CPD experiment, since they will be the leading criteria all along the CPD performance study. The CPD was designed to:

- Provide measurements of the energetic particle radiation in the upper polar atmosphere to be combined with absorption data from imaging riometer (relative ionospheric opacity - meter) installations on the ground in order to detect the dynamical features of polar and auroral particle precipitation events.
- Conduct monitoring of the level of solar-geophysical activity during events, like major solar flares and geomagnetic storms, where intense and variable high-energy particle radiation may occur.
- Monitor the long-term high-energy particle radiation dose at the satellite for investigations of possible radiation damages on other on-board experiments and systems.

Section 1.1 contains a summary of the CPD mechanical assembly. In Section 1.2, the ØRSTED mission and orbit analysis are presented. The CPD experiment is described within the general frame of ØRSTED mission [4]. The accomodation of the CPD on the satellite and the ØRSTED GEANT model are presented in Section 1.3 and Section 1.4, respectively.

1.1 Mechanical details

The CPD mechanical assembly is made of six 3.5 cm diameter and 4.7 cm height detector units similar to the one shown in Figure 1.1. These units are accomodated in a 260 x 175 x 55 mm^3 aluminum box shown in Figure 1.2 (see also Figure 6 in Appendix A). The

dimensions of all detector subunits are given in Appendix A. The specific features of these subunits may be better grasped from the description summarized in Table 2.1.

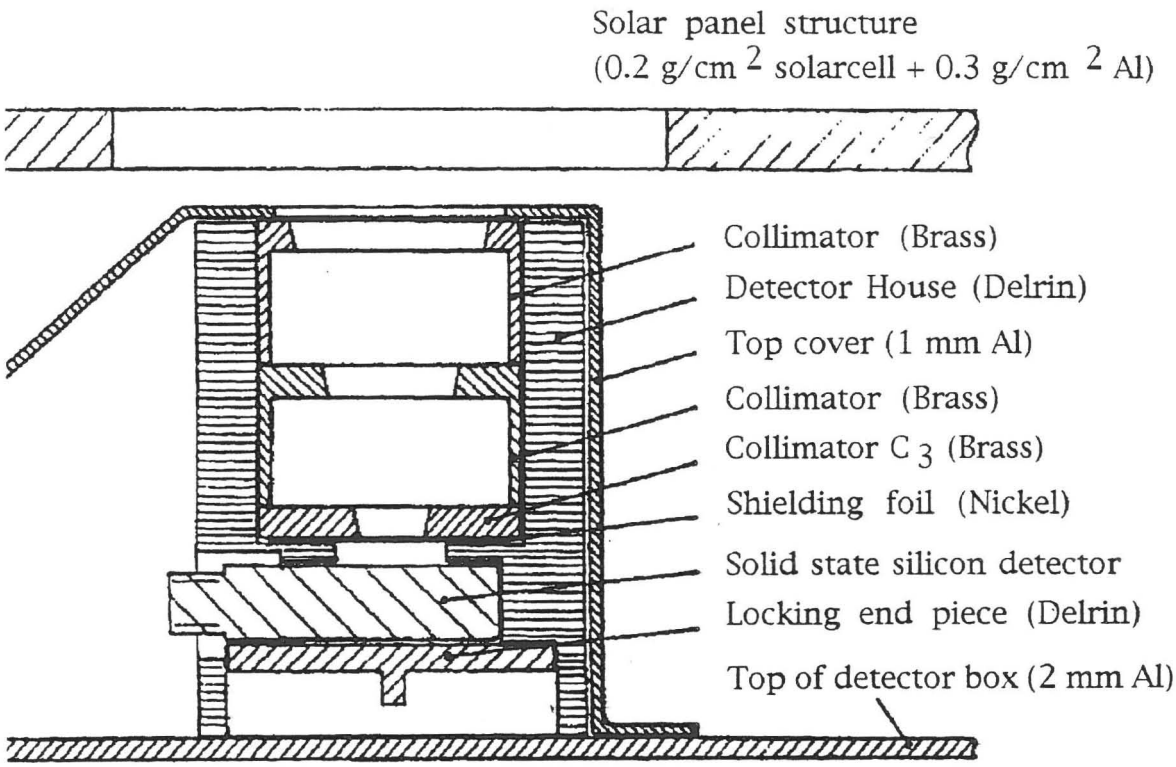

Figure 1.1: General layout of the Charged Particle Detectors.

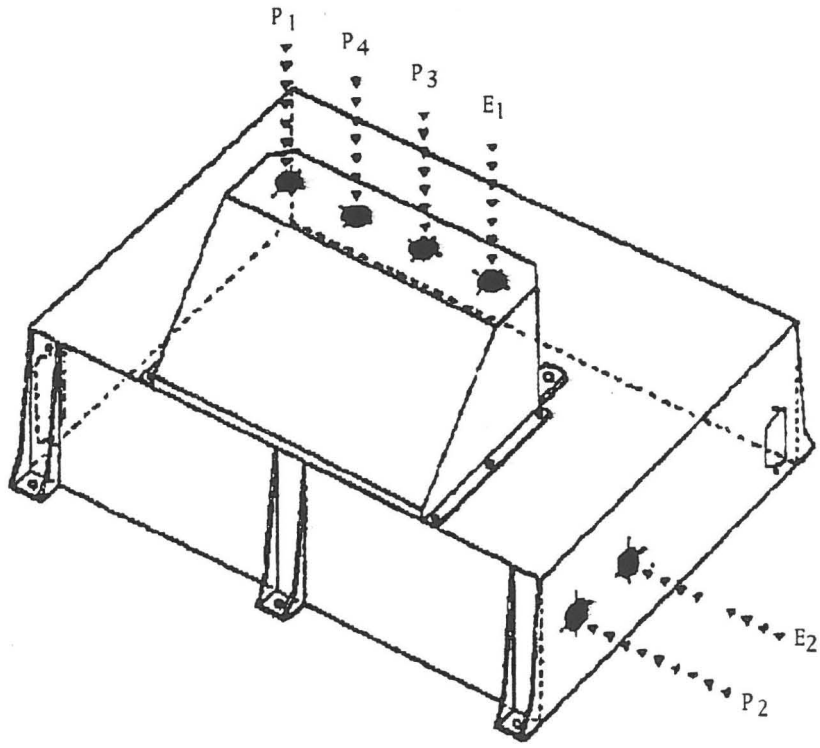

Figure 1.2: The CPD box and detector location.

1.2 Mission and orbit analysis

See Appendix B and Reference [4].

1.3 Accomodation of the CPD detector on the satellite

The ØRSTED satellite is well described in Appendix C. A picture of the satellite, showing the CPD accomodation is given in Figure 1.3.

The interior of the ØRSTED satellite is partly shown in Figure 1.4. As will be seen in Chapter 2, the radiation background level in the CPD will be determined by the filling factor of the satellite box. Figure 1.4 suggests that background radiation coming from the bottom is not likely to reach the CPD sensitive elements.

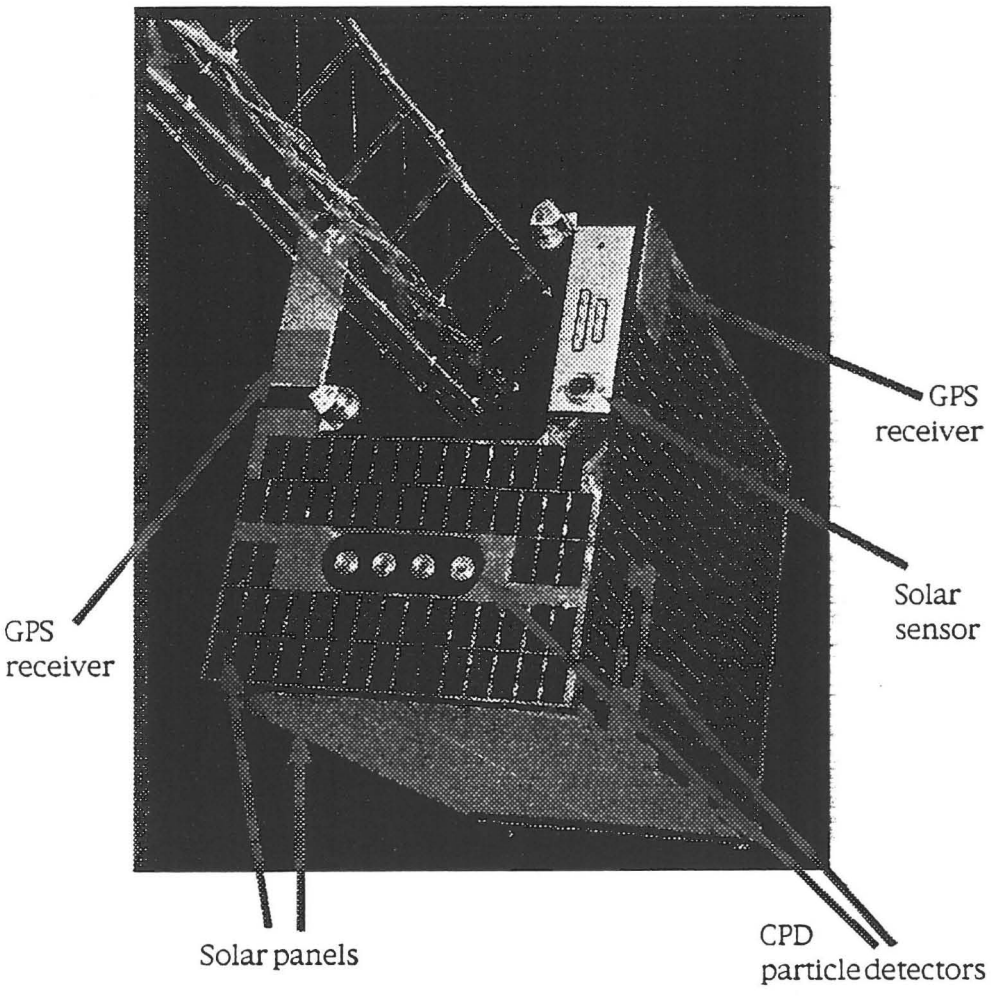

Figure 1.3: Accomodation of the CPD detector on the satellite.

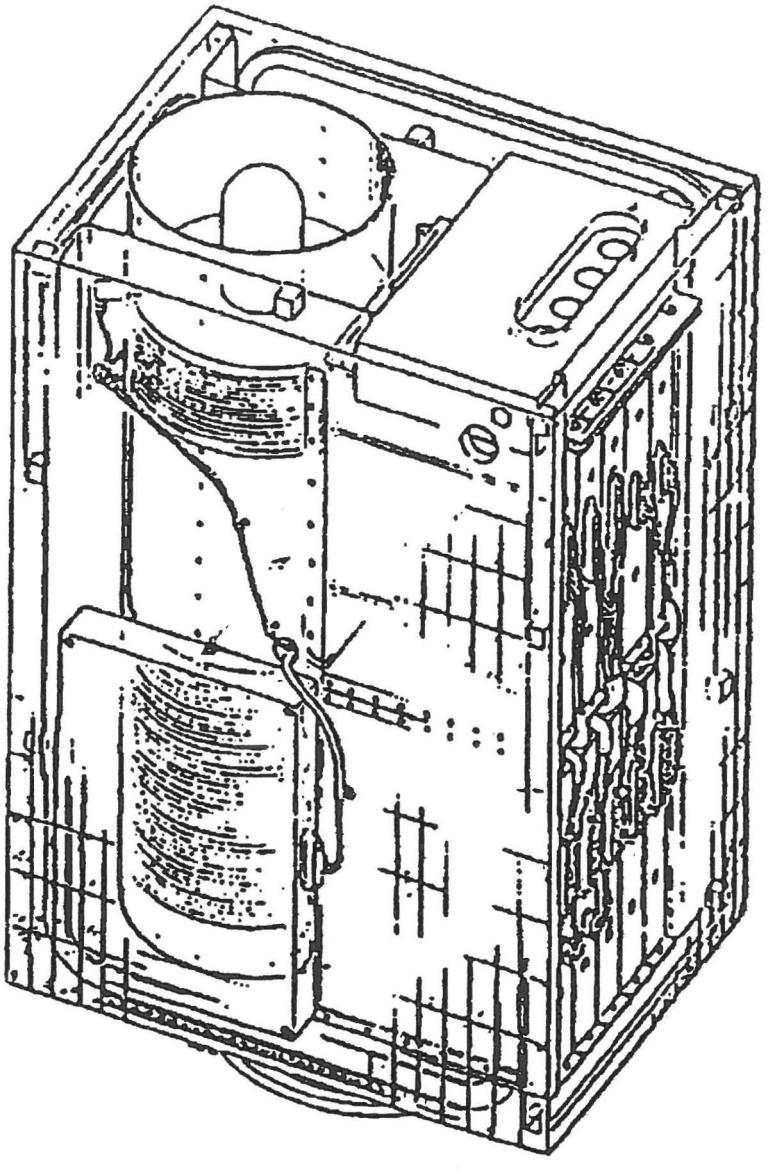

Figure 1.4: Satellite main body and CPD surrounding elements.

1.4 The GEANT model of the Charged Particle Detector

The ØRSTED satellite model is shown in Figure 1.5 to 1.8. The CPD components were modelized following a detailed plan of the whole detector. The CPD box is accomodated inside the satellite body (of outer dimensions 72 x 45 x 34 cm^3) made of 0.376 mm thick GaAs solar cells on a 1 mm thick aluminum plate backing. No other information than Figure 1.3 and 1.4 was available about the components inside ØRSTED, thus we consider that the CPD accomodation to the satellite modelized herein could still be refined. As part of the needed refinements, the characterization of the shielding efficiency of the CPD surrounding elements is of paramount importance. Indeed, as stated above, these elements could contribute to reduce the radiation background level.

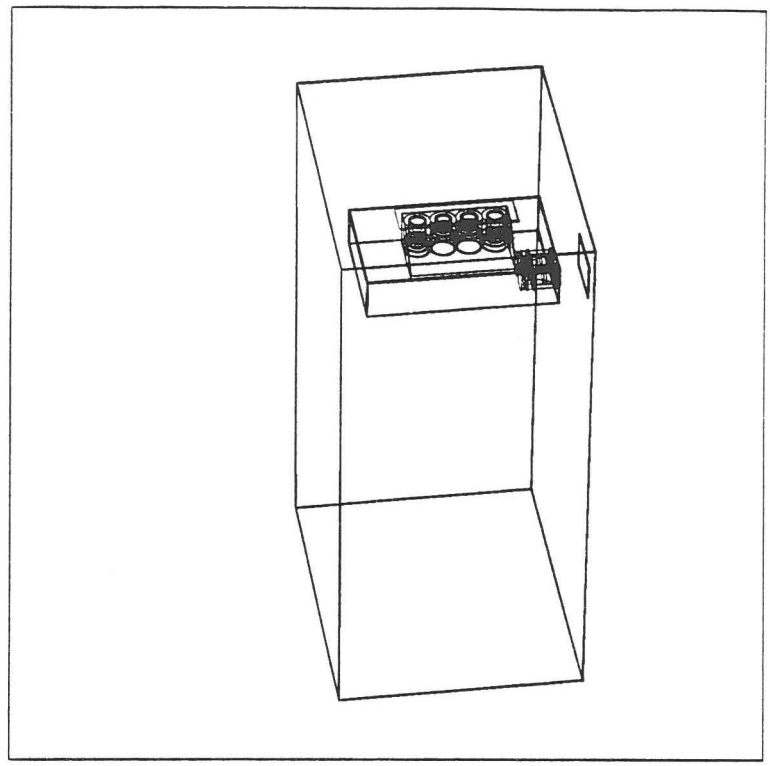

Figure 1.5: The ØRSTED model used in numerical simulation with GEANT 3.21.

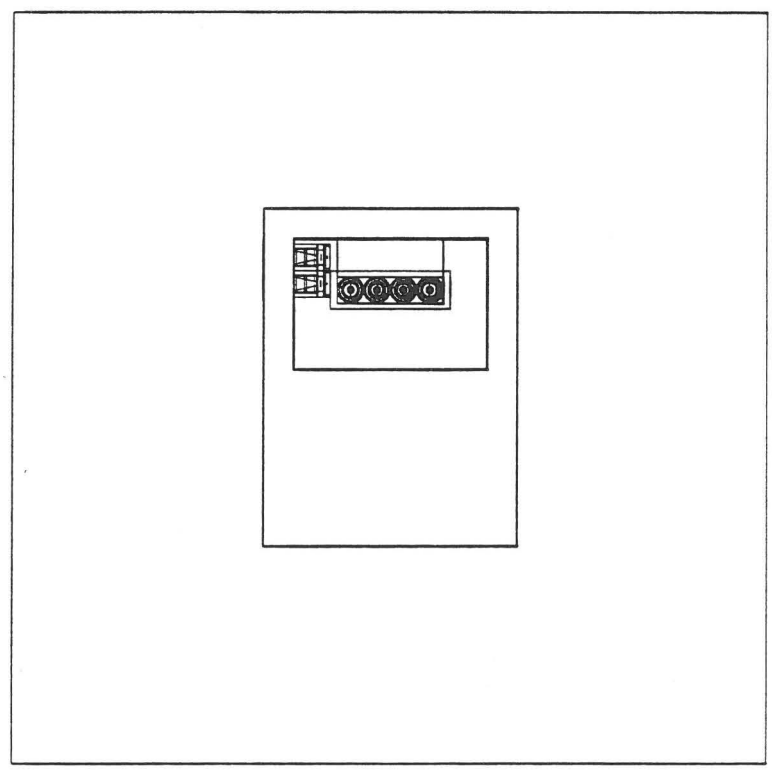

Figure 1.6: ØRSTED model: projected view along the boom axis.

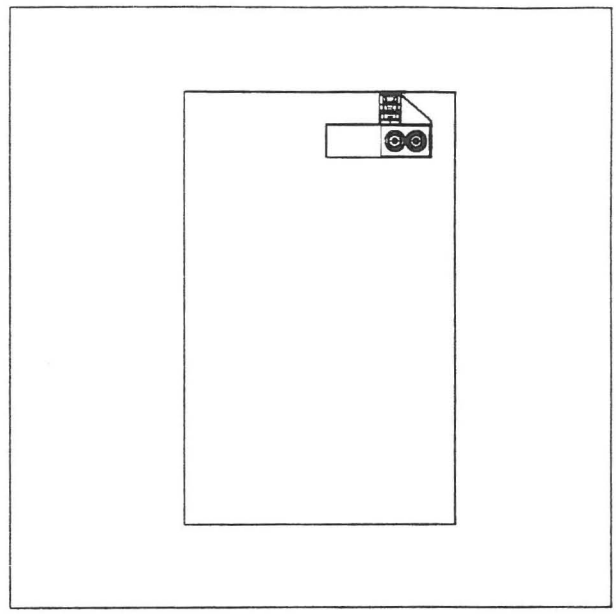

Figure 1.7: ØRSTED model: projected view along the horizontal detector symmetry axis.

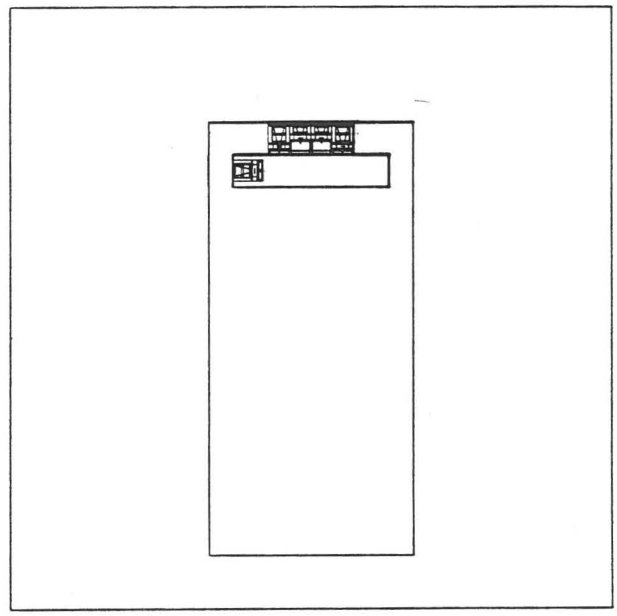

Figure 1.8: ØRSTED model: projected view along the perpendicular to the detector symmetry axes.

Chapter 2

The simulation of the CPD

The CPD properties were determined using the mechanical model decribed in Chapter 1. Some of these properties (described in Section 2.1) are not ajustable anymore once the CPD hardware is definitely frozen.
The others will be tuned at calibration time to match the experimenter's requirements. They are summarized in Section 2.2. In particular, the detection efficiency, which is the basis of all count rate predictions is given in Subsection 2.2.2. Table 2.1 summarizes a large number of both fixed and ajustable CPD characteristics. The Section 2.4 reports the counting rate based on the detection efficiency and the space radiation characteristics.

2.1 The CPD fixed characteristics

2.1.1 View direction

As stated in Chapter 1, the six detectors which compose the CPD are oriented either towards the up direction (90°, i.e. looking "along" the boom direction) or horizontally oriented (0°, i.e. perpendicular to the boom direction).
The field of view (F.O.V.) half angle are 20.5^o for detector units P1, P2, E1 and E2 and 33.5^o for detectors P3 and P4. These F.O.V. are determined taking into account the fact that the collimators are not deep enough to shield the outer rims of the sensitive detector surfaces.
The aperture values given in Table 2.1 refer to the aperture of the last collimator set before the detector sensitive element, whereas the actual aperture involves the whole sensitive surface of the detectors.

2.1.2 The Geometrical Factor (GF)

The geometrical factor values in Table 2.1 are valid for particles of energy above the thresholds and below the energies at which the collimators are no longer efficient. This point is illustrated in Figure 2.1, where the count rates per unit flux (i.e. the GF) are plotted as a function of particle energy. One can see that the GF is a well defined constant for electrons penetrating in P1 and E1 with an energy between 0.3 MeV and 1.5 MeV, whereas the GF is still increasing at electron energy equal to 5 MeV. It never reaches a constant value for detector P3 and P4 due to straggling of electrons crossing the 1 mm thick aluminum and copper entrance windows.
The geometrical factor of protons (see Figure 2.2) is constant up to 10 MeV in P1 and E1. At this energy, a significant number of protons begin reaching the sensitive element through the collimator C3. This number increases with the proton energy, up to 41 MeV, - the proton energy value at which they completely traverse the 3 mm thick brass plate -, making it totally inefficient. At this energy, the GF value equals the one obtained when no collimator is installed between the detector entrance and the detector sensitive element. The protons thresholds for P3 and P4 are $\sim$ 50 MeV and $\sim$ 90 MeV, respectively, well above the value (41 MeV) for which the proton flux may be considered as collimated. This fact is reflected in the GF of P3 and P4 for protons: the value (0.25 cm^2 sr) is exactly the same as the one obtained for a no collimated proton beam in P3 and P4.

The general characteristics of the GF of P1, P3, P4 and E1 for α-particles (see Figure 2.3) are very similar to the protons one. The Figures 2.4, 2.5 and 2.6 show the asymptotic variation of the GF for detectors P1 and E1 and for the electrons, protons and α-particles, respectively.

The difference between the GF mean values given herewith and the values in Appendix A are due to the differences in aperture used: in Appendix A, the aperture value of 0.20 cm^2 (corresponding to the collimator aperture) was used, whereas 0.50 cm^2 corresponding to the whole sensitive area is used herein.

2.1.3 Detector type

The detector type referred to as A and B are ORTEC manufactured U-011-050-300-T and B-016-050-1000-T respectively. A-type detector are 300μm thick silicon and B-type are 1000μm thick silicon, both with sensitive area equal to 50 mm^2.

2.1.4 Entrance windows and threshold energies

The entrance windows are made of a 0.75μm thick nickel foil for P1, P2, E1 and E2 and establish threshold energies for those detectors. The 1 mm thick aluminum window and 1 mm thick copper window determine the threshold energy for detectors P3 and P4

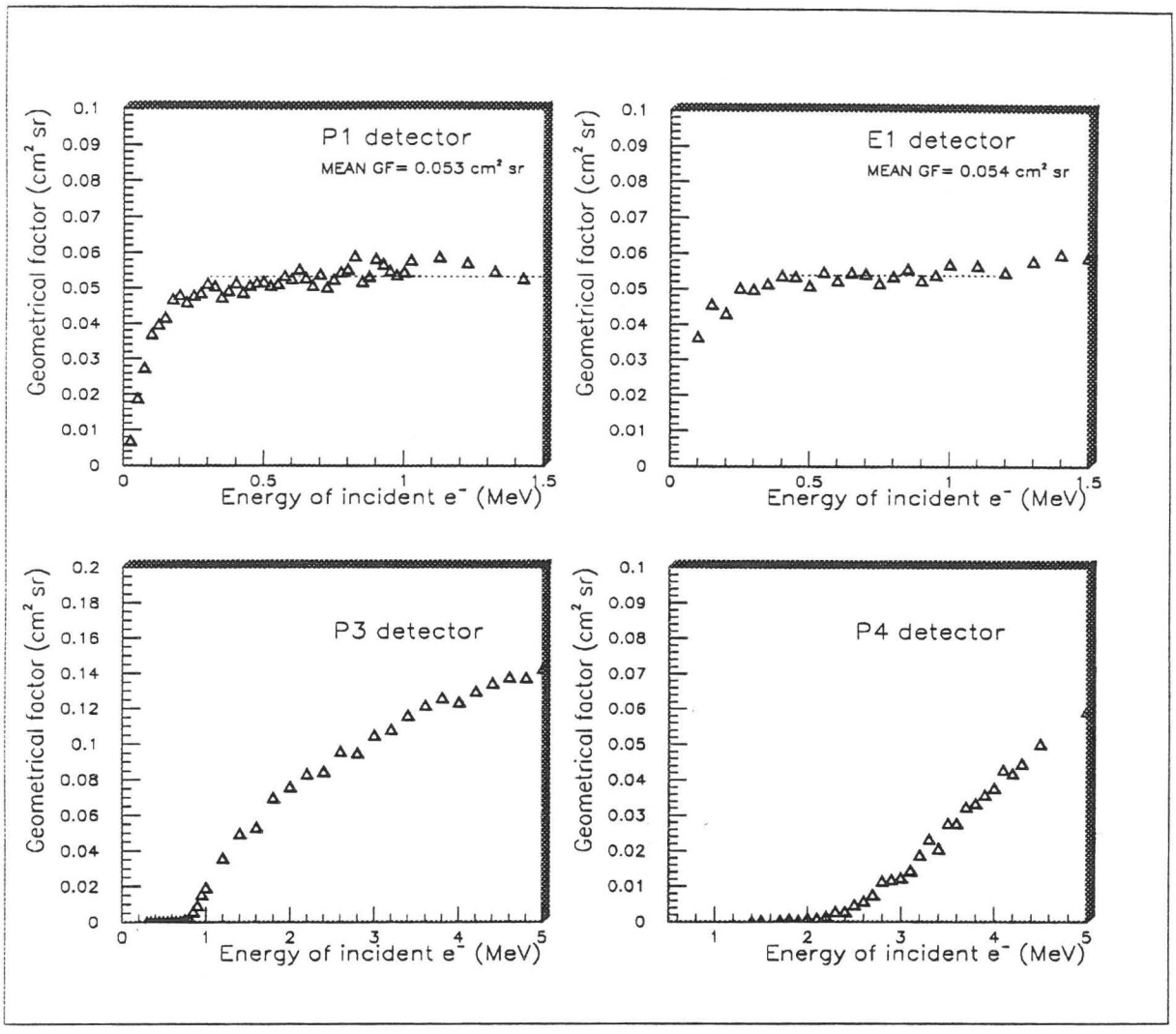

Figure 2.1: Geometrical Factor for electrons as a function of energy. The name of the detector is indicated in the insert, along with the mean value of the GF in the plateau region.

respectively. The three threshold energies given for each particle are to be interpreted as maximum energy values (at the given precision) at which 1/1000, 1/100 and 50/100 of the particles penetrating the detector perpendicularly to the windows planes hit the sensitive element.

2.1.5 The peak (penetration) energy

The peak (penetration) energy is mainly determined by the entrance window and the sensitive element thicknesses. The values given in Table 2.1 are defined as incident energy for which the average energy lost (over 10^5 particles) in the sensitive element is maximum. In this case too the particles are impacting perpendicularly the detector.

Property	DETECTOR			
	P1 and P2	P3	P4	E1 and E2
Sight angle (degree)	90 0	90	90	90 0
F.O.V half angle (degree)	20.5	33.5	33.5	20.5
Aperture (cm^2)	0.20	0.28	0.28	0.20
Geometric factor ($cm^2\ sr$)	0.053	0.25	0.25	0.053
Entrance window ($\mu m/compound$)	0.75/Ni	1000/Al	1000/Cu	0.75/Ni
Detector type	A	A	A	B
THRESHOLD ENERGIES (MeV)				
α:	.243	51.92	89.88	.243
	.243	52.07	90.11	.243
	.291	52.54	90.73	.291
p:	.174	12.89	22.36	.174
	.179	12.96	22.48	.179
	.206	13.19	22.83	.206
e^-:	.018	.682	1.67	.018
	.018	.738	1.97	.018
	.032	1.228	3.71	.032
PEAK (PENETRATION) ENERGY:				
α	24.	59.	95.	48.
p	6.	15.	24.	12.
e^-	.37	1.00	2.10	.88
MEAN ENERGY LOST IN Si at PEAK (PENETRATION) ENERGY:				
α	22.8	22.8	22.8	48.
p	5.6	5.6	5.6	12.
e^-	.3	.3	.3	.8
ENERGY BINS:				
1	[0.00-0.33[	[0.00-0.33[	[0.00-0.33[	[0.00-0.03[
2	[0.33-0.54[	[0.33-1.43[	[0.33-1.43[	[0.03-0.053[
3	[0.54-0.88[	[1.43-6.20[	[1.43-6.20[	[0.053-0.093[
4	[0.88-1.43[	[6.20-23.4[	[6.20-23.4[	[0.093-1.16[
5	[1.43-2.33[			[0.16-0.29[
6	[2.33-3.80[			[0.29-0.51[
7	[3.80-6.20[			[0.51-0.90[
8	[6.20-23.40[			[0.90-23.4[

Table 2.1: Properties of the CPD array. **A - type detector**: TU-011-050-300 (see Appendix A for details). **B - type detector**: TU-016-050-1000

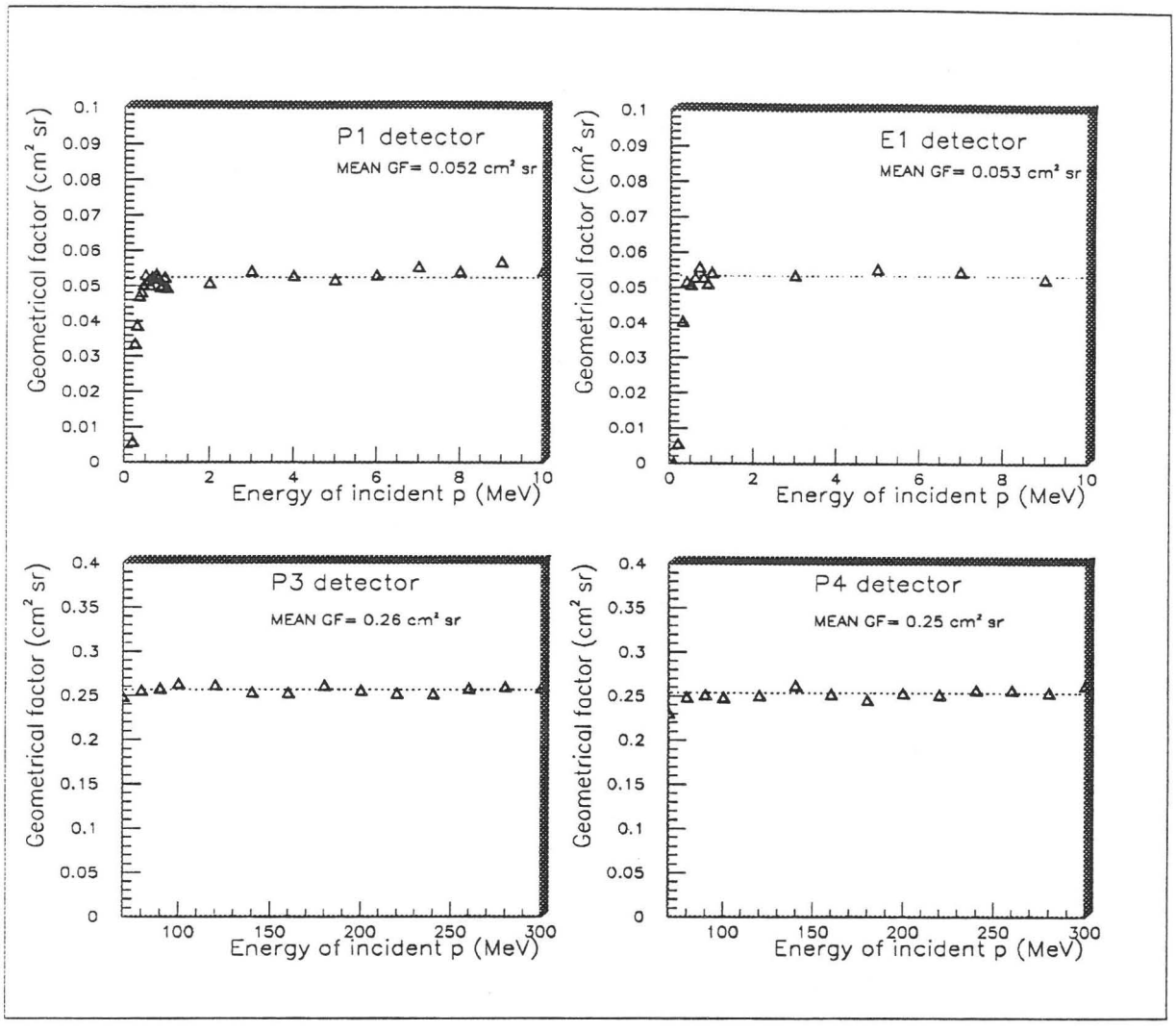

Figure 2.2: Geometrical Factor for protons as a function of energy. The name of the detector is indicated in the insert, along with the mean value of the GF in the plateau region.

2.1.6 The response of the CPD detectors to monoenergetic particles.

The response of detector E1 to an isotropic flux of monoenergetic particles was simulated for a sample of energies: 2 10^5 particles penetrating the detector at uniformly distributed positions within the 0.915 *cm* radius and uniformly distributed in a 2π-solid angle were tracked through the detector. The energy loss in the sensitive element was recorded. The Figures 2.7 to 2.9 show the different spectra for electrons, protons and α, respectively at several energies.

Some general conclusions may be drawn from these output spectra:

- The detected particles may be classified into four categories: (i) those which cross the inner edge (0. to 3 mm thickness) of the last collimator (C3), and lose the remaining energy in the sensor, (ii) those which lose a fraction of their energy in

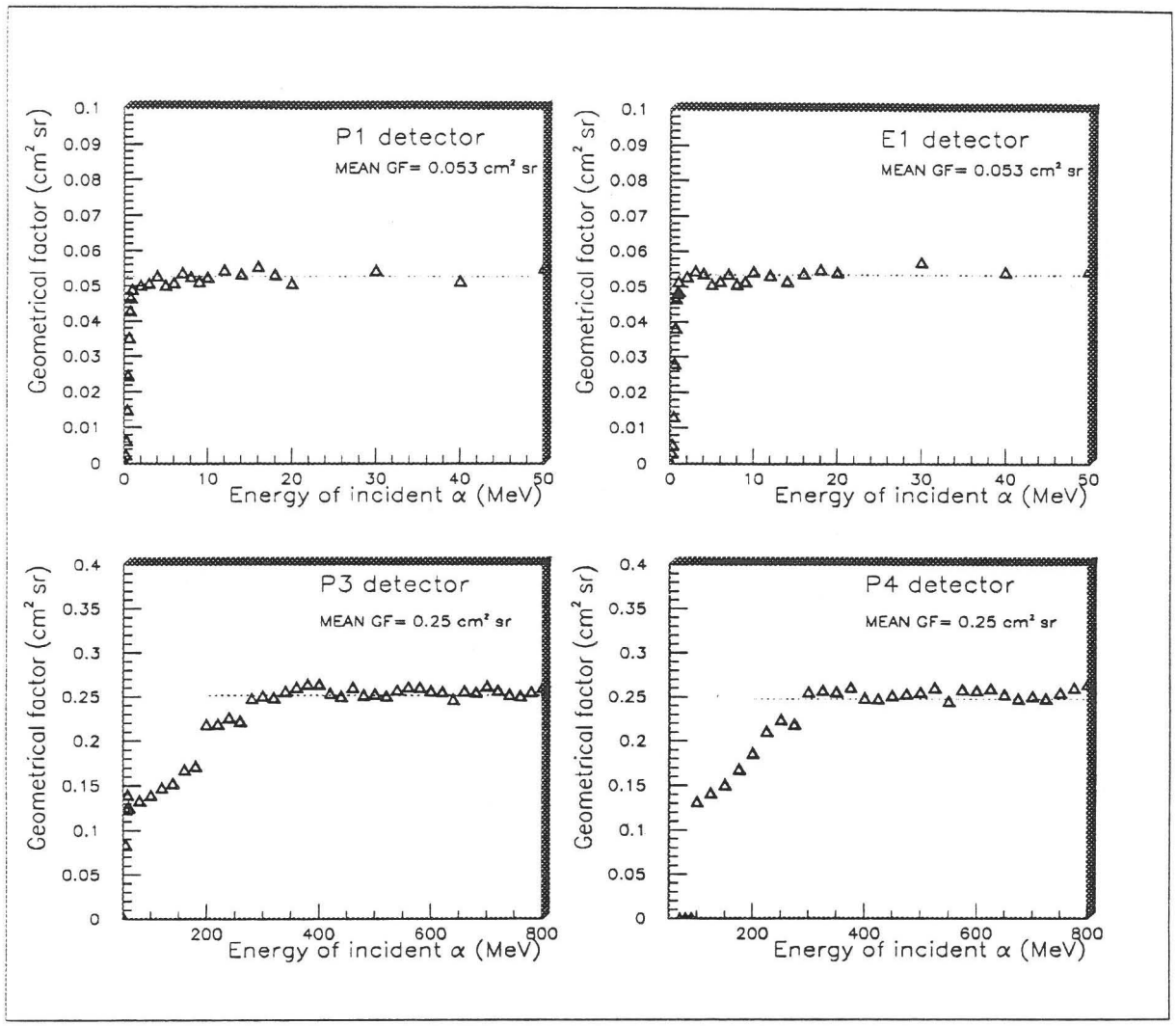

Figure 2.3: Geometrical Factor for *alpha*-particles as a function of energy. The name of the detector is indicated in the insert, along with the mean value of the GF in the plateau region.

the entrance window and cross the sensitive element depositing a fraction of their energy, (iii) particles which lose a fraction of their energy in the collimator and cross the sensitive element depositing a fraction of their energy. (iv) those which lose a fraction of their energy in the entrance window and deposit all the remaining energy in the sensitive element;

- All those particles contribute to differents bins (channels) of the detector, with a possible "peak generation" effect as shown in Figure 2.9: a 200 MeV flux of α-particles produces two main peaks in the detector. This case deserves a careful analysis, since such a behaviour spoils the detector energy resolution.

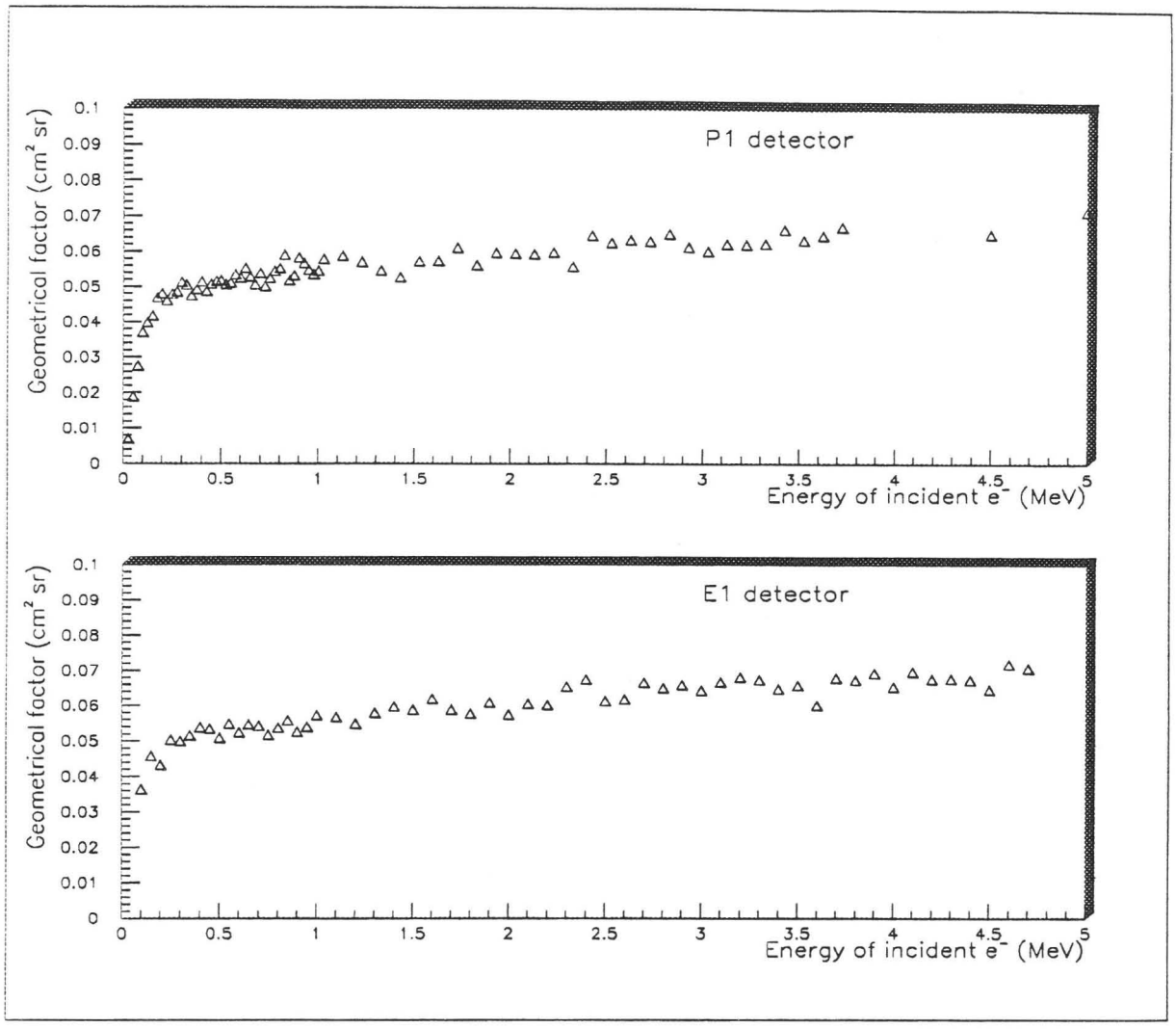

Figure 2.4: Asymptotic variation of the GF of P1 and E1 as a function of electron incident energy.

Figure 2.10 illustrates the results of an analysis of the detector response split into its different contributions: the α-particles which follow the "normal" path deposit 9.5 MeV in the sensitive element. Their spectrum is shown in Figure 2.10 (up - right). This category constitutes more than 50% of all the detected particles. Figure 2.10 (down - left) shows the spectra of the particles which reach the sensitive element after losing less than 100 MeV in the collimator C3. This precisely means that those particles run across less than a 3 mm long path in the brass collimator. The energy deposit ranges from 9.5 to 18 MeV. Much of the contributors to the energy loss spectrum near the 0 MeV limit is due to partial energy loss in the sensor and partial energy loss in the other collimators. In Figure 2.10 (down - right) the spectrum of α-particles which cross the 3 mm thickness of collimator C3 loosing more than 100 MeV is shown. A peak appears at 18 MeV, simulating $\sim$ 18 MeV and $\sim$ 93 MeV α-particles reaching the sensor through the "normal" path.

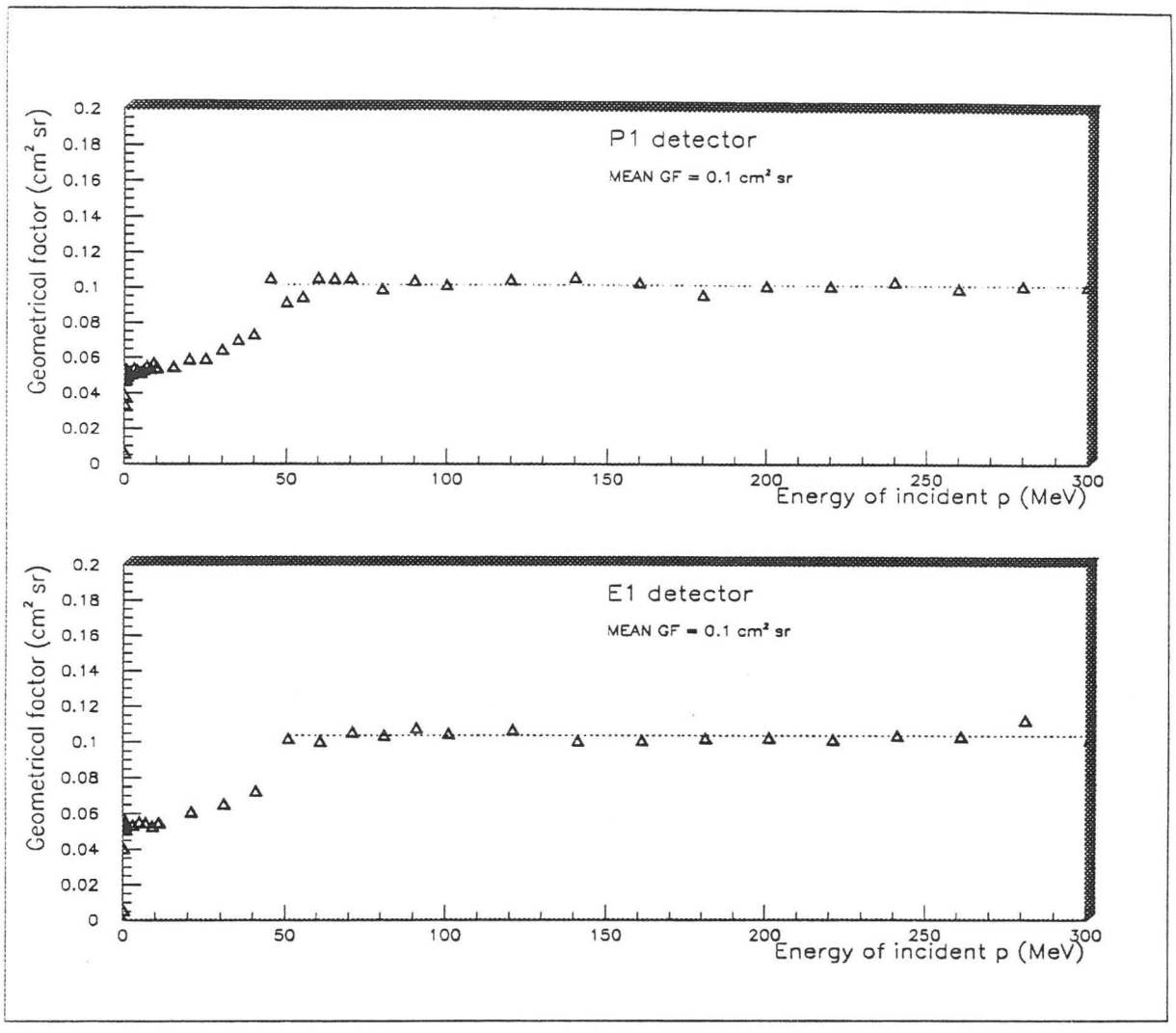

Figure 2.5: Asymptotic variation of the GF of P1 and E1, as a function of proton incident energy.

The kind of analysis described above was also made for 50 MeV protons. The conclusion is that 50 MeV protons going across the "normal" path give a signal of $\sim$ 2.4 MeV, whereas the 50 MeV protons crossing 3 mm through the C3 collimator deposit $\sim$ 4.7 MeV in the sensor, simulating both $\sim$ 4.7 MeV and $\sim$ 23 MeV protons.

2.2 Numerical simulation of a calibration

2.2.1 The CPD channels

The energy lost by particles at peak (penetration) energies depends on the sensor thickness. It has been calculated for all the detectors and the mean values over P1,...P4 and E1, E2 respectively are tabulated. These mean values are used in the design of CPD bins (channels), according to the method described in Appendix A.

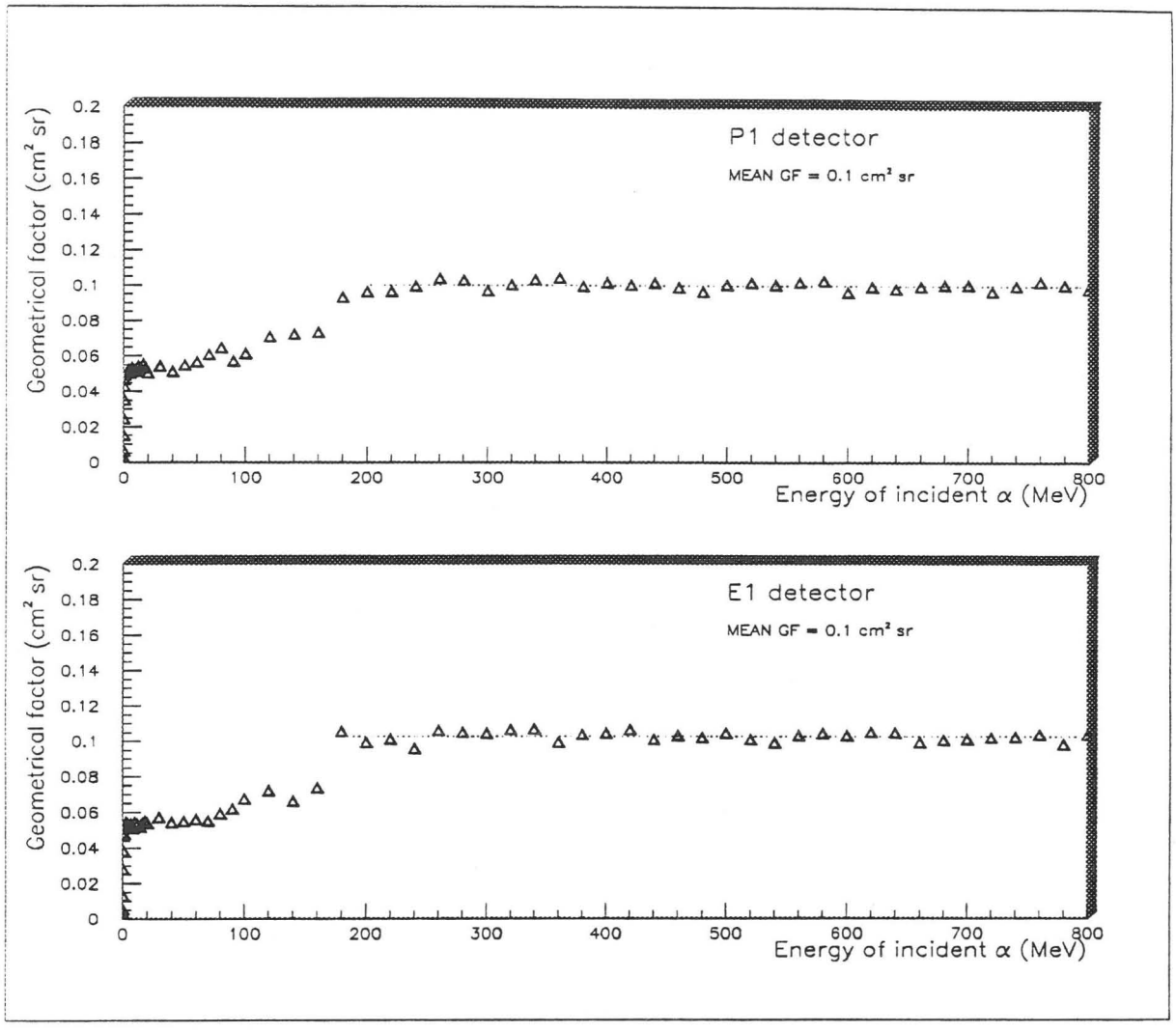

Figure 2.6: Asymptotic variation of the GF of P1 and E1, as a function of α-particles incident energy.

In a first design attempt, the mean energy values were majorated by the calculated uncertainty for protons and α-particles, and by 10% for electrons, in order to avoid the best possible bin crosstalk.
The resulting energy bin limits are shown in Table 2.1 as values of the energy lost in detector sensors.

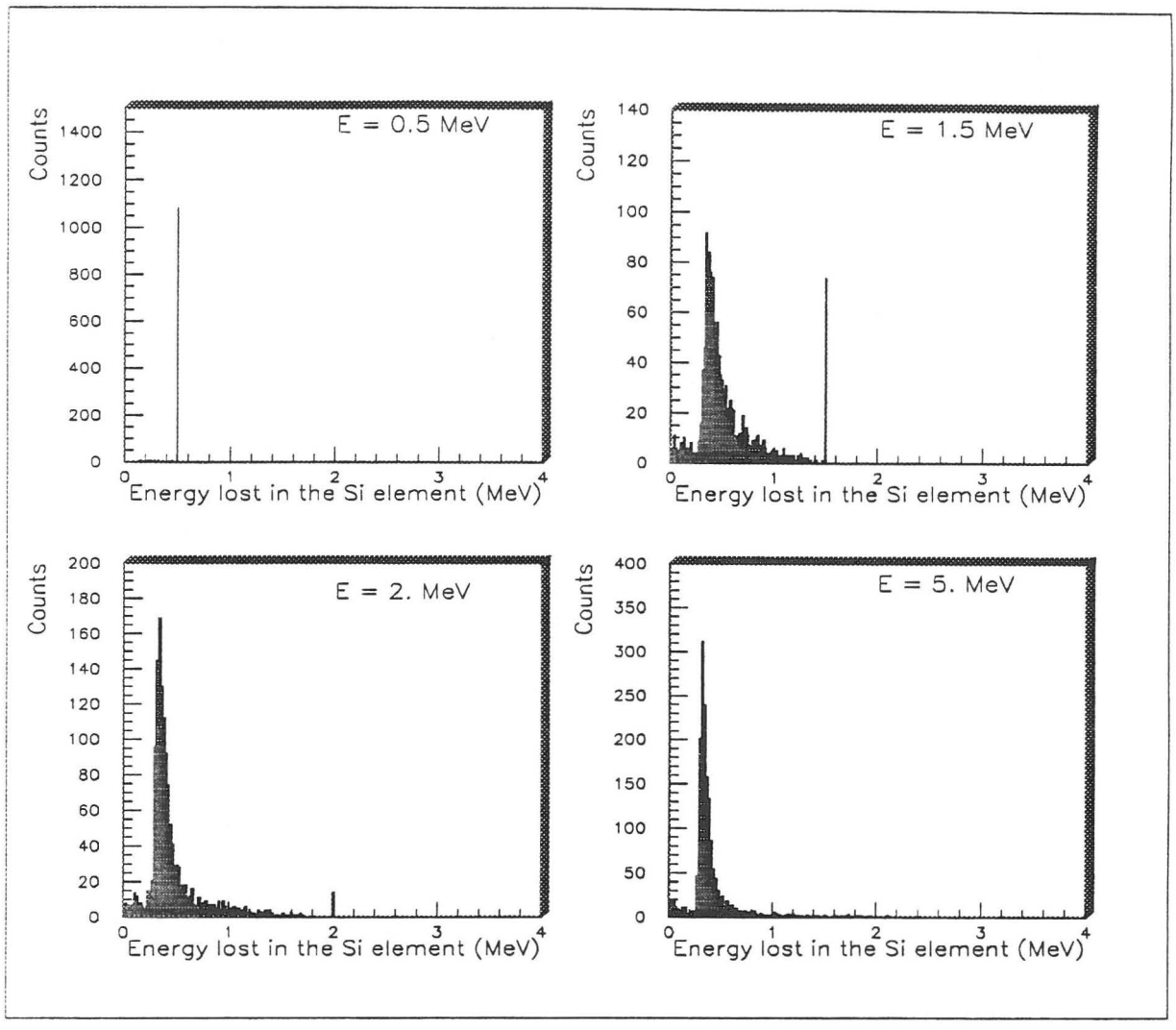

Figure 2.7: Spectrum of the energy lost in the E1 sensor by monoenergetic electrons.

Simulations by GEANT [16] revealed that still many electrons were counted in Bin 2, for P1 detector, due to energy straggling. The energy channels of Table 2.1 were recalculated by use of the maximum energy deposited by $\sim 8\ 10^6$ particles gathered from random positions and directions onto each up-looking detector. This number of particles is expected from a $1s$ counting time in a flux of 10^6 $particles/(s\ cm^2\ sr)$. The energy bins obtained using this method are shown in Table 2.2. They will be used throughout the rest of this document. The main task of the CPD electronic unit is to record any detected particle in one of the 40 incrementable registers. The electronic unit does not perform particle discrimination, neither does it discriminate low energy particles stopped in the sensitive elements from high energy particles depositing the same amount of energy. The way the signal is handled from the sensor to the registers is shown schematically in Figure 4 in Appendix A.

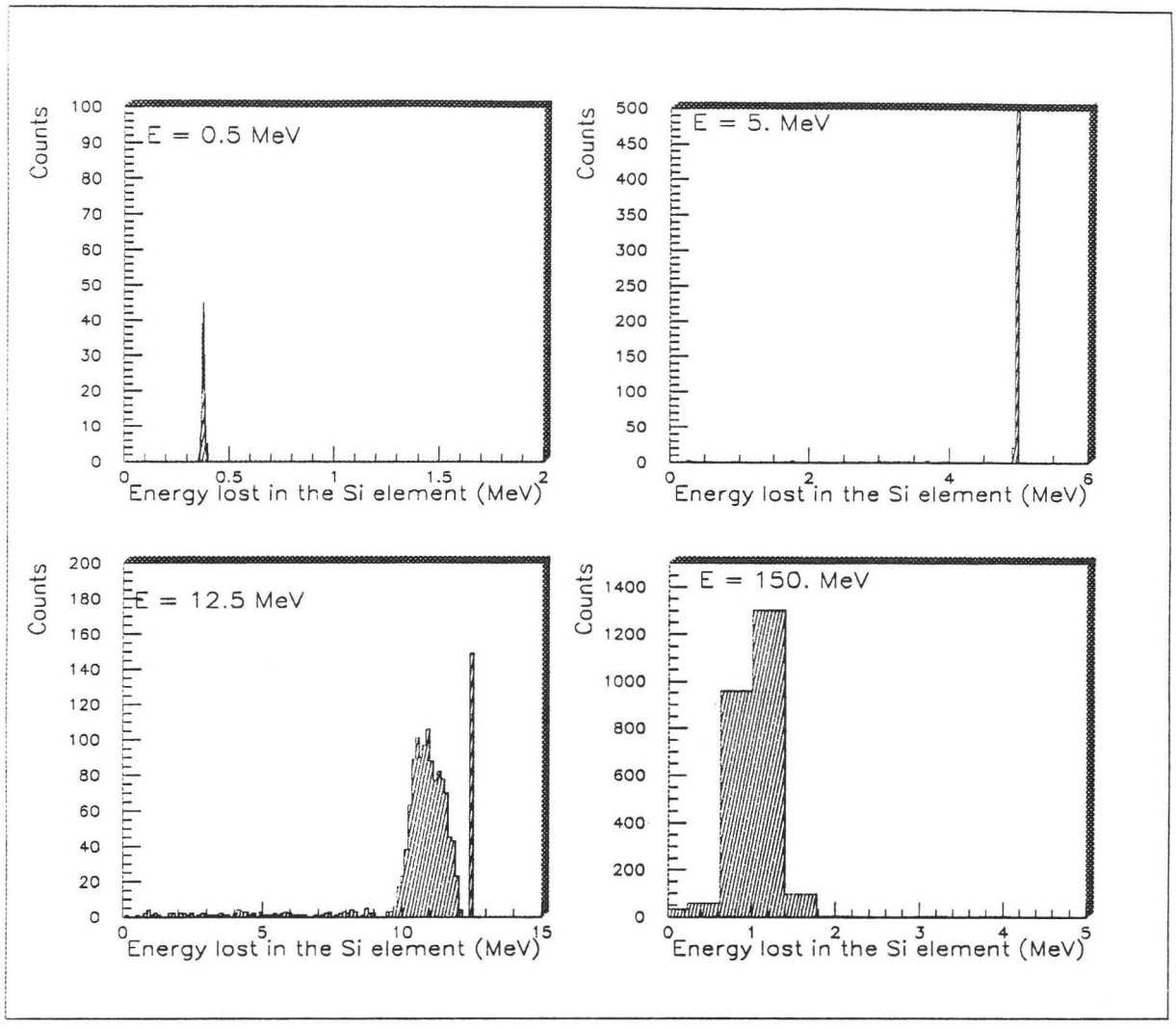

Figure 2.8: Spectrum of the energy lost in the E1 sensor by monoenergetic protons.

2.2.2 The CPD detection efficiency

The probability for a particle of kind k having an energy E_k, to be counted in bin i when it reaches a given detector is a fundamental characteristic of the CPD. These (energy dependent) intrinsic detection efficiencies, $p_i^k(E_k)$ were calculated using GEANT, for electrons, protons and α-particles of energies ranging from 10 keV to 5 MeV, 100 keV to 300 MeV and 100 keV to 500 MeV, respectively. Figure 2.11 to 2.16 show the intrinsic efficiencies for all the three kinds of particles (*solid line*: electron; *dashed line*: protons; *dotted line*: α-particles) as a function of energy. To calculate these functions, 10^6 particles having reached one randomly selected upward-looking detector, were tracked in the detector. The impact point in the 0.915 *cm* radius detector aperture and the momentum direction (angle of incidence) were randomly set and uniformly distributed within their respective domains. The number of hits on anyone among the CPD sensitive elements was recorded and divided by 10^6. The hits on E2 and P2 detectors were recorded too, their number gives an idea of the crosstalk between upward-looking detectors and horizontally looking ones.

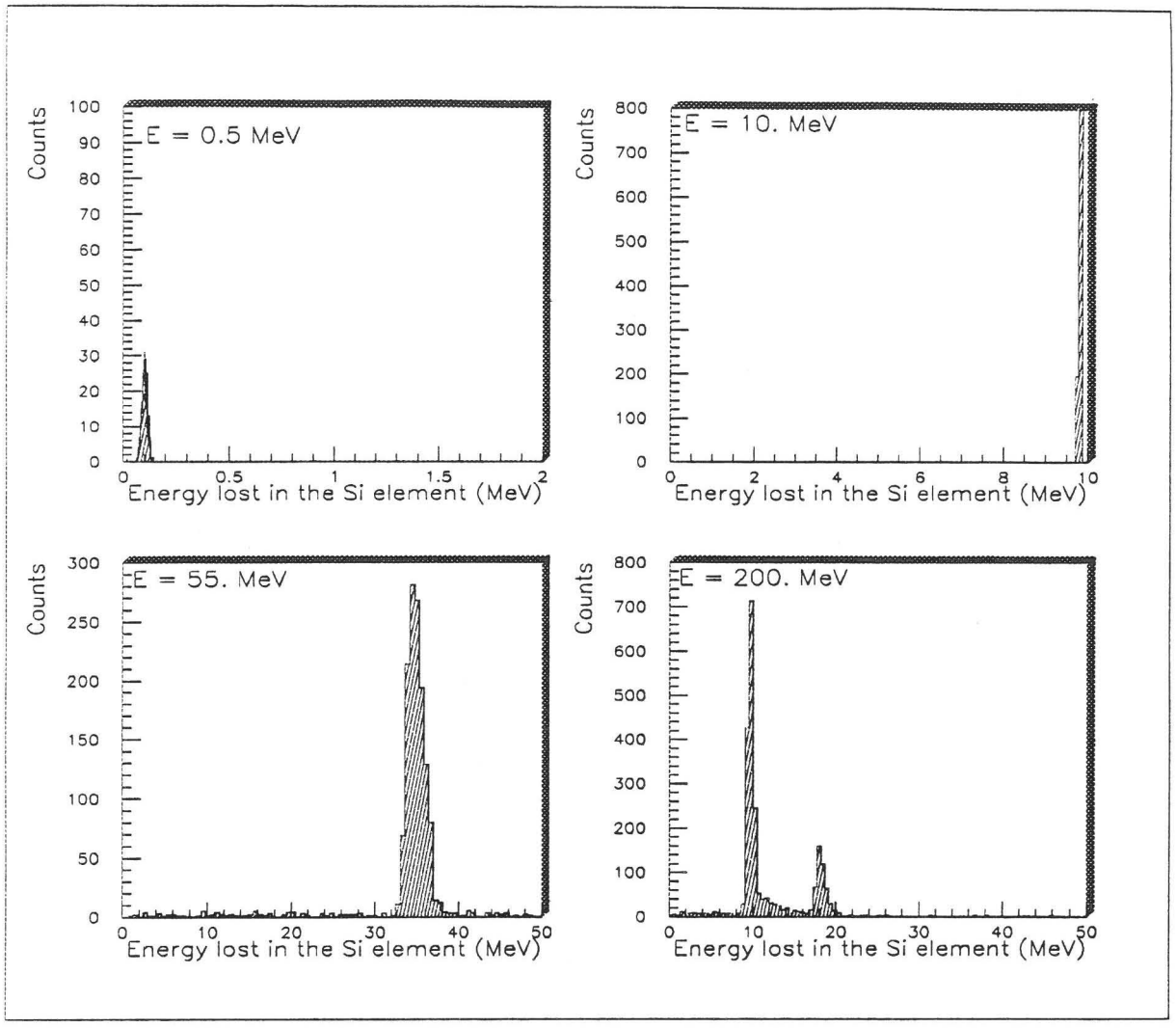

Figure 2.9: Spectrum of the energy lost in the E1 sensor by monoenergetic α-particles.

An attempt was made to improve the energy resolution of the CPD. Our aim was to reduce the spread of counts into many bins for particles of equal energies which penetrate into the CPD. Such a behaviour might complicate both the particle discrimination and energy spectrum determinations. The tentative modification was to replace the "sliced collimator" by a massive conical collimator along the whole particle path. By this change all the "false" peaks were eliminated. A detailed presentation of this study can be found in Appendix D.

2.3 Comparison of the simulation with the actual calibration

Actually, only the detector *line shape* function (linked to the fluctuation of charge carrier production in the solid state sensor for a fixed energy deposit) is not included in our calculations. This function should normally be used to transform the spectra of energies lost in the sensors into spectra of pulse height. As a consequence, the steps in the efficiency functions might be less sharp, but the results obtained here remain good approximations to be used in spectrum deconvolutions.

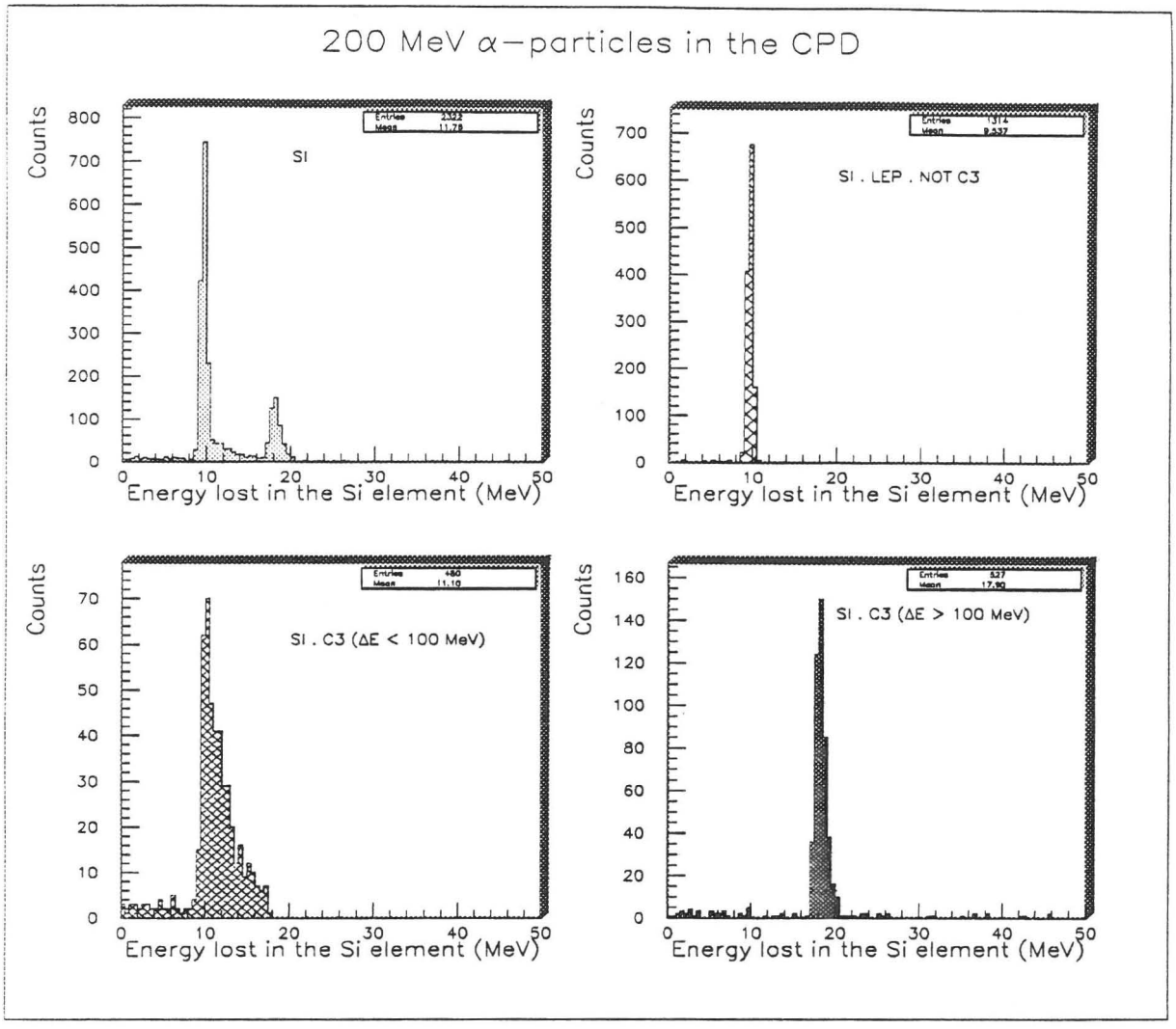

Figure 2.10: Spectrum of the energy lost in the E1 sensor by 200 MeV α-particles.

On comparing the simulation results shown in Table 2.1 and the calibration results in Appendix A, one can conclude to the reliability of the CPD simulation model. The cases for which a bit of disagreement is found are underlined. They always concern detection characteristics of α-particles. Since the results of Table 2.1 have been checked using GEANT, VRANGE [15] and TRIM [14], we will use these values for all the forthcoming calculations.

Bin number	DETECTOR		
	P1 and P2	P3 and P4	E1 and E2
1	[0.00-2.50[	[0.00-2.50[	[0.00-0.03[
2	[2.50-3.15[	[2.50-5.00[	[0.03-0.06[
3	[3.15-3.97[	[5.00-10.0[	[0.06-0.13[
4	[3.97-5.00[	[10.0-26.0[	[0.13-0.27[
5	[5.00-6.30[		[0.27-0.57[
6	[6.30-7.94[		[0.57-1.20[
7	[7.94-10.0[		[1.20-2.50[
8	[10.0-26.0[		[2.50-50.0[

Table 2.2: Energy bin limits taking into account the uncertainty on the energy deposit in the sensors.

2.4 The expected response of the CPD to a typical space radiation environment

2.4.1 Theoretical estimates

The expected number of particles recorded in CPD bin i per unit time is

$$N_i^{th} = N_i^{e^-} + N_i^p + N_i^\alpha \tag{2.1}$$

where $N_i^{e^-}, N_i^p$ and N_i^α are the count rate induced by electrons, protons and α-particles respectively. These count rates may be expressed as

$$N_i^k = \int_{E_{min}^k}^{E_{max}^k} p_i^k(E_k) J_d^k(E_k) \Gamma_k(E_k) dE_k \tag{2.2}$$

where

$p_i^k(E_k)$: the intrinsic detection efficiency,

$\Gamma_k(E_k)$: the probability for particle of type k having energy E_k, to reach one of the upward-looking detectors aperture. In an isotropic particle flux, this quantity is simply equal to πA, (A beeing the total detector surface facing the space environment: $A = 4\ \pi\ 0.915^2 cm^2$).

$J_d^k(E_k)$: the differential flux for particles of type k at energy E_k (expressed in $1/(s\ cm^2\ sr\ MeV)$). These functions are often parametrized as

$$J_d^k(E_k) = C_k E_k^{-\gamma_k} \tag{2.3}$$

but the values used here for count rates estimates were supplied as tables by SPENVIS [6] (see Figure 2.17 and 2.18).

E_{min}^k is the threshold energy of particles of type k. These energy have been given values: 0.010 MeV for electrons and 0.1 MeV for protons and α-particles.

E_{max}^k is the maximum energy for which the flux of particles of type k is not negligible for the CPD experiment. These energy values are set to 5 MeV, 300 MeV and 500 MeV, for electrons, protons and α-particles, respectively.

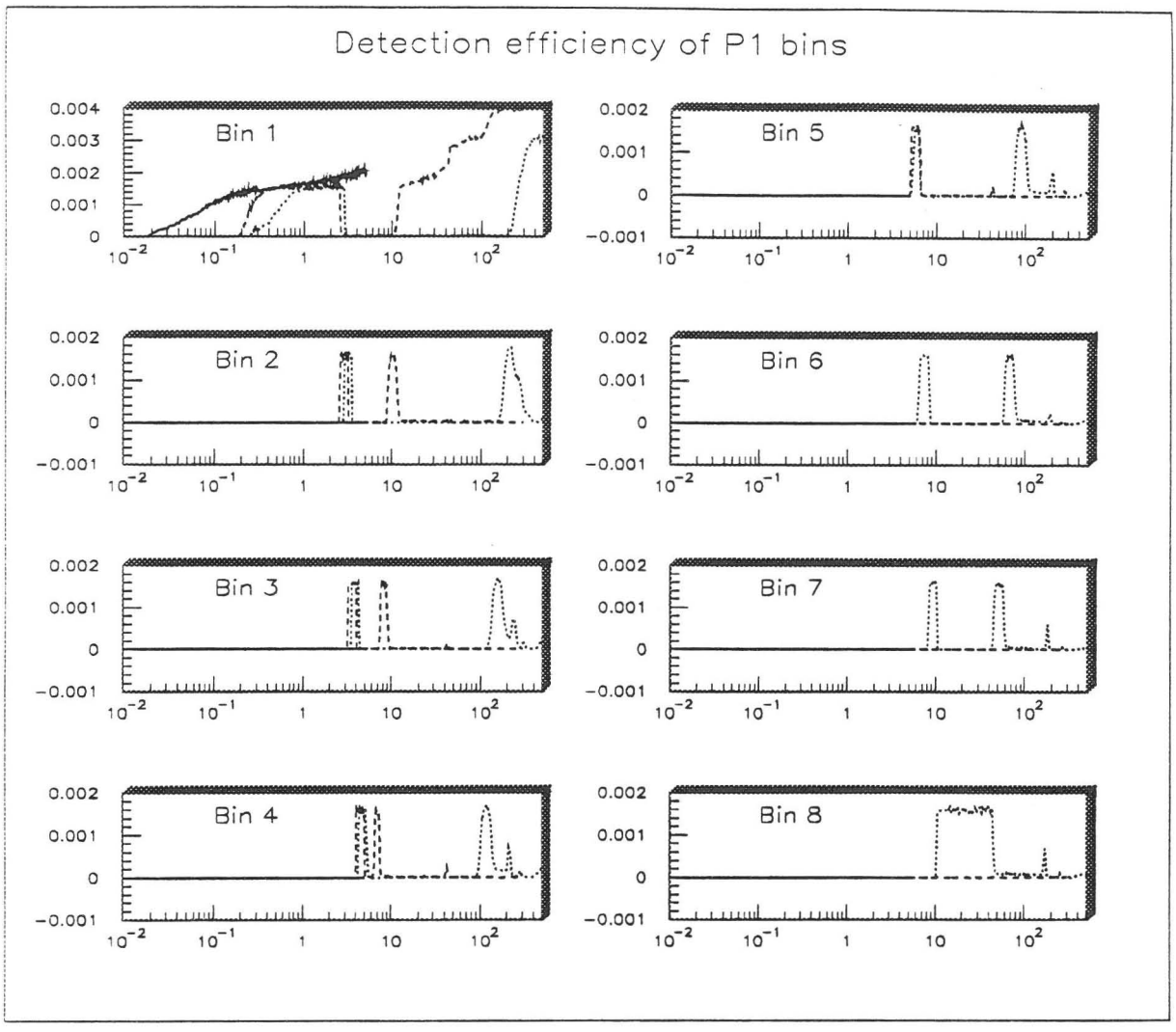

Figure 2.11: Detection efficiency of P1 detector subunit, as a function of incident particle energy. Solid, dashed and dotted lines are for electrons, protons and α-particles, respectively.

Provided that all the functions in expression 2.2 are mathematicaly defined, one can predict the count rate to be observed in each bin using Equation 2.1.

The actual integral fluxes for electrons ($2\ 10^6\ e^-/(s\ cm^2)$) and protons ($2\ 10^4\ p/(s\ cm^2)$) at the 60th minute - orbital time, (see Figure 2.19 and 2.19) were used. For α-particles, the proton spectrum was used though its maximum energy is set to 300 MeV; the integral flux was set to $2\ 10^3\ \alpha - particles/(s\ cm^2)$. The characteristics of the spectra are summarized in Table 2.3.

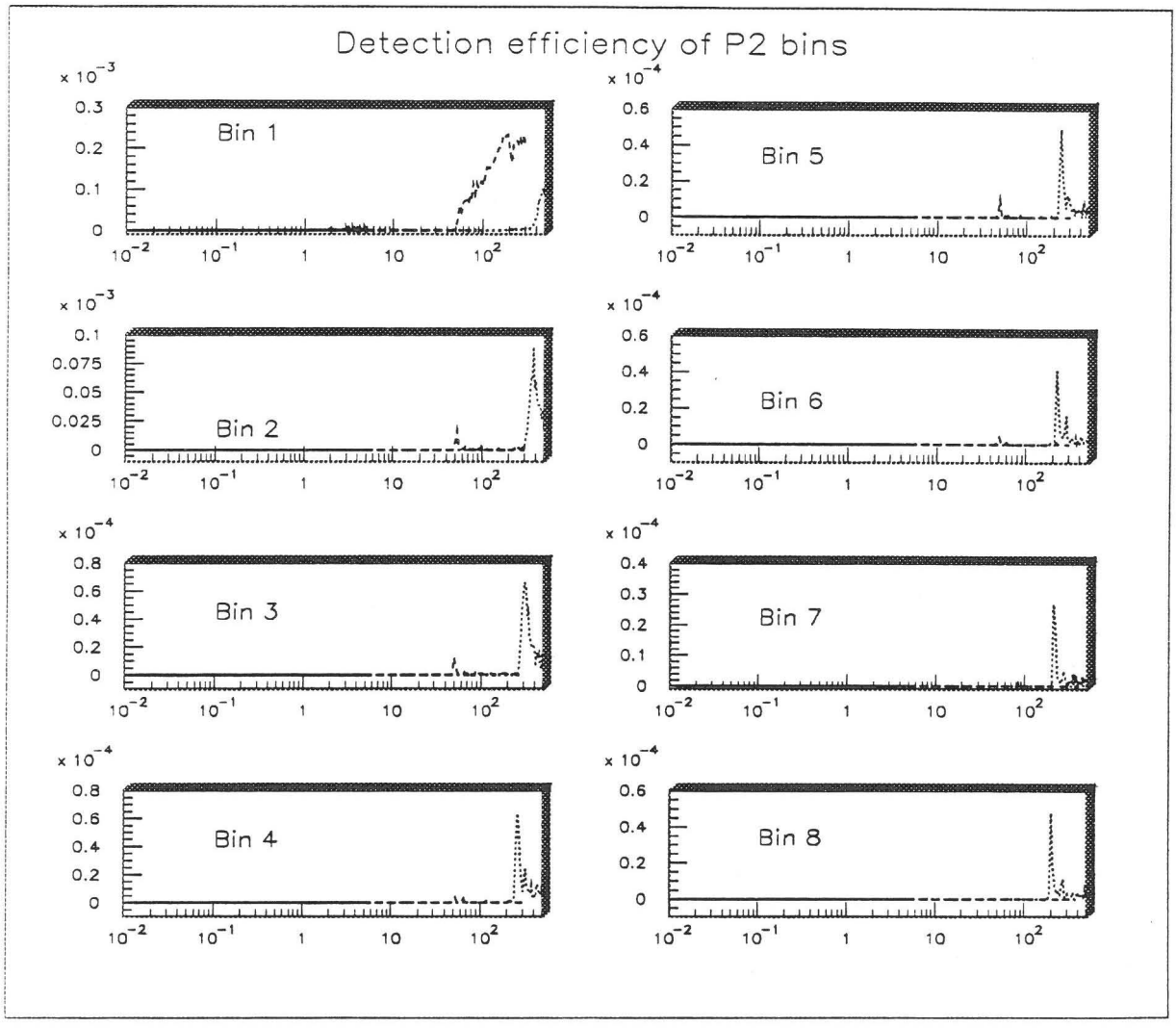

Figure 2.12: Detection efficiency of P2 detector subunit, as a function of incident particle energy. All the particles reach the CPD through the upward-looking detectors. Solid, dashed and dotted lines are for electrons, protons and α-particles, respectively.

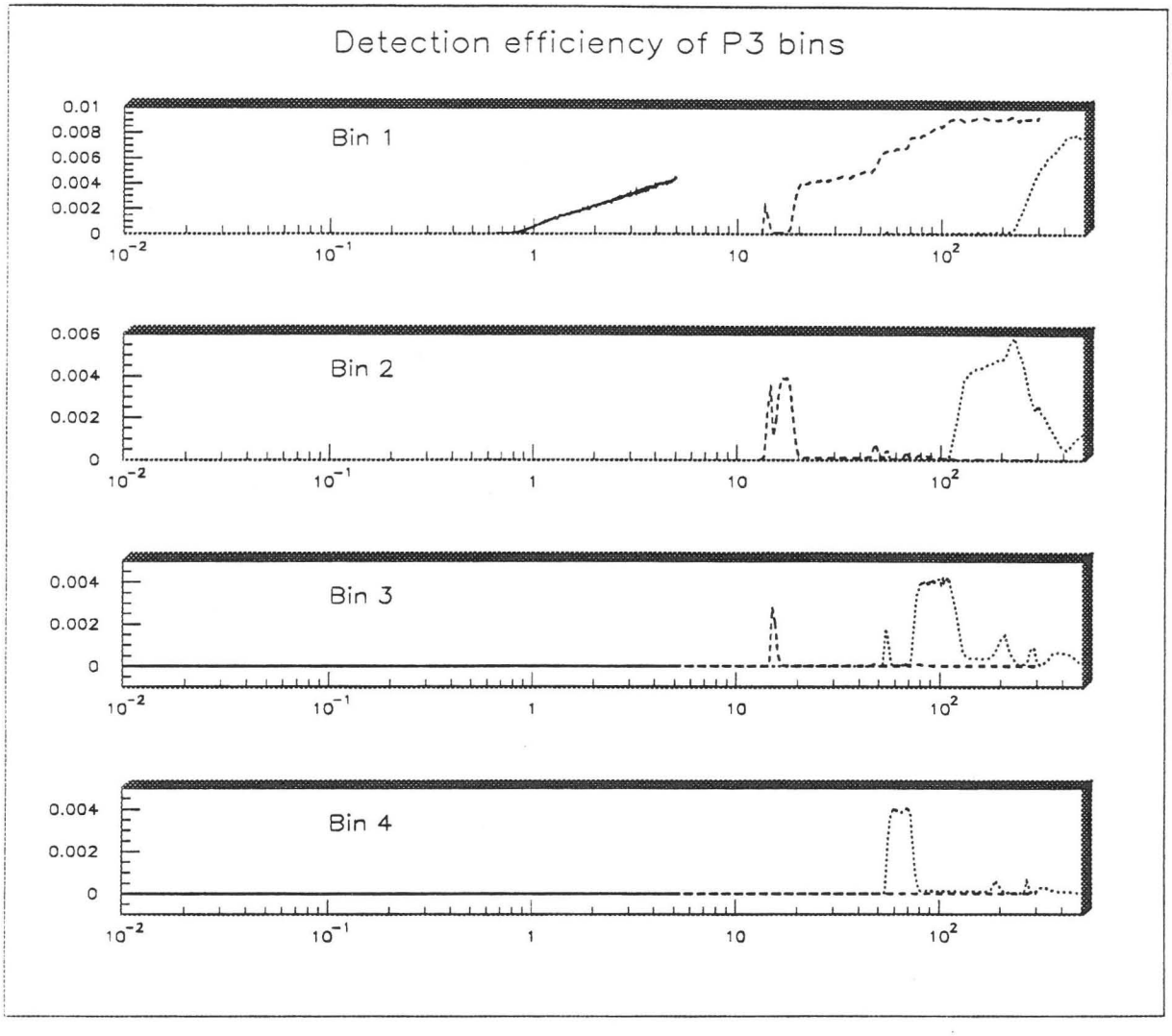

Figure 2.13: Detection efficiency of P3 detector subunit, as a function of incident particle energy. Solid, dashed and dotted lines are for electrons, protons and α-particles, respectively.

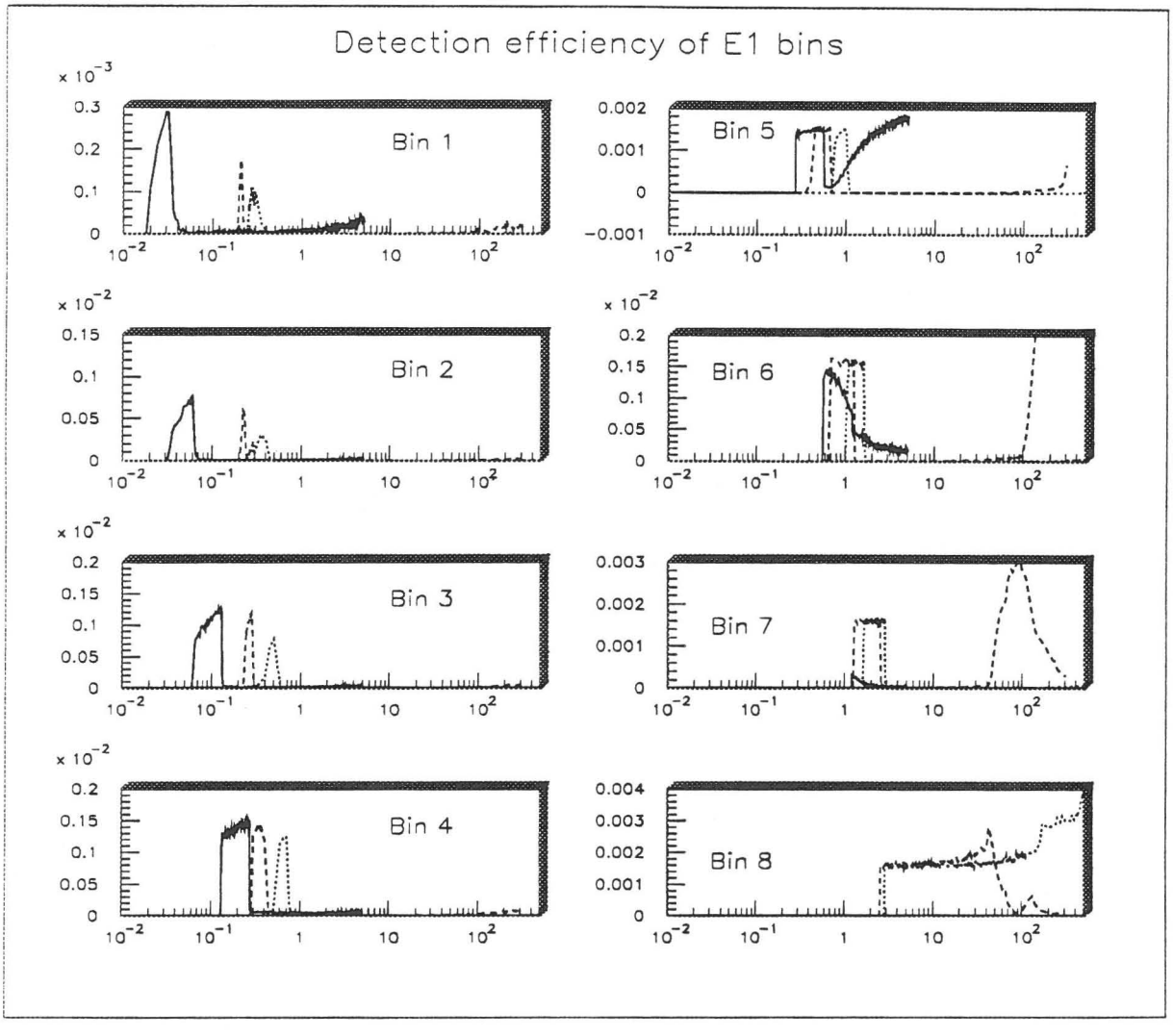

Figure 2.15: Detection efficiency of E1 detector subunit, as a function of incident particle energy. Solid, dashed and dotted lines are for electrons, protons and α-particles, respectively.

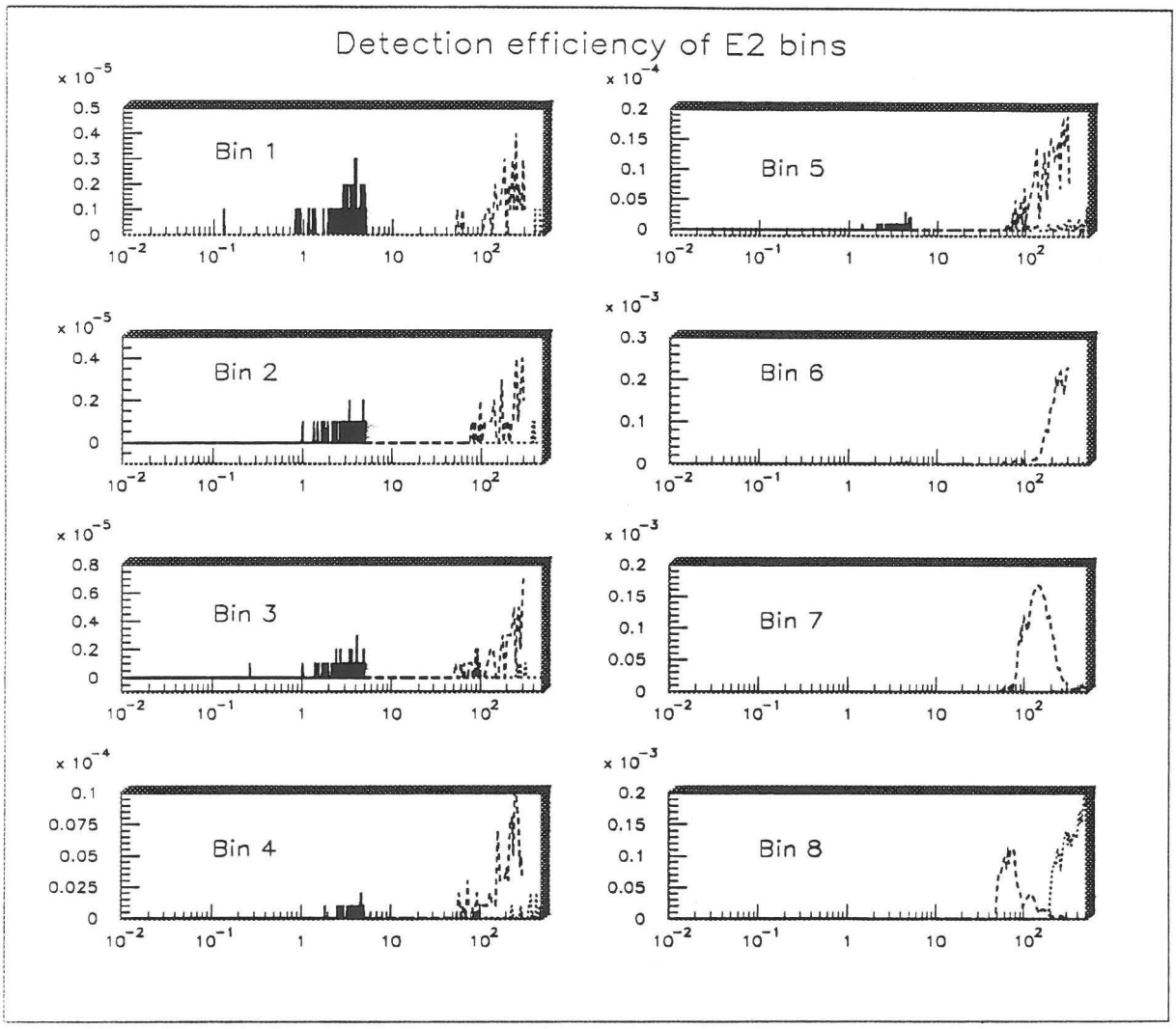

Figure 2.16: Detection efficiency of E2 detector subunit, as a function of incident particle energy. All the particles reach the CPD through the upward-looking detectors. Solid, dashed and dotted lines are for electrons, protons and α-particles, respectively.

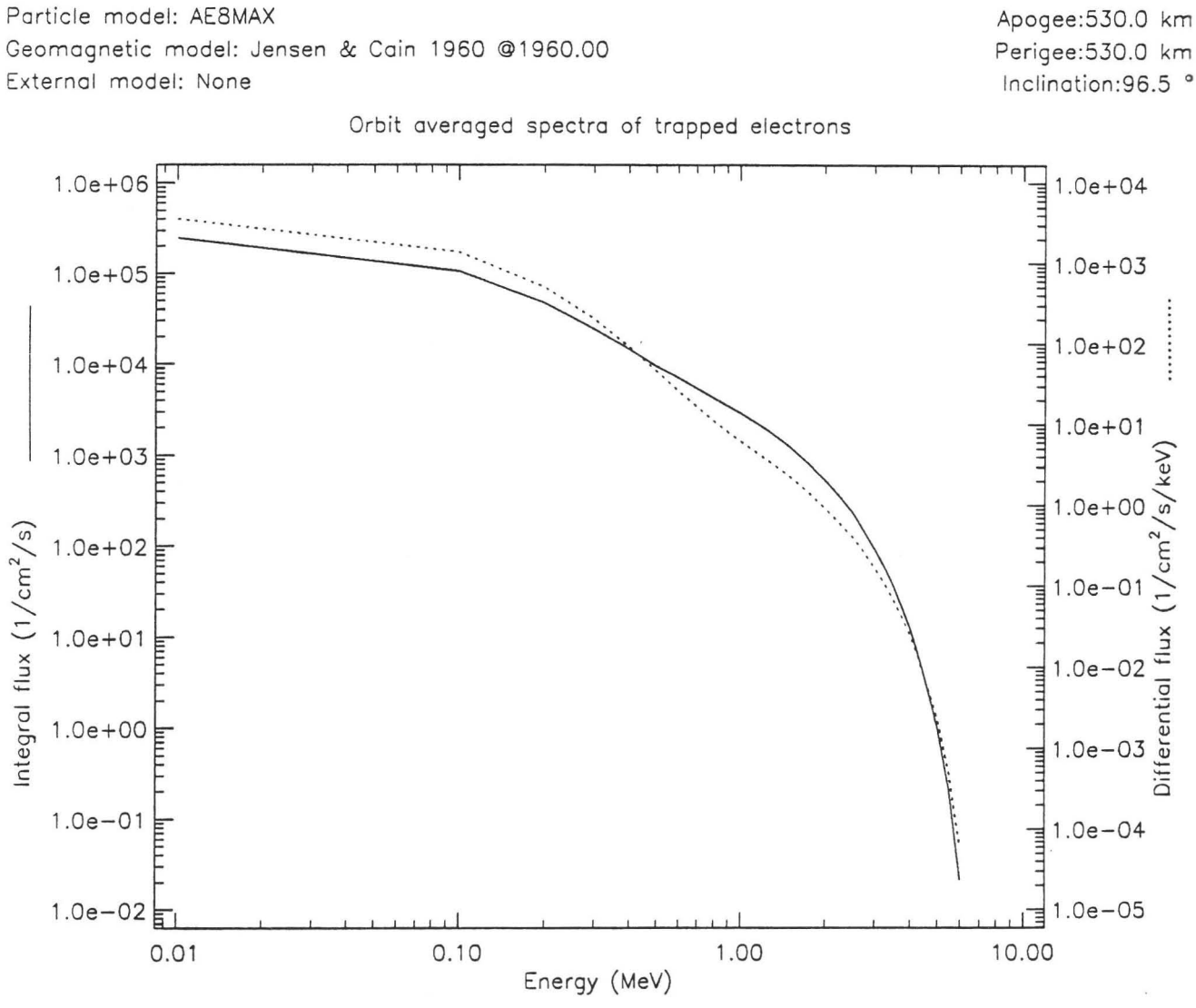

Figure 2.17: Integral and differential trapped electron spectrum average over 16 ØRSTED orbital periods.

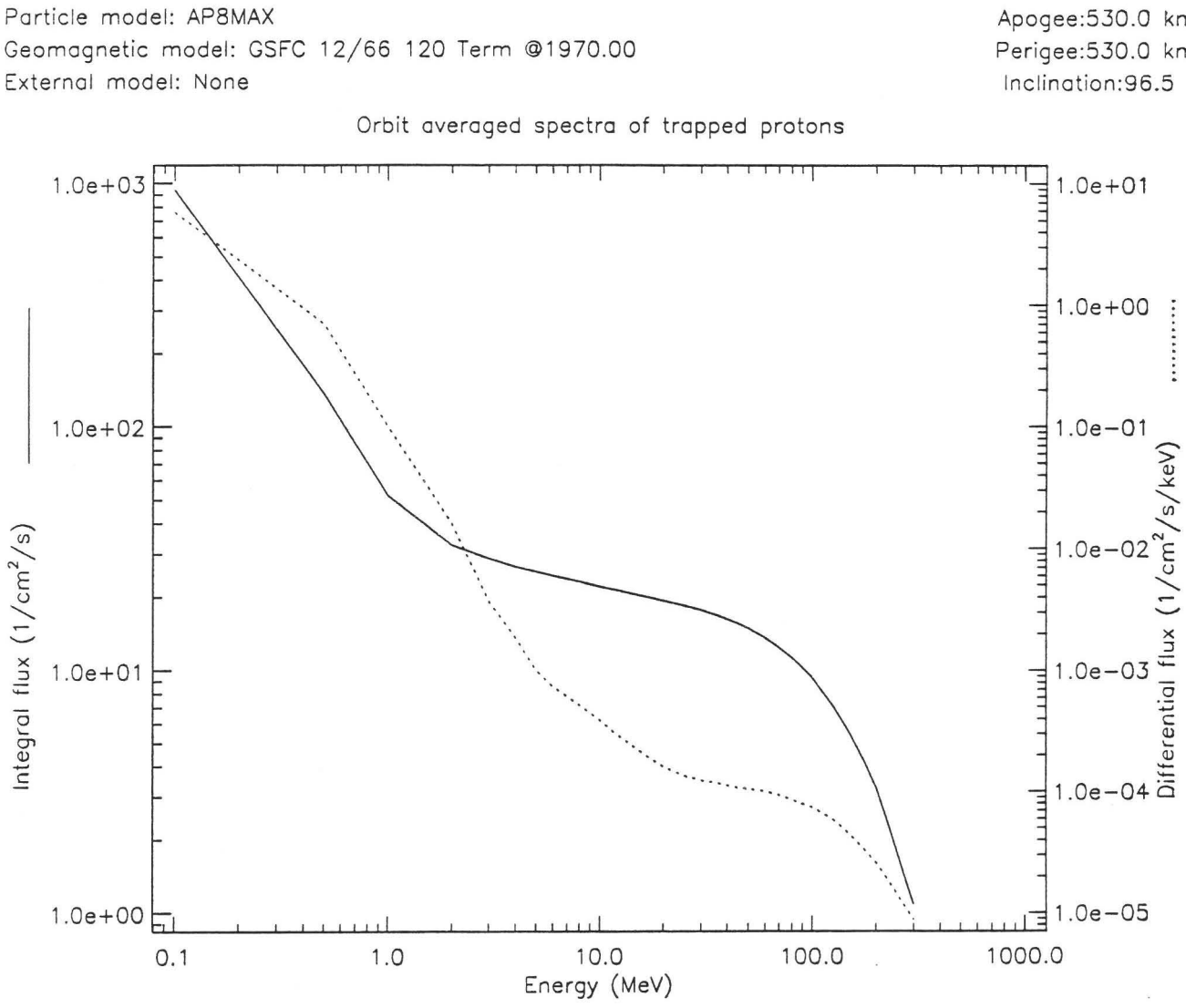

Figure 2.18: Integral and differential trapped proton spectrum average over 16 ØRSTED orbital periods.

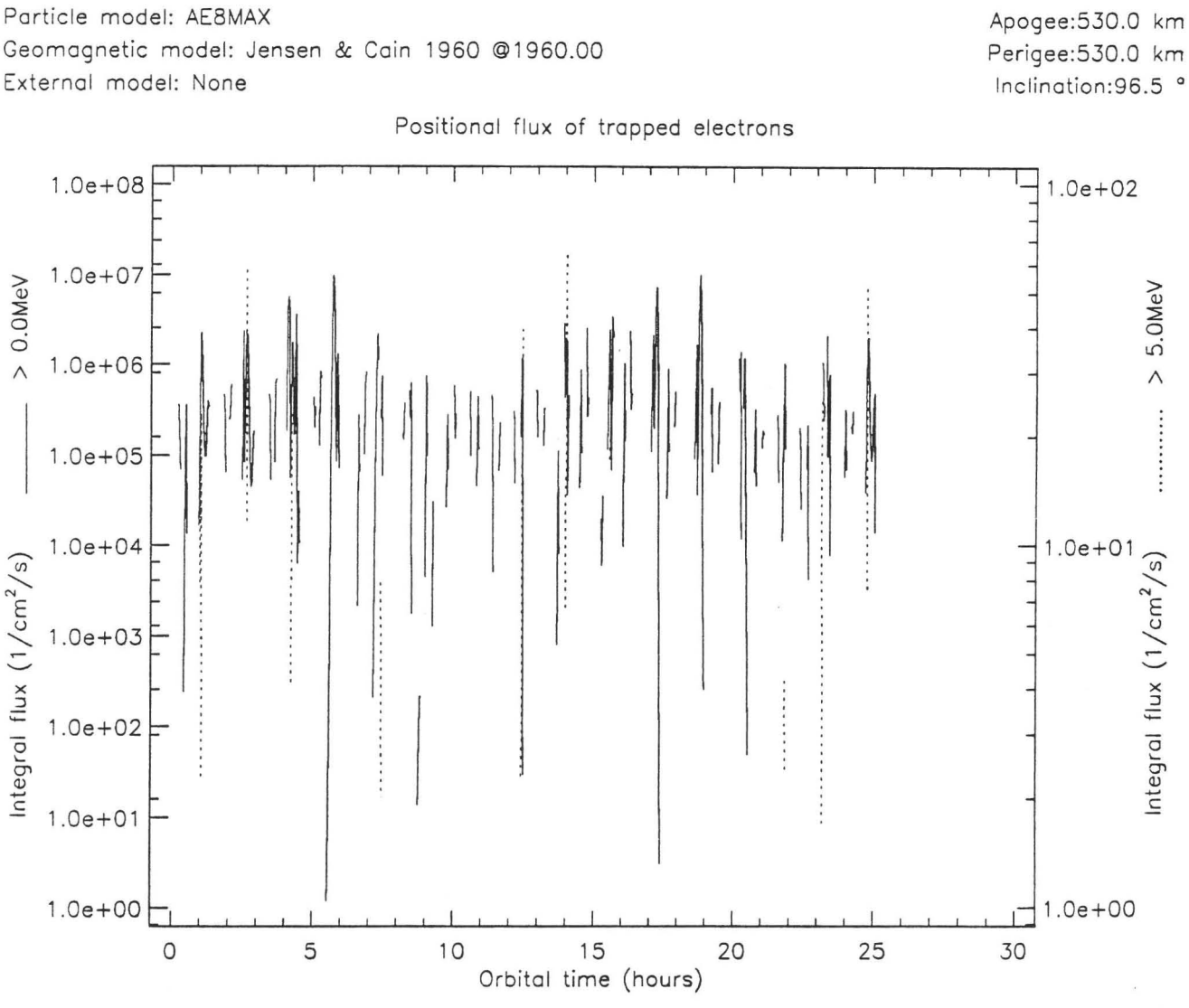

Figure 2.19: Integral trapped electron fluxes on ØRSTED orbit as a function of orbital time.

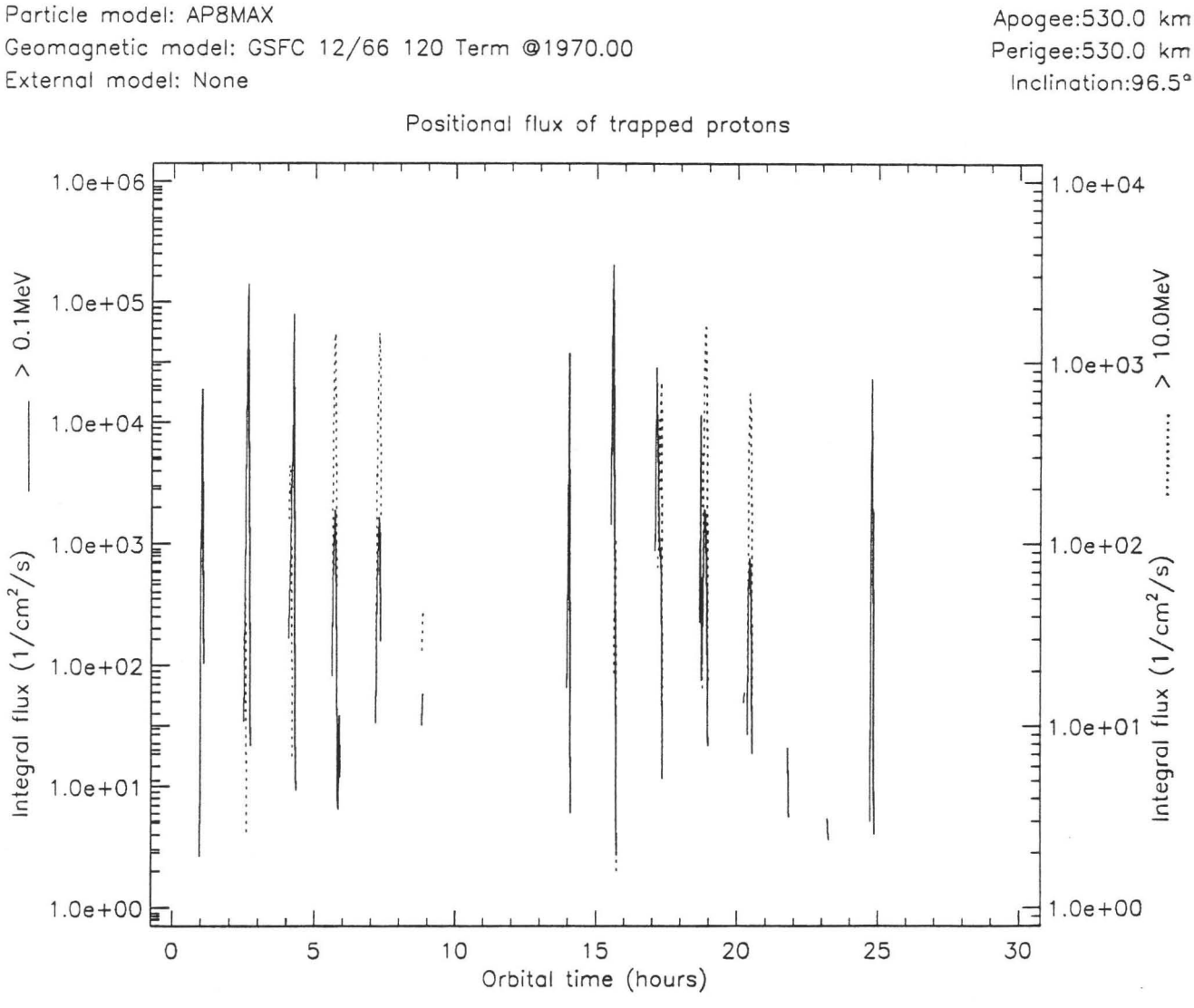

Figure 2.20: Integral trapped proton fluxes on ØRSTED orbit as a function of orbital time.

Particle	E_{min} (MeV)	E_{max} (MeV)	$J(E > E_{min})$ $(1/(s\ cm^2)$	Impact rate on the four detectors (1/s)
Electron	0.010	5.0	$2\ 10^6$	5260440
Proton	0.100	300.0	$2\ 10^4$	52604
α	0.100	300.0	$2\ 10^3$	5260

Table 2.3: Parameters of the particle spectra on ØRSTED orbit, at minute 60.

The calculated bin counts are shown in Table 2.4 as well as the count rates obtained by GEANT simulation. This clearly shows that once the detection efficiency is reliably estimated, it can be used to estimate count rates in order to avoid very time consuming simulations.

2.4.2 The expected CPD response to auroral electrons

The typical auroral electron spectrum shown in Figure 2.21 was used to estimate the CPD count rates at auroral latitudes. One of the energy spectra supplied by D.S. Evans [9] has been extrapolated from $\sim$ 30 keV (maximum experimental energy) to $\sim$ 600 keV. The auroral electron integral fluxes are about $10^8\ e^-/(s\ cm^2\ sr)$ for electrons with energy greater than 14 keV at 138 km, 201 km and 840 km altitudes (see [9, 10, 8]). This value of the integral flux was adopted for the 530 km altitude of ØRSTED orbit. The angular distribution of the auroral electrons was assumed to be isotropic at the ØRSTED orbit [11]. The CPD counts during a 1 ms time interval are shown in Table 2.5. The proton contribution was not included.

2.4.3 Pulse pile-up effects in the CPD

The electronics can easily handle count rates up to $5\ 10^4$ particles/second [5] and the particle fluxes like those encountered in the South Atlantic Anomaly on ØRSTED orbit should be processed without special care. The detector dead-time which will be measured in flight will be used to transform the apparent count rates into actual rates of impact on the detector sensors.

The particle fluxes encountered in the auroral region are likely to cause one or both of the following problems:

- The pulse pile-up effects which results in an overestimate of the low energy part of any particle spectrum.
- The almost continuous hits ($\approx 2\ 10^6$ hits/second on P1) on the sensor may paralyse the detector.

Though the detectors P3 and P4 may handle the auroral electron flux, due to their higher energy threshold for electrons, the four other detectors will trigger the electronic system so often that even tasks related to P3 and P4 will be hampered.

Equation 2.2			Simulated		
Detector	Bin	Counts	Detector	Bin	Counts
P1	1	4666	P1	1	4834
	2	0		2	0
	3	0		3	0
	4	0		4	0
	5	0		5	1
	6	0		6	0
	7	0		7	0
	8	0		8	0
P2	1	0	P2	1	0
	2	0		2	0
	3	0		3	0
	4	0		4	0
	5	0		5	0
	6	0		6	0
	7	0		7	0
	8	0		8	0
P3	1	112	P3	1	141
	2	0		2	0
	3	0		3	0
	4	0		4	0
P4	1	8	P4	1	14
	2	0		2	0
	3	0		3	0
	4	0		4	0
E1	1	167	E1	1	168
	2	584		2	610
	3	1506		3	1567
	4	1622		4	1668
	5	781		5	762
	6	173		6	151
	7	9		7	9
	8	1		8	2
E2	1	0	E2	1	0
	2	0		2	0
	3	0		3	0
	4	0		4	0
	5	0		5	0
	6	0		6	0
	7	0		7	0
	8	0		8	0

Table 2.4: Calculated and simulated CPD count rate on ØRSTED orbit for spectra decribed in Figure 2.17 through 2.18.

Simulated		
Detector	Bin	Counts
P1	1	2217
	2	0
	3	0
	4	0
	5	0
	6	0
	7	0
	8	0
P2	1	0
	2	0
	3	0
	4	0
	5	0
	6	0
	7	0
	8	0
P3	1	2
	2	0
	3	0
	4	0
P4	1	4
	2	0
	3	0
	4	0
E1	1	43
	2	80
	3	408
	4	841
	5	976
	6	24
	7	0
	8	0
E2	1	0
	2	0
	3	0
	4	0
	5	0
	6	0
	7	0
	8	0

Table 2.5: Simulated CPD counts after a 1 ms time interval at auroral latitude of ØRSTED orbit. Only electrons events are initiated (at the up-looking detector entries) and counted. The incident flux of electrons is isotropic and equal to 10^8 $particles/(s\ cm^2\ sr)$.

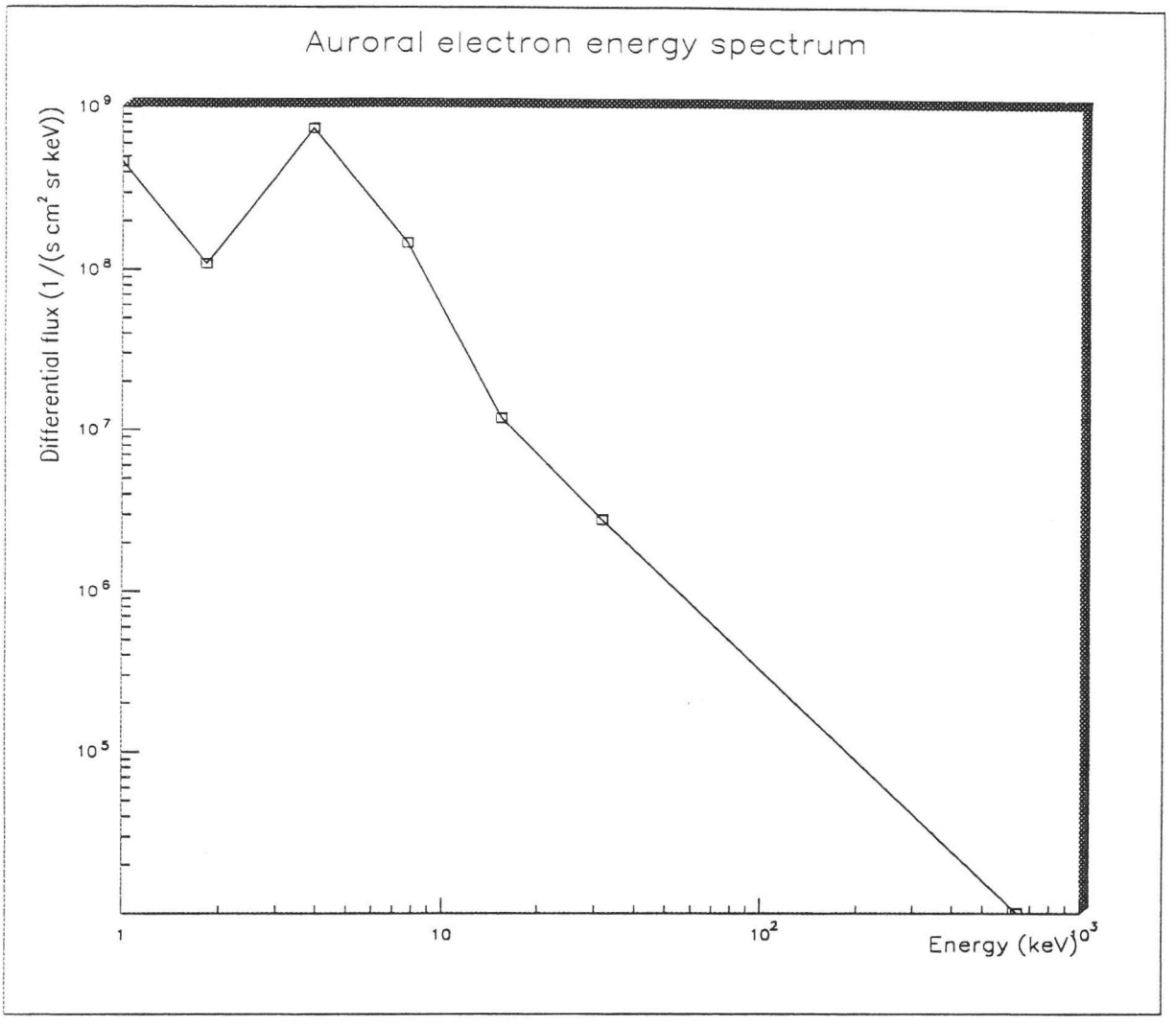

Figure 2.21: Typical electron energy spectrum at auroral latitude.

However, the paralysis problem can be partly solved, if the micro-processor (for data processing and experiment control) can accept telemetry commands to disable the very sensitive detectors when ØRSTED crosses the auroral region.

If the CPD paralysis problem is solved, the influence of pile-up on the observed spectrum can be predicted:

- If the pile-up probability is an order of magnitude below the normal detection probability, the discrepancy between the counts of P1 bins and E1 bins will just increase the error bars of the final results.
- If pile-up effects are not negligible, the pile-up process must be modelized as a function of the integral flux. Then the bin count rates may be directly calculated for any specific spectrum shape. The unfolding becomes model dependent.

2.5 The CPD and particle angular distributions

All the count rates estimations performed in the previous sections were based on the assumption that the particle fluxes on ØRSTED orbit were isotropic. When this assumption is no longer valid, the CPD bin detection efficiency must be computed as a function of angular coordinates of incident particle momentum. If, for example, one defines the polar angle θ_k as the angle between the particle momentum and the Z axis (parallel to the boom), and ϕ_k the azimuthal angle of the particle momentum, the count rates of Bin i is given by the general expression

$$N_i^k = \int_{\theta_{kmin}}^{\theta_{kmax}} \int_{\phi_{kmin}}^{\phi_{kmax}} \int_{E_{min}^k(\theta_k,\phi_k)}^{E_{max}^k(\theta_k,\phi_k)} p_i^k(E_k,\theta_k,\phi_k) J_d^k(E_k,\theta_k,\phi_k) \Gamma_k(E_k,\theta_k,\phi_k) dE_k d\theta_k d\phi_k \tag{2.4}$$

in which all the functions used in Equation 2.2 are replaced by their angular dependent counterparts.

It goes without saying that the use of Equation 2.4 is not only a time consuming task, but also may lead to erroneous results when it is used to fit experimental results, due to the elevated number of model parameters [12].
As a matter of fact, this model will be used only when dealing with orbital particle fluxes involving one kind of particle only [7]. In other cases, the count rates from detector P1 will be compared to the count rates from detector P2 in order to produce an isotropy index. The same holds for detectors E1 and E2.
The calculation of the angular dependent efficiencies is underway.

2.6 The CPD signal to noise ratio

The count rates given in Table 2.4 and 2.5 are valid only if no particle can reach the sensor(s) unless it passes through one of the detector entries. This condition is fulfilled if the components on any particle path to the sensor are thick enough to shield efficiently the later for all the particle energies encountered in significant number on ØRSTED orbit. We assume herein that, due to their generally high flux, electrons constitute the principal threat to the CPD signal to noise[1] ratio.

[1]The word *"noise"* is defined here as *"a signal sensed by the CPD, but not accounted for in the detection efficiency (see above)"*.

Among all the elements along particle paths, the satellite housing is the easiest structure (additional sensor shield) to modelize. To evaluate the efficiency of this structure in stopping the ill-directed particles, 10^8 electron events of sample energies have been initiated randomly on one of the satellite sides but the bottom one. The circular areas corresponding to the projection (parallel to the detector symmetry axis) of the detector entry to the satellite housing panels was marked and particles hitting the sensors from this area were recorded in "signal bins". Any other particle reaching a sensor was recorded in "noise bins". On simulation completion, all the bin contents were divided not by 10^8 but by this number majorated by the number of events (about 11. 10^6) initiated on the upper satellite side. This allowed us to spare about two hours for each simulated energy, since the particles which might be initiated at the bottom were not launched, as it is likely that they would not hit any CPD sensor.

Figure 2.22 shows the values of electron signal and noise efficiency for Bin1 of each upward-looking detector at seven energy values, whereas Figure 2.23 shows signal and noise detection efficiency for Bin 1 to 4 of E1, one of the detectors primarly dedicated to electron counting.

If the materials along the electron paths were equivalent, as absorbers, to a 2 mm thick aluminum shield (or a 3 mm thick delrin shield), they would stop up to 1 MeV electrons. However, the bremsstrahlung gamma from these shields seems to be the most disturbing source of noise in the detector sensors. Consenquently, though the contribution of electrons to the noise is reduced, it remains greater than the 1 MeV electron signal.

If the satellite total weight ($\sim$ 60 kg) was distributed over its outer surface ($\sim$ 14436 cm^2), the resulting housing thickness would be equivalent to a $\sim$ 1.5 cm thick aluminum plate. We have evaluated the probability to produce a signal in a (50 mm^2) sensor installed at 10 cm distance from one side, for an electron event initiated at the other side of a 1 cm thick aluminum plate. The electron energy was 1 MeV and its initial momentum was perpendicular to the sensor surface.

The result is that even in this favourable case, only 28 particles would hit the sensor for 10^7 electrons events initiated. None of these particles would deposit more than 60 keV in the sensor: the electron Bin 1 and 2 would be the most sensitive to such a kind of noise. During a 1 ms time interval in the auroral region, the maximum number of hits on E1 or E2 sensors would be: $\sim 10^8 \times \pi \times 14436 \times 28\ 10^{-7} \times 10^{-3} \approx 1260$ $hits$.
To evaluate the number of effective noise counts, this number must be corrected to take into account the true number of electrons of energy greater than 1 MeV (which was seen to be low in auroral zone).

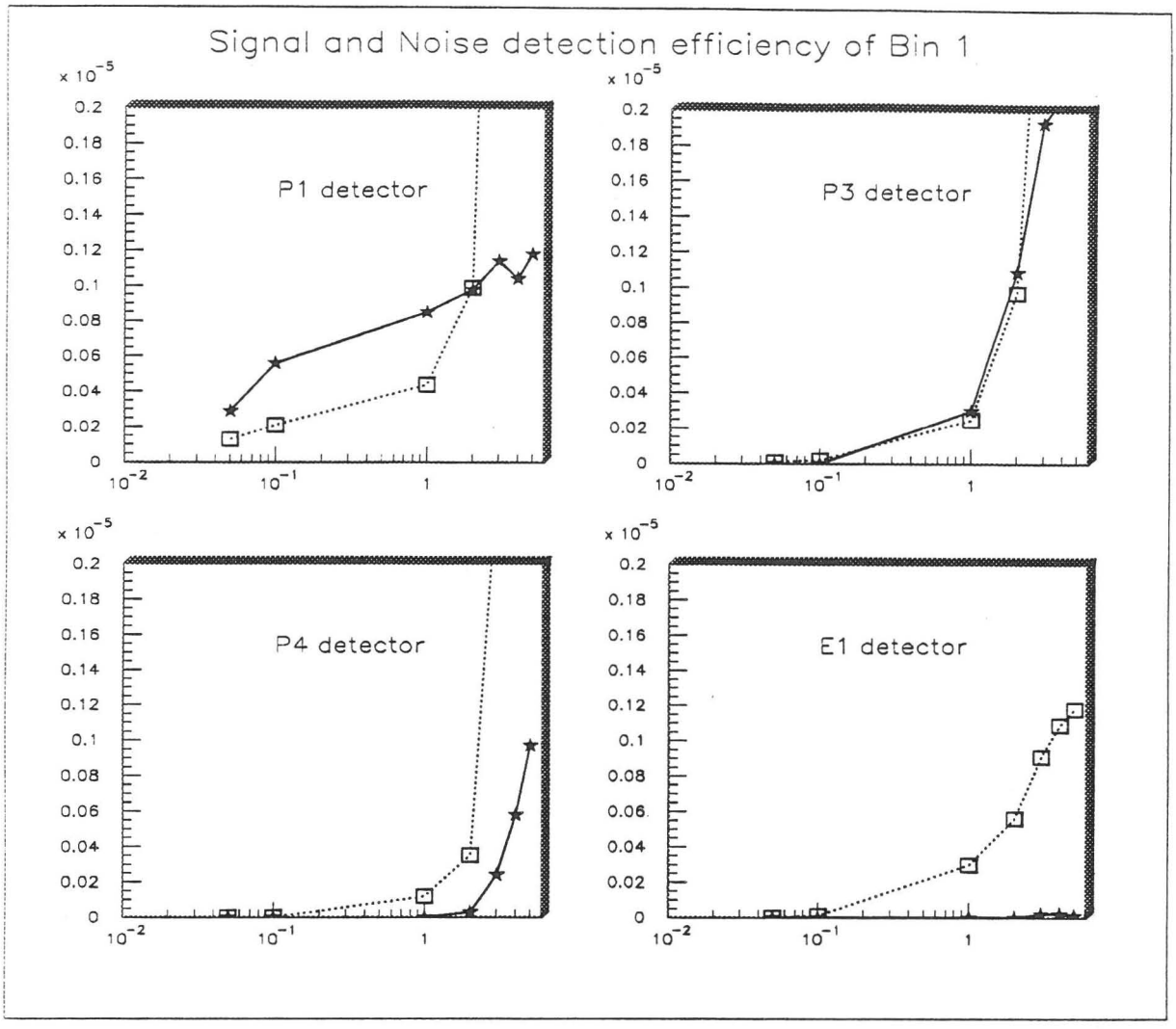

Figure 2.22: Electron signal (solid line) and noise (dotted line) contributions in CPD bins as a function of incident electron energy.

All in all, no significant background is to be expected from electrons if the materials inside ØRSTED are homogeneously distributed. Otherwise, the signal to noise ratio has to be experimentally determined or evaluated by simulations based on a more precise mass distribution model of the ØRSTED spacecraft.

We can conclude that the contribution of the materials inside the ØRSTED housing is necessary to improve the signal to noise ratio. An alternative way to reduce the noise level would be to make a more accurate description of all the mass elements inside ØRSTED and to calculate the appropriate detection efficiencies (of the whole satellite) to be used in both the Count Rate Prediction and the Data Analysis phases. But this is an extensive and very time consuming task which will only be undertaken if necessary, once the CPD data will become available.

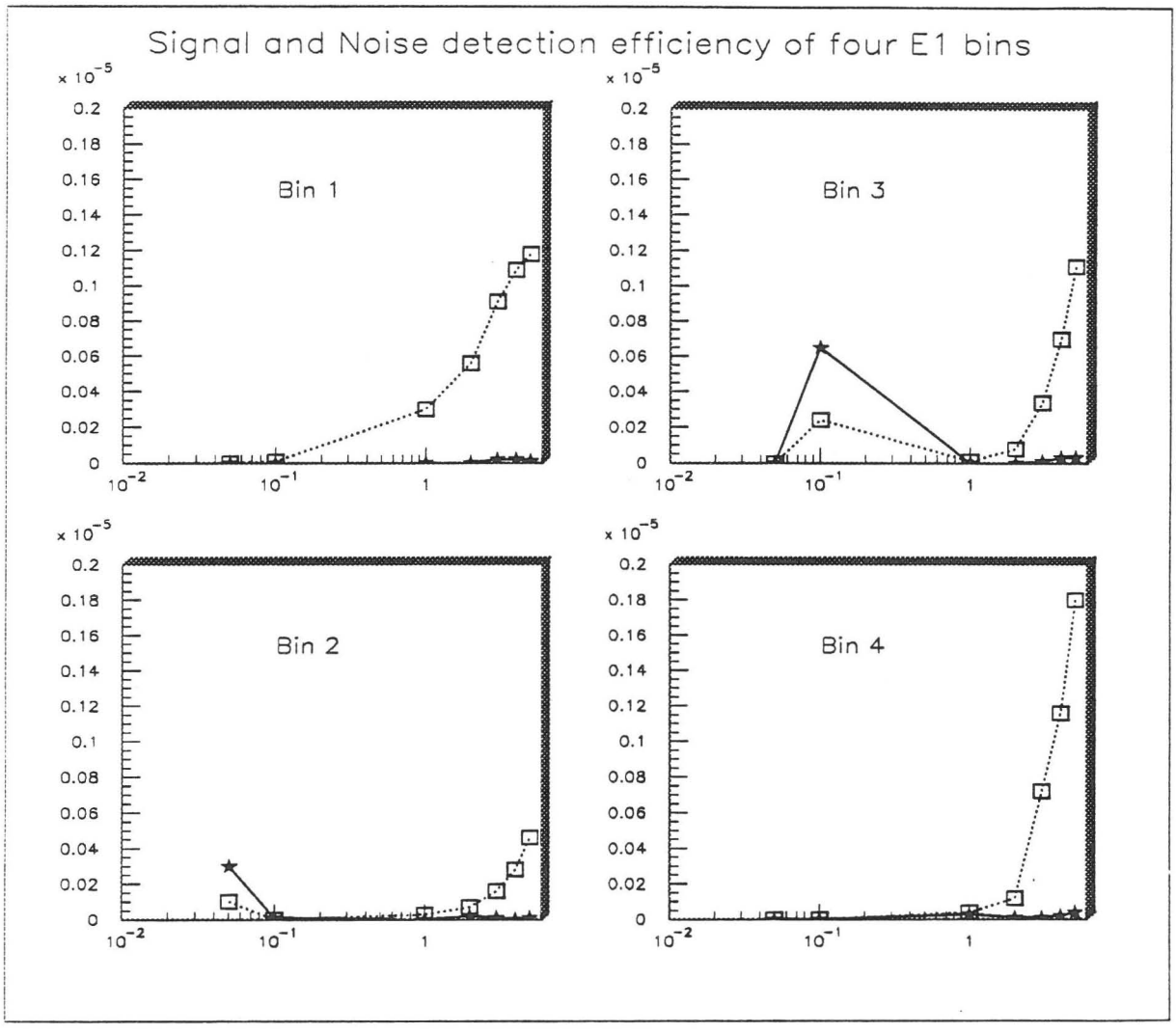

Figure 2.23: Electron signal (solid line) and noise (dotted line) contributions in Bin 1 to 4 of E2 as a function of incident electron energy.

Chapter 3

The expected CPD performance in spectrum discrimination

3.1 General Data Analysis Protocol

The parameters of the function $J_d^k(E_k)$ (see Equation 2.3) may be deduced from a least squares fit, if experimental bin counts N_i^{exp} are supplied. The function[1] to minimize is expressed as

$$f(C_k, \gamma_k, k = e^-, p, \alpha) = \sum_{i=1}^{40} (N_i^{exp} - N_i^{th})^2 \tag{3.1}$$

in term of symbols defined in Chapter 2.

Reliable solutions for C_k and γ_k will be obtained if the six variables are independent. This means it must be possible to solve the least squares problem and get parameters which are expressed as functions of bin counts only. This is not valid if the CPD bin counts contain contributions from different kind of particles. The guidelines to decide wheither a bin contains different contributions are as follows:

- It is generally acknowledged that the orbit averaged number of electrons in space environment is roughly by a factor 10^2, greater than the number of protons. In the same way, the on-orbit proton flux is considered as greater than the α-particle flux, though the intensity ratio may be less than 10^2.
- The CPD bin counting efficiency for a given kind of particle is sometimes, by a factor 10^3, greater than the detection efficiency for other kind(s) of particles contributing to this bin.

A particle will be considered as present (P) in a bin, if its detection efficiency in that bin is greater than 10^{-4}, no matter the flux value on orbit. A particle will be considered as a trace (t) in this bin, otherwise.

[1] This function will be replaced by the Chisquare function as soon as the probability law of the bin counts is determined.

Detector	Particle	Bin							
		1	2	3	4	5	6	7	8
P1	Electron	D	t						
	Proton	P	D	D	D	D	$\underline{t}$	$\underline{t}$	$\underline{t}$
	α	P	P	P	P	P	$\underline{D}$	$\underline{D}$	$\underline{D}$
P3	Electron	D	t						
	Proton	P	P	P	$\underline{t}$				
	α	P	P	P	$\underline{D}$				
P4	Electron	P							
	Proton	P	P	P	$\underline{t}$				
	α	P	P	P	$\underline{D}$				
E1	Electron	D	D	D	D	D	D	P	t
	Proton	P	P	P	P	P	P	P	P
	α	P	P	P	P	P	P	P	P

Table 3.1: Bin count estimates for each up-looking detector and particle type.

A particle will be considered as dominating (D) the bin, if its detection efficiency is a factor 10^2 greater than the efficiency for the other particles present in the bin. The fluxes for those other particles must be lower than or equal to the dominating particle flux.
A particle will be considered as dominating (D) the bin, if its flux is greater than the flux of the other particles present in the bin. The detection efficiency for those other particles must be lower than or equal to the dominating particle detection efficiency.

If particle a dominates the counts in bin i, as long as the flux for particle b is not more than 10^2 times a flux, then particle a will be considered as conditionnally dominating the bin i counts, and this will be symbolized by an underlined D ($\underline{D}$). The symbol for particle b in bin i will be an underlined "t" ($\underline{t}$), which means that b is present in bin i as a trace unless the flux for particle b compensates the poor detection efficiency.

Following those rules, an attempt was made to classify the CPD bins, in order to select the best particle discriminators among them. The results are summarized in Table 3.1.

In conclusion, the electron and proton discrimination is to be expected if some of the Bin 2 to 5 of P1 are not empty. α-particle spectrum is likely to be obtained if some of the Bin 6 to 8 of P1, Bin 4 of P3 and Bin 4 of P4 are not empty.
In other cases, only the electron spectrum may be obtained.

To achieve the chi-square[2] function minimization by the MINUIT code from the CERN program library, one proceeds as follows:

- A preliminary fit is performed in order to obtain the "initial" parameter values. This is done by using the critical bins enumerated above, if their counts are not zero.
- The obtained parameters are supplied to MINUIT as input for global fit. This results in the actual best spectrum likely to fit the experimental bin counts.

[2] A statistical analysis will be done in order to determine the uncertainty on the bin counts [13].

If no count was recorded in a a critical bin for a given kind of particle, guessed initial values of parameters may be used, but without guarantee for the final result.

Attempts to perform MINUIT minimization without the intermediate step decribed above have been often unsuccessful. This can be understood if one notices, as stated above, that a successful particle discrimination is guaranteed by the bins in which different particle types are not simultaneously present.

3.2 Case studies

3.2.1 Electron dominated environment

In order to check the experimental method outlined here, we have simulated counts induced by particles for which the energy spectrum model parameters are given in Table 3.2. Energy ranges were 0.01 to 5.0 MeV, 0.1 to 300.0 MeV and 0.1 to 500.0 MeV, for electrons, protons and α-particles, respectively. The calculated and simulated counts are shown in Table 3.3. One can notice that the bin count rates are quite well reproduced by the theoretical estimates using Equation 2.1 and 2.2.

Particle	C_k $(1/(s\ cm^2\ sr\ (MeV)^{(1-\gamma_k)})$		γ_k		$J^k(E > E_{min})$ $(1/s\ cm^2\ sr)$	
	Model	Fit	Model	Fit	Model	Fit
Electron	13000	12604	1.001	1.049	80911	84608
Proton	950	1690	1.85	2.18	7903	21675
α	790	12	2.	1.06	7898	91

Table 3.2: Model and fit parameters of the particle energy spectra on ØRSTED orbit.

The parameters obtained by least squares fit are shown in Table 3.2. We will see that the poor agreement between the expected results and those we got is due to the small numbers of recorded particles in some critical bins. One way to show this, is by assuming that proton and α-particle fluxes are 10 times more important, with the electron flux remaining the same as in Table 3.2 and perform a least squares fit again.

Equation 2.2			Simulated		
Detector	Bin	Counts	Detector	Bin	Counts
P1	1	3302	P1	1	3381
	2	8		2	12
	3	7		3	10
	4	5		4	8
	5	3		5	8
	6	1		6	4
	7	1		7	0
	8	3		8	4
P2	1	0	P2	1	1
	2	0		2	0
	3	0		3	0
	4	0		4	0
	5	0		5	0
	6	0		6	0
	7	0		7	0
	8	0		8	0
P3	1	1780	P3	1	1663
	2	3		2	5
	3	0		3	0
	4	0		4	1
P4	1	279	P4	1	324
	2	1		2	1
	3	0		3	0
	4	0		4	0
E1	1	76	E1	1	61
	2	161		2	138
	3	376		3	512
	4	531		4	719
	5	1518		5	1524
	6	581		6	583
	7	83		7	90
	8	40		8	34
E2	1	0	E2	1	0
	2	0		2	1
	3	0		3	0
	4	0		4	0
	5	0		5	0
	6	0		6	1
	7	0		7	1
	8	0		8	0

Table 3.3: Calculated and simulated CPD count rates for spectrum parameters of Table 3.2.

Detector	Bin	Counts	Detector	Bin	Counts
P1	1	5560	P1	1	5909
	2	90		2	92
	3	72		3	64
	4	66		4	58
	5	43		5	37
	6	17		6	14
	7	12		7	8
	8	31		8	41
P2	1	1	P2	1	3
	2	0		2	0
	3	0		3	0
	4	0		4	0
	5	0		5	0
	6	0		6	0
	7	0		7	0
	8	0		8	0
P3	1	1932	P3	1	1496
	2	37		2	32
	3	12		3	13
	4	5		4	5
P4	1	389	P4	1	523
	2	15		2	14
	3	5		3	8
	4	1		4	2
E1	1	120	E1	1	101
	2	219		2	199
	3	698		3	889
	4	878		4	1569
	5	2036		5	1963
	6	899		6	953
	7	396		7	321
	8	407		8	348
E2	1	0	E2	1	0
	2	0		2	1
	3	0		3	0
	4	0		4	0
	5	0		5	3
	6	0		6	1
	7	0		7	2
	8	0		8	2

Table 3.4: Calculated and simulated CPD count rates if proton and α flux are multiplied by 10.

Particle	C_k $(1/(s\ cm^2\ sr\ (MeV)^{(1-\gamma_k)})$	γ_k	$J^k(E > E_{min})$ $(1/s\ cm^2\ sr)$
Electron	10511	1.019	67246
Proton	14178	2.18	181843
α	5012	1.67	34873

Table 3.5: Parameters obtained by least squares fit if proton and α fluxes are multiplied by 10.

Particle	C_k $(1/(s\ cm^2\ sr\ (MeV)^{(1-\gamma_k)})$		γ_k		$J^k(E > E_{min})$ $(1/s\ cm^2\ sr)$	
	Model	Fit	Model	Fit	Model	Fit
Electron	1300	6411	1.001	1.486	8091	117643
Proton	28500	1015	1.85	1.28	237107	6173
α	7900	35269	2.	1.85	78984	293536

Table 3.6: Model and fit parameters for a proton dominated space environment.

The expected bin counts and the simulation results are shown in Table 3.4. The critical bins of P1 are now significantly different from zero.

Using MINUIT to fit the simulation bin counts, one gets the spectrum parameters listed in Table 3.5, which are in better agreement with the model ones. The energy spectra corresponding to these parameters are drawn in Figure 3.1.

3.2.2 Proton dominated environment

Many other cases have been considered including the case in which the space particle fluxes are dominated by protons. The input parameters and results are illustrated in the Tables and Figures below:

Parameters

Table 3.6 contains the model and least squares fit spectrum parameters.

Simulated bin counts

Table 3.7 contains the simulated count rate for the different bins.

Input/Output spectra

It is clear that the CPD failed to discriminate proton vs. α-particles, so much that proton spectrum parameters became *alpha*'s and vice-versa.

Detector	Bin	Counts
P1	1	5938
	2	213
	3	174
	4	147
	5	90
	6	19
	7	10
	8	37
P2	1	2
	2	0
	3	0
	4	0
	5	0
	6	0
	7	0
	8	0
P3	1	645
	2	77
	3	24
	4	3
P4	1	392
	2	32
	3	16
	4	3
E1	1	91
	2	339
	3	857
	4	1327
	5	1497
	6	1137
	7	795
	8	834
E2	1	0
	2	0
	3	0
	4	0
	5	0
	6	1
	7	2
	8	1

Table 3.7: Simulated CPD count rate for a proton dominated space environment.

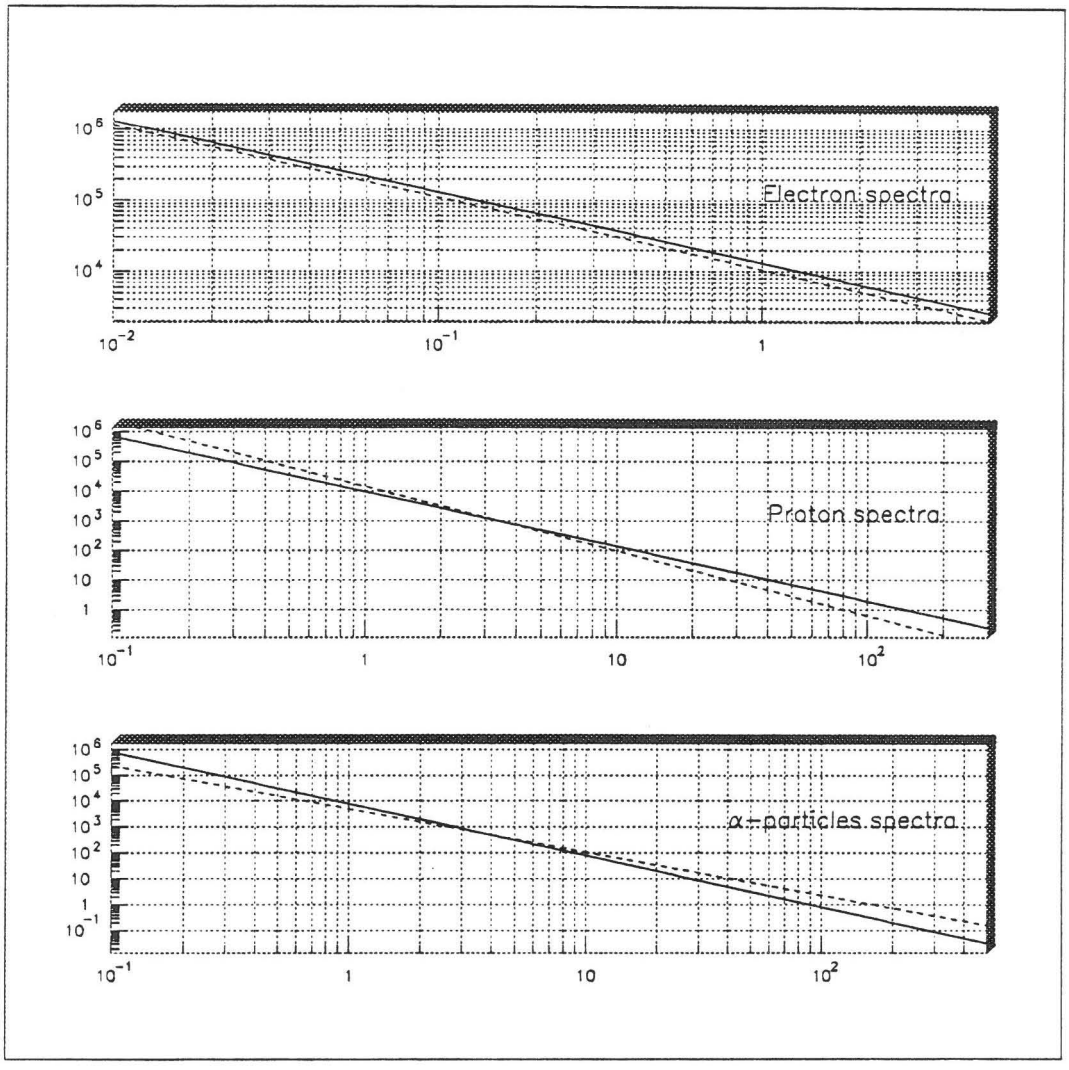

Figure 3.1: Comparison between the model spectrum (smooth line) and the spectrum resulting least squares fit (dashed line) in the case the proton and α fluxes are multiplied by 10. The curves represent the probability density function (ordinate) in function of the particle incident energy (abscissa).

Chapter 4

Conclusion

We have demonstrated throughout this study that:

1. The CPD accommodation on the ØRSTED satellite is such to ensure a direct comparison between fluxes of particles coming from two directions perpendicular to each other. Such a setup allows the generation of a Flux Asymmetry Index linked to the difference of count rates between perpendicular detectors. During the analysis this index will be used to switch between isostropic and anisotropic flux models.

2. Using the GEANT simulation code from the CERN program library, we have calculated the detection efficiency for each CPD channel and each particle type for isotropic fluxes and "background-tight" satellite assembly. These efficiencies have been (and will be) used in count rate predictions and analysis. The method to calculate efficiencies and to perform predictions and analysis when the particle fluxes are anisotropic have been described. We described also a method to take into account the background and possible pulse pile-up effects which may result from the high electron flux values encountered on ØRSTED orbit in auroral zones.

3. Case studies have shown that particle discrimination and energy spectrum analysis will be possible in case of isotropic particle fluxes. Angular distribution analysis is possible in principle but strongly depends on the number of model parameters and orbital position.

The CPD is ready to operate when the particle flux does not paralyse its electronics (due to an excessive particle impact rate on a sensor). Angular dependent efficiencies are currently calculated and, though they necessitate much CPU time, they should be completed before the first CPD data become available.

The only task awaiting the CPD co-Investigators will now be to check (experimentally or numerically) the shielding capability of the satellite, for particles which do not enter the CPD through the detector aperture.
In case the satellite does not shield efficiently the CPD sensors, new efficiency functions must be calculated.

Bibliography

[1] M.S. Gussenhoven et al., *Space Radiation Dosimeter SSJ* for the Block 5D/Flight 7 DMSP Satellite: Calibration and Data Presentation*, Technical Report, 20 March 1986.

[2] J. Lemaire et al., *The Scintillating Fibre Detector (SFD)*, Technical Note A, BISA/UCL, January 1997.

[3] P. Bühler et al., *Monitoring of the Radiation Belts with the Radiation Environment Monitor REM*, Workshop on Trapped Radiation Belts, Geophysical Monograph, (1996).

[4] E. Friis-Chistensen and C. Scøtt, *Øersted Compendium, Contributions from the International Science Team*, DMI Scientific Report: 97-1, Denmark May 1997.

[5] Glenn F. Knoll, *Radiation detection and measurement*, John Wiley & Sons, Inc. (1979).

[6] Heynderickx, D., M. Kruglanski and J. Lemaire, *UNIRAD v3.0: Trapped radiation software*, ESTEC, (1996).

[7] E.G. Mullen, M.S. Gussenhoven and D.A. Hardy, *Proceedings of NATO Advanced Study Institute, "Terrestrial Space Radiation and its Biological Effects"*, Corfu, Greece, 11 - 25 October 1987.

[8] James C. Ulwick, McCormac, B.M. (ed.), *Aurora and Airglow*, Reinhold Publishing Corporation, New York, pp. 225-237, (1967).

[9] David S. Evans, McCormac, B.M. (ed.), *Aurora and Airglow*, Reinhold Publishing Corporation, New York, pp. 191-209, (1967).

[10] M.S. Gussenhoven et al., *Journal of Geophysical Research*, vol. 90, no. A11, pp. 11009-11023, (1985).

[11] B.J. O'Brien, Walt, M. (ed.), *Aurora Phenomena*, Stanford University Press, Stanford, California, pp. 84-98, (1965).

[12] Kruglanski, M., and J. Lemaire, *Trapped proton anisotropy at low altitudes*, Trend Technical Note 6, ESTEC, (1996).

[13] V. Pierrard, *Thèse annexe*, UCL/ASTR, Février 1997.

[14] J.F. Ziegler, *SRIM (Stopping and Range of Ions in Matter) and TRIM (Transport of Ions in Matter) programs based on Ziegler's tables*, downloadable from http://www.research.ibm.com/ionbeams/SRIM/SRIMINTR.HTM.

[15] Gh. Grégoire, *VRANGE and VSTOP are range/stopping power programs based on Ziegler's tables, Williamson's tables and Hubert's tables (See references hereafter)*; private communication.

[16] CERN, *GEANT Version 3.21/05 Released on 15.03.96.*

[17] C. Williamson et al., *Saclay report*, CEA-R3042 (1966).

[18] Hubert et al., *Annales de Physique*, vol. S-5 (1980).

List of Figures

List of Tables

Appendix A

The High Energy Charged Particle Detector Experiment

ØRSTED High Energy Charged Particle Detector Experiment

Peter Stauning, Solar-Terrestrial Physics Division, DMI

Peter Davidsen, Computer Resources International (formerly DMI)

Abstract The ØRSTED solid-state, high-energy, charged particle detector (CPD) experiment is aiming at the detection of electrons within the energy range from 30 keV to >1 Mev and protons and α-particles from 250 keV to >30 MeV.
A primary purpose of the satellite particle experiment is to provide measurements of the energetic particle radiation in the upper polar atmosphere to be combined with absorption data from imaging riometer installations on the ground in order to detect the dynamical features of polar and auroral particle precipitation events.
A second objective for the mission is to conduct monitoring of the level of solar-geophysical activity during events, like major solar flares and geomagnetic storms, where intense and variable high-energy particle radiation may occur.
A third feature of the proposed experiment is the monitoring of the long-term high-energy particle radiation dose at the satellite for investigations of possible radiation damages on other on-board experiments and systems.

1. Scientific background.

Large flares at the Sun and magnetic storms and substorms in the Earth's magnetosphere may generate intense radiation of high-energy charged particles, mostly electrons, protons and α-particles. This high-energy radiation is an important element of the fundamental physical processes at the sun, in the interplanetary space and in the near-earth space. The high-energy charged particles are important in a number of research fields such as solar wind-magnetosphere-ionosphere-atmosphere coupling processes, and geomagnetic morphological problems like the distinguishing between 'open' and 'closed' magnetospheric regions. The high-energy particles are also important for substorm generation and dynamics and for various aspects of upper atmosphere conditions.

The high-energy charged particles of solar or magnetospheric origin are lost by precipitation into the atmosphere. The precipitation is particularly intense in the polar and auroral regions where the energetic radiation frequently produces substantially enhanced ionization at low altitudes. Such ionization can cause black-out of HF radio communication circuits used a.o. for the air and sea traffic. In addition to causing ionospheric absorption of radio waves the energetic particle radiation may have various other effects, for instance, on space systems, and on the environment. The high energy radiation during large solar flares may cause severe damage on spacecraft systems in particular on solar panels and complex electronic systems. The high energy particle precipitation increases the conductivity of the atmosphere thereby changing its global electrical properties. The precipitation may even produce modifications of the lower atmospheric chemistry and composition e.g. the nitric-oxide and ozone abundances. The high-energy precipitation events offer essential advantages for atmospheric observations. The ionization produced at low altitudes makes the upper atmosphere 'visible' for electromagnetic probing and thus enable various forms of radar observations of winds and turbulences in the 'middle atmosphere' which is difficult to explore by other methods.

2. Charged particle detector instrument.

Figure 1 presents a photo of the Charged Particle Detector (CPD) instrument. The box contains all the electronic circuits involved in the experiment, that is, high-voltage supply for the solid state detectors, charge-sensitive preamplifiers, pulse amplifiers, discriminators, counter circuits, and a computer system based on the intel 80186 processor circuit.

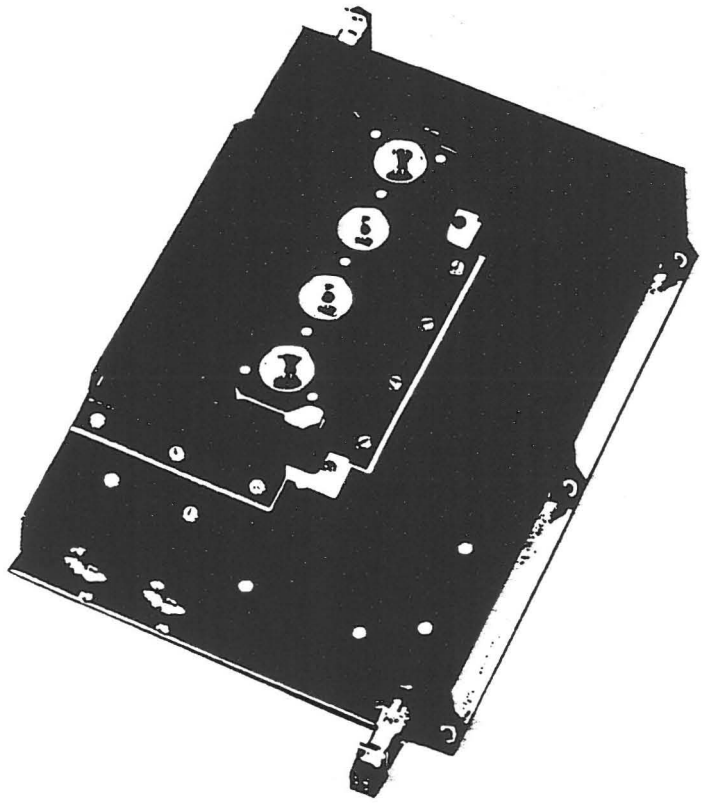

Figure 1. Photo of the Charged Particle Detector instrument for the Ørsted satellite.

2.1 Summary of characteristics of high-energy charged particle detector experiment

The charged particle detector (CPD) experiment measures the fluxes of high-energy electrons and ions using an array of 6 solid-state detectors with different shieldings and depletion depths. Four of the detectors look upward in the direction of the mast. Two detectors look to the side. The instrument has been constructed at the Danish Meteorological Institute. PI for the experiment is *P. Stauning*, DMI. Technical manager is Peter Davidsen (now CRI).

Overall max. dimensions:	260 x 199 x 113 mm
Total mass:	2.3 kg
Total power consumption:	1.0 Watts
Energy ranges:	
Electrons:	30 keV - 1 MeV
Protons:	250 keV - 30 MeV
Alpha particles:	1 - 100 MeV
Analyzer levels:	
4 detectors:	8 energy levels, logarithmically spaced
2 detectors:	4 energy levels
Temporal resolutions:	
Very high speed:	5 samples/sec (selected locations)
High speed:	1 sample/sec (auroral latitudes)
Moderate speed:	0.5 sample/sec (polar cap)
Low speed:	0.1 sample/sec (low latitudes)

Table 1. Summary technical data for the CPD experiment.

2.2. Detectors The proposed experiment uses a set of solid-state silicon surface barrier detectors. Each solid state detector has response functions to incoming particles of different kinds and various energies as shown by the curves in Figure 2.

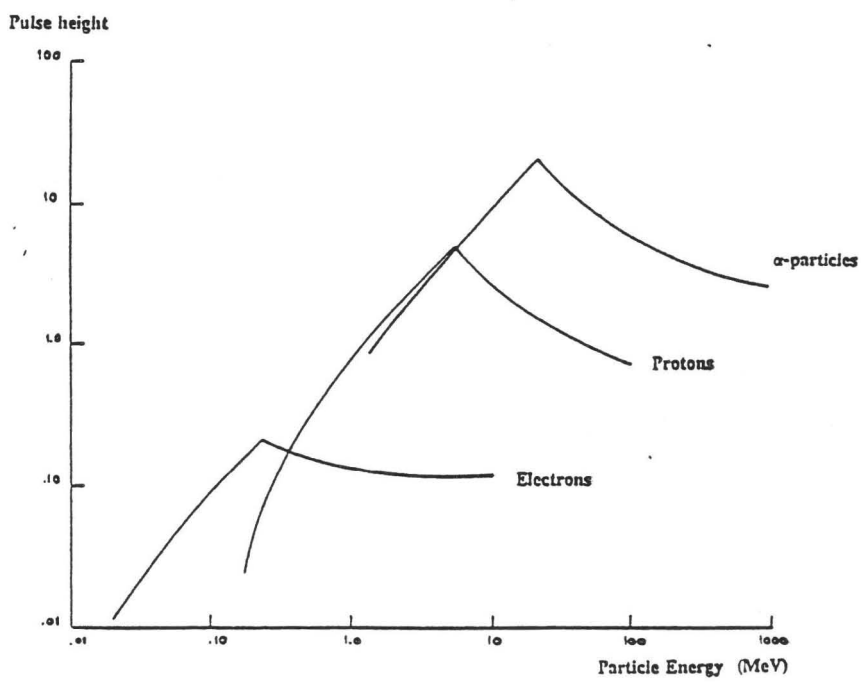

Figure 2. Solid state detector characteristics.

Power subsystem
The power subsystem is comprised of the following elements:

- A solar array, consisting of five solar panels. Each panel is composed of 2 x 4 cm GaAs solar cells with micro-sheet cover glass. The array delivers 54 watts average at End-Of-Mission.

- Two NiCd battery units, each with a 6 Ah capacity. A 15 % depth of discharge is foreseen during eclipse operations.

- Two power control units are included with redundant battery charge regulators, central DC/DC converters, and load control/protection devices.

- Available outputs: ±5 V, ±8 V, +15 V and the unregulated power bus. Controlled disconnection of loads is included for the protection of the power subsystem itself.

Communication
The communication system is redundant in order to ensure communication to and from the satellite with a very high reliability. Its characteristics are:

- S-band communication (down link 2039.6 MHz, up link 2215 MHz) with two turnstile communication antennas mounted on the earthpointing side of the satellite.

- Science data accumulation rates are approximately 1 kbit/sec in normal mode, and 6 kbit/sec in burst mode.

- Telemetry down link is equipped with Reed-Solomon concatenated and convolutional encoding.

- Telecommand up link includes Bose-Chaudhuri - Hocquenghem encoding.

- ESA packet standards PSS-04-106 (Telemetry) and PSS-04-107 (Telecommand) have been adopted for the Ørsted mission.

Command and Data Handling
The Command and Data Handling (CDH) subsystem is responsible for all onboard data processing, performing

- housekeeping data acquisition and processing
- science data acquisition and storage
- time management
- data memory management
- data compression
- TM and TC format management
- TC validation, distribution and execution
- attitude control processing

The CDH subsystem is comprised of two Central Processing Units each equipped with an Intel 80186, 16 MHz processor. It contains 16 Mbytes of RAM data storage which is sufficient for 13 hours of continuous operation. Data error detection and correction circuitry are included in the CDH.

Attitude control

Attitude control is provided to perform detumbling after separation from the launch vehicle and to ensure stabilization during the operational phases of the mission. Attitude determination is based on inputs from the star imager, sun sensors, and the CSC magnetometer. Attitude control is performed in a way which creates minimum disturbances to magnetic field measurements.

Stabilization of the satellite attitude is accomplished by passive and active techniques. The passive technique employs gravity-gradient stabilization using the deployed boom with a tipmass of 3.1 kg from the two magnetometers and the star imager. The active technique uses three-axis magnetorquer coils interacting with the Earth's magnetic field. The ACS maintains a yaw angle variation of ± 10 degrees to optimize the power output of the solar panels.

Ground Equipment

Ground Support Equipment used for Ørsted has been designed with the following key considerations:

- The Core EGSE is built from a commercial product (EasyMAP)
- Subsystem specific test equipment is to be integrated via standardized I/Fs
- Adoption of ESA Space Standards
    - Packet TM/TC standards
    - Packet Utilization Standards (PUS)

Starting from a cut-off energy defined by the front shield and detector contact material (normally Au or Al deposit) each incoming energetic particle creates an ionized track in the depleted layer of the reverse biased semiconductor diode. The generated free charge amounts to 1 electron-hole pair for each 3.6 eV of energy lost by the primary particle. The charge is collected due to the large reverse bias of the diode layer and fed to a charge-sensitive (integrating) pre-amplifier, that produces an impulse of amplitude proportional to the charge, that is, to the energy of the primary particle. At some energy level the pulse height maximises as the energetic particle just penetrates the depleted layer. At larger energies the pulse height decreases as the length of the track remains constant while the ionization efficiency decreases with increasing energy of the penetrating particle.

2.3 Detector array

The ØRSTED Charged Particle Detector (CPD) experiment comprises an array of 6 silicon solid-state detector units (D1 - D6). A sketch of the CPD experiment is shown in Figure 3. A more detailed drawing with dimensions (in mm) of the box and detector mount is shown later.

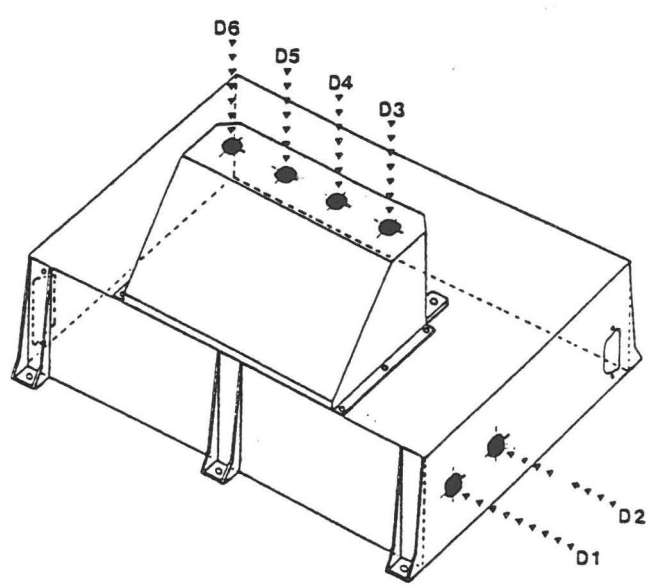

Figure 3. Sketch of ØRSTED charged particle detector experiment box.

Two detectors (D1, D2) are mounted to look horizontally while the remaining four (D3 - D6) are mounted to look vertically upward in the direction of the satellite mast carrying the magnetometers. The detectors have different characteristics and shieldings to provide discrimination between α-particles, protons, and electrons. One pair labeled P1 and P2 (D6, D1) of identical detector units looking vertically upward and horizontally, respectively, are primarily used for α-particle and proton detection. They use 300 μm depletion layer detectors shielded by 0.75 μm nickel foil. Another pair of identical detector units labeled E1 and E2 (D3, D2) looking vertically upward and horizontally, respectively, are intended primarily for electron detection. They use 1000μm depletion layer detectors shielded also by the 0.75 μm nickel foil. The remaining two detector units labeled P3 and P4 (D4, D5) are mounted to look upward and use 300 μm depletion layer detectors with heavier shielding to discriminate against lower particle energies in order to detect the fluxes of particles of higher energies.

The two detector types have the following basic characteristics:

Detector model	TB-016-050-1000	TU-011-050-300
Detector type	Totally depleted	Ion-implanted
Sensitive area	50 mm^2	50 mm^2
Depletion depth	1000 μm	300 μm
Noise width	9 keV (FWHM)	3.2 keV (FWHM)
Alpha resolution	16 keV (FWHM)	11 keV (FWHM)
Operating bias	200 volts	100 volts

Table 2. Basic detector characteristics

2.4 Specifications of detector assembly characteristics

Referring to the detector numbering defined in Figure 3 the characteristics of the detector array elements are.

Detector: P1

Look direction:	90° (vertically upward)
View cone half angle:	12.9°
Aperture:	0.20 cm^2
Geometric factor:	0.031 cm^2ster
Shield:	0.75 μm nickel foil
Detector:	EG&G Ortec type ULTRA U-011-050-300-T
Threshold energies:	
α-particles:	900 keV
protons:	250 keV
electrons:	30 keV
Peak (penetration) energies:	
α-particles:	24 MeV
protons:	6 MeV
electrons:	290 keV

Detector: P2

Look direction:	0° (horizontally)
Otherwise like P1	

Detector: P3

Look direction:	0° (vertically upward)
View cone half angle:	25.7°
Aperture:	0.28 cm^2
Geometric factor:	0.18 cm^2ster
Shield:	1 mm Al
Detector:	EG&G Ortec type ULTRA U-011-050-300-T
Threshold energies:	
α-particles:	52 MeV
protons:	13 MeV
electrons:	770 keV
Peak (penetration) energies:	
α-particles:	76 MeV

protons:	19 MeV
electrons:	1 MeV

Detector: P4

Look direction:	0° (vertically upward)
View cone half angle:	25.7°
Aperture:	0.28 cm^2
Geometric factor:	0.18 cm^2ster
Shield:	1 mm Cu
Detector:	EG&G Ortec type ULTRA U-011-050-300-T
Threshold energies:	
α-particles:	100 MeV
protons:	24 MeV
electrons:	1.9 MeV
Peak (penetration) energies:	
α-particles:	124 MeV
protons:	30 MeV
electrons:	2.2 MeV

Detector: E1

Look direction:	90° (vertically upward)
View cone half angle:	12.9°
Aperture:	0.20 cm^2
Geometric factor:	0.031 cm^2ster
Shield:	0.75 μm nickel foil
Detector:	EG&G Ortec type B-016-050-1000-T
Threshold energies:	
α-particles:	900 keV
protons:	250 keV
electrons:	30 keV
Peak (penetration) energies:	
α-particles:	48 MeV
protons:	11 MeV
electrons:	650 keV

Detector: E2

Look direction:	0° (horizontally)
Otherwise like E1	

2.5 Electronic units

A simplified block diagram of the experiment is shown in figure 4. The 6 detector units are connected to charge-sensitive pre-amplifiers. Small capacitors in parallel with the detectors provide circuits for injection of calibration pulses to the front end of the amplifiers. The energy-dependent pulses from the 4 narrow-angle detector units, P1, P2, E1, and E2, are fed to 8-level pulse-height analyzer circuitry. The pulses from the 2 wide-angle detectors, P3 and P4, are fed to simpler 4-level analyzers.

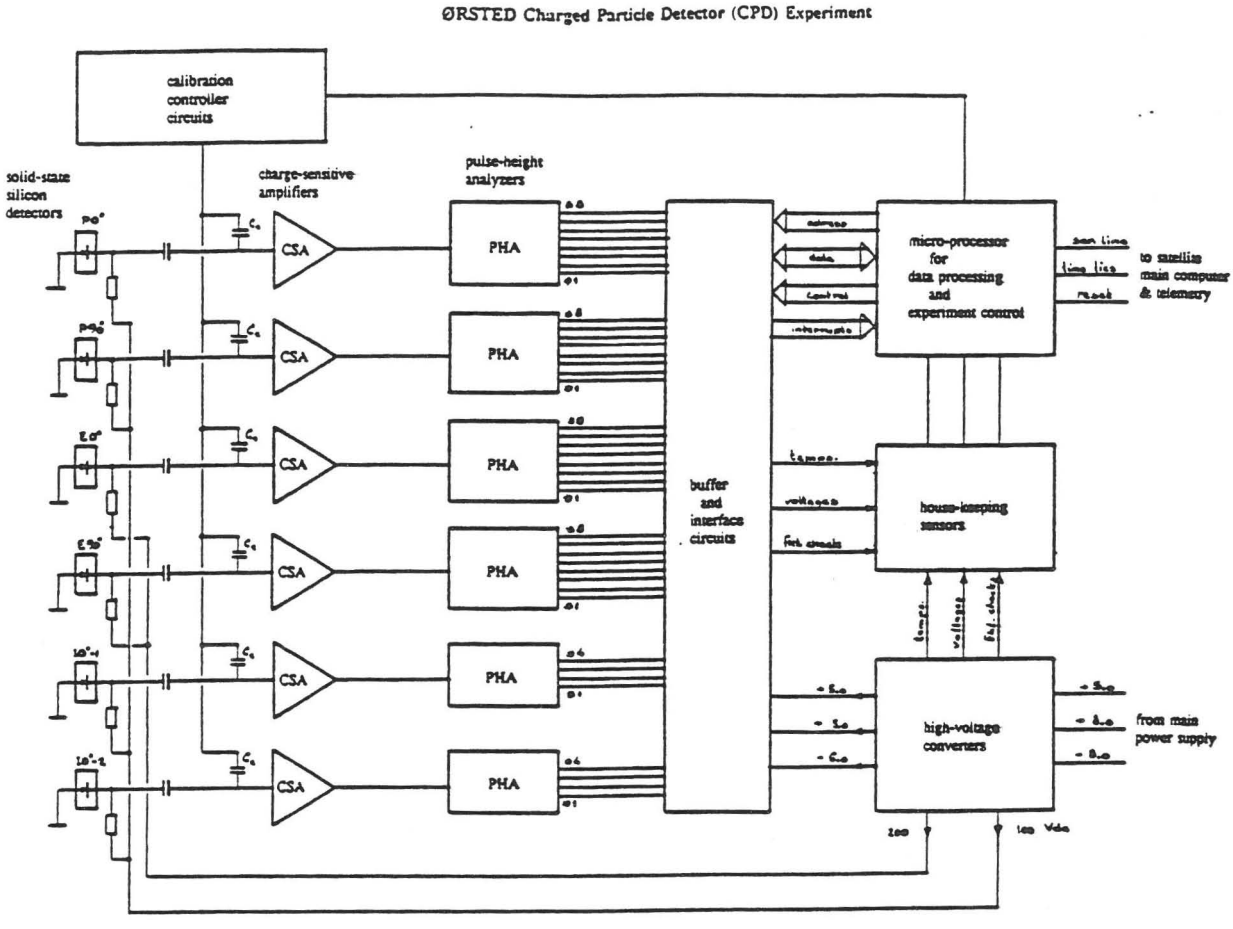

Figure 4. Simplified electric block diagram of particle experiment.

For the 'proton' detectors (P1, P2, P3, P4) there is one channel above penetration energy for protons (i.e. exclusively for high-energy α-particles). The lowermost channels are placed just below the electron penetration energy level. The remaining 6 or 2 channels are spaced logarithmically evenly between these upper and lower levels.

For the 'electron' detectors (E1, E2) there is one channel above the penetration energy for electrons (i.e. exclusively for high-energy protons and α-particles). The lowermost channels is placed at an energy level of ~ 30 keV deposited in the detector. The remaining 6 channels are spaced logarithmically evenly between these upper and lover levels.

The detector and 8-level analyzer circuits are shown in more detail in Figure 5. From the charge-sensitive preamplifiers the signals are fed to a pulse amplifier with adjustable gain. The output from this unit is connected both to the next pulse amplifier and to all inverting inputs of a quad voltage comparator integrated circuit. The 4 non-inverting inputs of the quad comparator are connected to a voltage divider chain to provide a set of spaced reference voltage levels. Additional fed-back resistors from the comparator outputs to the reference inputs provide some hysteresis to improve the output pulse shaping. The comparator output pulses are connected to 8-bit binary counter circuits with 3-state outputs. The output from the second pulse amplifier is similarly connected to a quad voltage comparator circuit to provide 4 additional analyzer levels. The output pulses from these comparators are connected to 8-bit binary counter circuits.

The structure of the data communication lines between the pulse-height analyzers and the

processor is bus-like. The counter outputs are coupled in parallel to the 8-bit input data bus. By controlling the 3-state enable lines any counter may be selected for read-out to the experiment processor. The data and control lines are be managed by PIO circuits of the 8255 type.

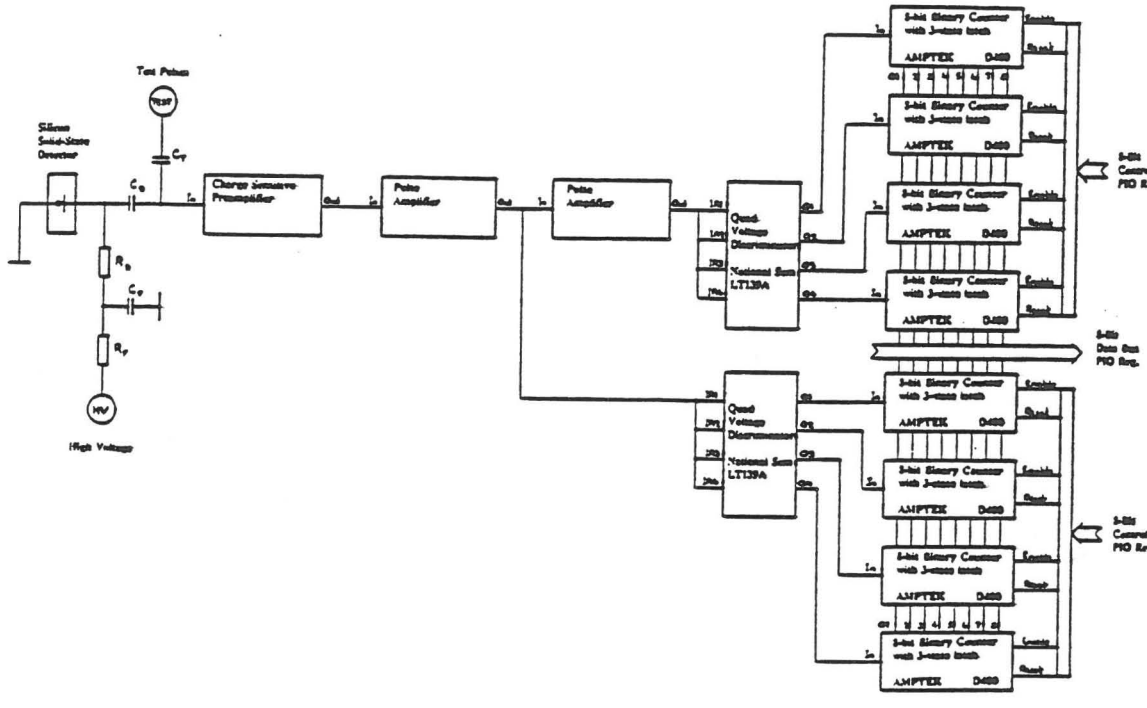

Figure 5. Solid-state detector pre-amplifier and pulse-height analyzer circuits.

The experiment microprocessor samples all available 40 channels at rates up to 5 samples/-sec. The processor unit must manage the read-out of pulse counters, data sorting and scaling and it should initiate and check calibration sequences. The processor should also conduct the collection and control of house-keeping parameters and finally it must communicate with the satellite main computer to send data and receive commands. The micro-processor circuit to be used for the particle experiment is intel 80186 which is the same as that of the satellite main computer system (CDH).

The calibrator unit is controlled by the experiment microprocessor. Start of calibration and the number of pulses generated at a preselected rate of 10^4 s^{-1} can be remotely programmed to any value. The calibrator pulse level may be set to any one of 1024 steps by the remotely programmed microprocessor. Any sequence of calibrator pulse numbers and levels can be generated.

Typically, a sequence will consist of a fixed number of pulses generated at each step of a steadily increasing amplitude from near zero up to a maximum value well above the uppermost analyzer level. These calibrator pulses will arrive in parallel with the pulses generated by the particle radiation. The calibration pulses are alternately turned on and off in order to distinguish the calibration pulses from the particle counting. This sequence is repeated twice for each calibrator level.

The supply voltages provided by the satellite power supply for the CPD experiment are +

and - 8.25 VDC and +5.0 VDC (nominally). The internal voltage regulators in the experiment provide stabilized voltages of +6.0 VDC and -5.0 VDC for the signal amplifiers and the pulse height analyzers. Bias voltages of +100 VDC and +200 vdc are produced by regulated voltage converters for the silicon detectors.

2.6 Mechanical assembly

The charge-sensitive pre-amplifiers, the pulse analyzer and calibration circuits, the microprocessor circuits, the converters, and the two side-looking detector units are housed in a box of (outer) dimensions 260 x 175 x 55 mm. The four up-looking detectors are mounted in a compartment on top of the box. The appearance of the box and the overall dimensions are given in Figure 6.

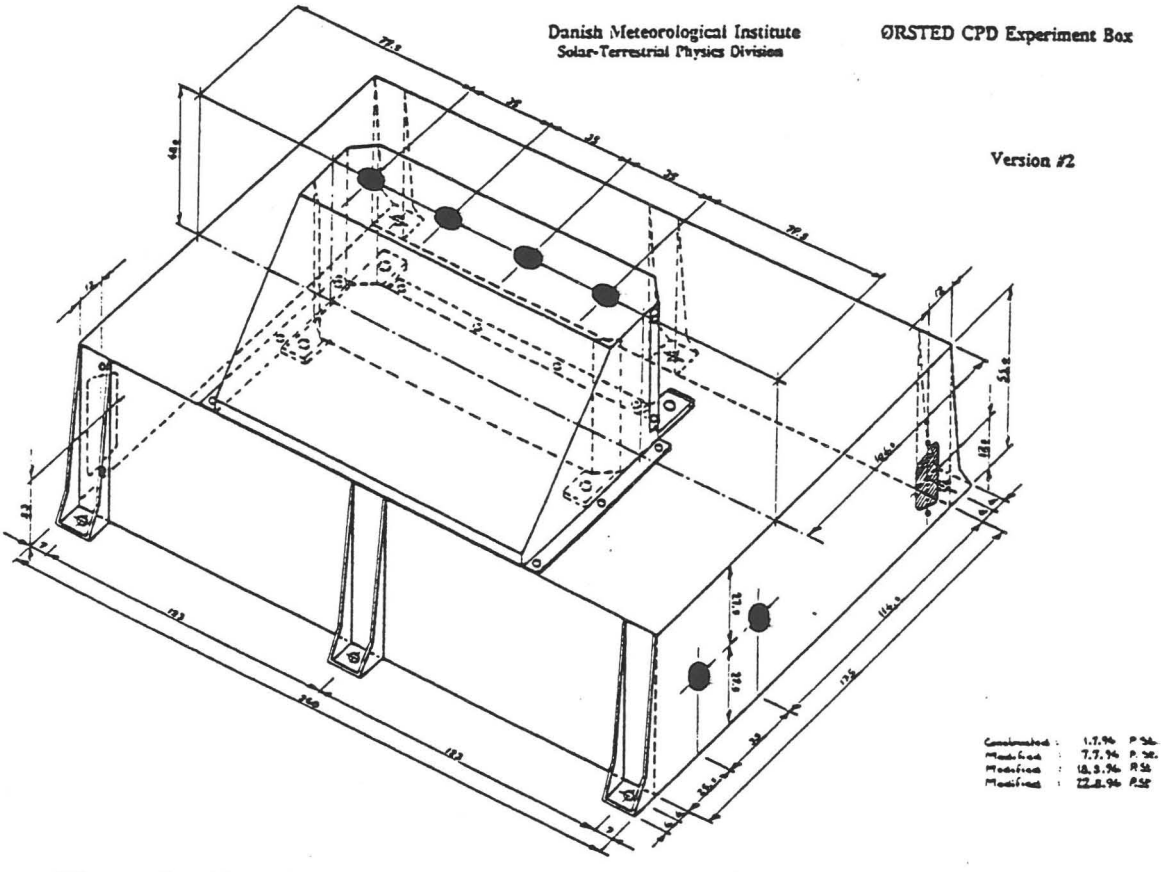

Figure 6. Experiment box outline. Detector orientation.

The two sensor assemblies mounted inside the box are looking out through holes drilled in the sides of the box. The box is mounted on top of the upper platform of the Ørsted satellite structure. For the 0° detectors looking along the satellite axis it is unavoidable to have the longerons of the magnetometer boom within field of view. This construction, however, is so light, that it produces a small pertubation only.

The mounting of the top compartment is shown in Figure 7 in a cross-section for one of the narrow-beam detector assemblies. The side-looking detector mounts are nearly the same except there the top cover in aluminum of 1 mm thickness is replaced by the box wall made of 2 mm Al. The wide-angle detector mounts are a little simpler (one collimator segment less), but they use otherwise the same principles.

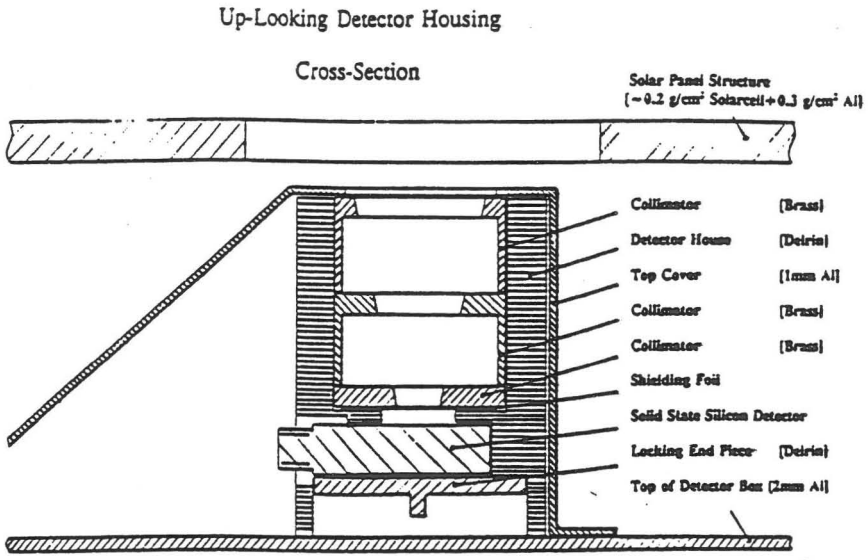

Figure 7. Cross-section of mount of up-looking narrow-beam detector assembly.

3. Data Collection

3.1 Data sample rates

The experiment has a total of 40 detector/level counter channels. To make the experiment flexible, the detector data should not be processed more than strictly neccessary on-board the satellite. The count rates are safely represented in 12-bit words (8 bits for the mantissa and 4 for the exponent in a logaritmic representation). Not including the house-keeping data, a complete scan would thus require 40 words of 12 bits i.e. 480 bits or 60 bytes of each 8 bits.

Corresponding to different operational modes there will be 4 different data sampling modes.

(i) Very high-speed.
During passes over one of a few selected locations a very high time resolution is desired in order to achieve a good spatial resolution in the particle fluxes. The sampling interval is then .2 seconds corresponding to a data rate of approx. 300 bytes/sec i.e. 2400 bits/sec. This time step corresponds to a horizontal distance of 2 km and should be maintained over at most 400 km of the orbit.

(ii) High speed.
When passing through the auroral regions at geomagnetic latitudes of 60° to 70° then a time resolution of approx. 1 sec. is selected. The data rate is now approx. 60 bytes/sec. This happens approx. during 12 minutes of each orbit i.e. the total amount of data is approx. 40.000 bytes each orbit.

(iii) Moderate speed.
At very high, polar latitudes above 70° geomagnetic latitude a time resolution of approx. 2 sec would be satisfactorily. The data rate in this mode is approx. 30 bytes/sec. For a true polar orbit this would happen appr. during 25 min. of each orbit, and a total amount of

45.000 bytes would be collected each orbit.

(iv) Low speed.

At middle or low geomagnetic latitudes below 60° a time resolution of approx. 10 seconds will be sufficient and a data rate of approx. 10 bytes/sec is anticipated. During the appr. 60 min. of each orbit spent in this mode a total of 36.000 bytes will be collected.

These 4 different modes of operation are summarized in Table 3

Operational mode	Condition	Sample interval
Very high speed	Selected positions	0.2 sec
High speed	Auroral latitudes (60-75°)	1 sec
Moderate speed	Polar latitudes ($\Phi > 75°$)	2 sec
Low speed	Low latitudes ($\Phi < 60°$)	10 sec

Table 3. Operational modes for particle experiment.

The data from the CPD experiment are first communicated via the RS485 data line to the CDH main computer and stored for occasional transmission to ground during passes close to the ground station. The choice of mode is defined by time-tagged commands issued regularly from the control center and uploaded to the satellite. The times for shifting between the latitude-dependent modes are calculated from the orbital information and a relatively simple magnetic field model like the eccentric dipole model or the corrected geomagnetic latitude model. The high-speed mode should be selected whenever the satellite passes over one of a set of specific positions corresponding to the locations of imaging riometer installations and incoherent scatter radars. The most important locations are listed in Table 4.

Station Name	Location	Geographic latitude	Geographic longitude	Invariant latitude	Installation month	Installation year	No.of beams	Operated by
Danmarkshavn	Greenland	76.77N	341.37E	77.29	Sep	1992	64	DMI, NIPR
Gulkana	Alaska	62.88N	214.85E	63.49	planned		164	UofM, APTI
Iqaluit	Canada	63.80N	291.40E	73.35	Sep	1992	49	UofM
Kilpisjärvi	Finland	69.05N	20.79E	65.90	Aug	1994	49	UofL, SGO
Longyearbyen	Svalbard	78.20N	15.80E	75.09	Aug	1995	64	DMI,UNIS,NIPR
Ny Ålesund	Svalbard	78.92N	11.92E	76.07	Sep	1991	64	STEL
Poker Flat	Alaska	65.13N	212.52E	65.31	Sep	1995	256	CRL, UofA
Sanae	Antarctica	70.32S	357.58E	-60.95	Mar	1991	16	PU
Sdr.Strømfjord	Greenland	66.99N	309.05E	73.51	Oct	1989	49	DMI, UofM
South Pole	Antarctica	90.00S	-	-74.10	Jan	1988	49	UofM
Syowa	Antarctica	69.00S	39.35E	-66.45	Feb	1992	64	NIPR
Tjørnes	Iceland	66.20N	342.90E	66.89	Jul	1990	64	NIPR, STEL
Tromsø	Norway	69.70N	19.20E	66.70	planned		800	MPAE
Zhongshan	Antarctica	69.37S	76.38E	-74.69	planned		64	NIPR, PRIC

Table 4. List of selected operating and planned imaging riometer installations (September 1995).

An imaging riometer installation, typically, has a field of view of approximately 250 x 250 km. For the correlation studies it may be considered a useful case if the orbit (more precisely the projected foot-point) of the satellite is within 100 km of the location of an imaging riometer installation. At the time of the possible launch of the Ørsted satellite there will probably be 10 imaging riometer installation in operation. They will be located at magnetic latitudes from 65 to 80°. The probability of a passage within 100 km from one or more of these 10 installation during a full orbit will be approximately 20%.

The incoherent scatter radar stations in question, ISR in Sdr. Strømfjord, EISCAT in Tromsø, and ESR in Longyearbyen, are all co-located with imaging riometer installations (cf. Table 4). The radar installations have a larger range than the riometers, typically 1000 x 1000 km. Hence a close encounter for initiating very-high-speed CPD operation should be larger, for instance 300 km. The radars, however, are operated on a campaign basis so their availability should be checked.

As a crude estimate there will be some absorption observable during 10-20% of total time. Events of particular interest may occur during 1-2% of the time. From these criteria 1 of every 30 orbits (one every other day) would be of great interest and only 1 of every 500 orbits (two events each month) would be of particular interest for correlation studies. Thus it is important that every possible case is sampled.

4. Data processing.

For the Charged Particle Detector experiment the raw data will be counts referring to some integration time interval and defined from detector impulse amplitudes. The output data wanted from the experiment are intensities of particle fluxes as functions of particle type, particle energy and particle pitch angle. Some degree of uncertainty in the derivation of these values must be expected. We attemt to learn as much as possible from previous experiences in data handling procedures and algoritms. Aspects to consider are a.o.:

- particle identification (electr., protons, α-particles)
- energy level calibrations
- calculation of angular distributions
- subtraction of background
- detector dead-time corrections
- pulse pile-up effects
- detector noise effects

There will probably be developed several levels of detector calibrations and corrections. A relatively simple procedure should be made available as a default procedure. Other more complicated procedures based on actual values of the house-keeping data, on correlations between the detectors and possibly also on judgements of the geophysical situation, e.g. whether a solar flare is in progress, should be developed.

The auxillary values needed for the data presentation will be the primary parameters:

- UT time
- Geographic latitude and longitude (and altitude)
- Satellite attitude (polar and azimuthal angles)
- Housekeeping data

From these values a set of secondary parameters should be derived a.o.:

Appendix B

Summary of the Ørsted satellite mission

Summary of the Ørsted satellite mission

The main purpose of the Ørsted satellite is to provide a precise global mapping of the Earth's magnetic field. Provisionally collection of data is planned for a period of 14 months. The measurements shall be used to improve the existing models of the Earth's magnetic field and to determine the changes of the field.

Combined with the data from other satellites and from many ground based observatories the measurements from Ørsted will be used in studies of the variations of the magnetic field of the Earth. The variations both of the strong field from inside the Earth and of the weaker, rapidly varying, field resulting from the interaction between the ionised gas streams from the sun (the solar wind) and the Earth's magnetosphere are included in the studies. Furthermore, the transfer of energy from the solar wind to the outer magnetosphere and further down to the lower layers of the atmosphere will be studied. All of these studies will benefit not only from the magnetic field measurements but also from the measurements of the flow of energetic particles around the satellite.

A precise survey of the Earth's magnetic field is of particular interest to the field of geophysical studies. Equivalent measurements have been made only once before, with the US MAGSAT satellite (1979-80). So with the new data from Ørsted it will be possible for the first time ever to obtain a global survey of the changes of the main field. These changes are related to flows inside the Earth's fluid core but the exact mechanisms is not yet known. Geological formations in the Earth's crust can be mapped and characterised by detailed studies of the magnetic maps. Consequently, also geologists have an interest in using the Ørsted data.

Compared to the MAGSAT-mission the Ørsted-project is improved in a number of ways. The accuracy, for example, both of the magnetometers and the star-imager are higher. In addition, the Ørsted orbit will have a different orientation in relation to the direction to the Sun and therefore new information about the global distribution of electric currents in the Earth's magnetosphere will be gained.

Instruments

A total of five scientific instruments are carried onboard the Ørsted satellite. Three of the sensors are mounted on an 8 meter long boom to minimise the disturbances from the electrical systems of the satellite.

CSC Fluxgate Magnetometer to measure the magnetic vector field (strength and direction). This instrument is stable within 0.5 nT over time spans of several days. It has been built at the DTU.

SIM Star-Imager to determine the orientation of the fluxgate magnetometer (and the satellite). It is accurate to less than 5 arc seconds. This instrument has been built at the DTU.

Overhauser Magnetometer to measure the strength of the magnetic field (not direction sensitive). It has an absolute accuracy better than 0.5 nT. The main purpose of this instrument is the calibration to an absolute scale of the measurements of the fluxgate magnetometer. It has been built at LETI in Grenoble and is provided by the French Space Agency, CNES.

The last two of the instruments are placed on the main body of the satellite:

Charged Particle-Detectors (CPD) to measure the flux of fast electrons (0.03-1 MeV), protons (0.2-30 MeV), and α-particles (1-100 MeV) around the satellitte. This instrument has been built at the Danish Meteorological Institute.

Turbo-Rogue GPS Receiver to accurately determine the position of the satellite. During intervals this instrument may be used scientifically to investigate the atmospheric pressure, temperature, and humidity beneath the satellite. It is built at the Jet Propulsion Laboratory in California and is provided by the US National Space Agency, NASA.

Orbit and Operation.

An elliptic orbit of heights between 500 and 850 km and with an orbit period of approx. 100 minutes will be used. The main receiver station is located at DMI in Copenhagen with backup stations at IKT in Ballerup and at AAU in Aalborg. The technical functionality of the satellite is monitored at the Control Centre at CRI. Preliminary data reduction and calibration are performed at the Science Data Centre at DMI.

Participants.

The Ørsted project is undertaken jointly by a number of Danish research and technology institutions and industrial companies.

Research

Danish Meteorological Institute (DMI)
(Solar-Terrestrial Physics Division)
University of Copenhagen (KU)
(Department of Geophysics, The Niels Bohr Institute)
Danish Technical University (DTU)
(Institute of Automation)
Danish Space Research Institute (DRI)
(Department of Solar System Physics)

Technology

University of Aalborg (AAU)
(Institute of Electronic Systems)
The Engineering College of Copenhagen (IKT)
(Department of Electronics)
Danish Technical University (DTU)
(Department of Applied Engineering Design and Production)
(Department of Control and Engineering Design)
(Department of Electromagnetic Systems)

Industry

Computer Resources International A/S (CRI)
Per Udsen Co. A/S (PUC)
Terma Elektronik A/S (TE)
Innovision

International participation

The Ørsted project has attracted much attention within the international research community. An extensive collaboration to explore the scientific data has been established. More than 50 research groups from all parts of the world participate in this project and will be provided access to the data.

The US National Space Agency, NASA, contributes to the Ørsted project with an offer to launch the satellite free of charge together with a large US satellite, ARGOS. They will be launched with a DELTA-II rocket from the Vandenberg Base in California. NASA, in addition, supplies the specially built GPS receiver, the Turbo-Rogue.

The French Space Agency, CNES, supplies the Overhauser magnetometer. The European Space Agency, ESA, has provided technical advice and financial support of the Control Centre at CRI and the Ørsted Science Data Centre at DMI.

Schedule

Assembling and test:	1996-1997
Launch from California:	1997
Operation and data sampling:	1997 to 1998
Data analysis and publications:	1997 to (at least) 2000

H. C. Ørsted (1777-1851)

The first Danish satellite has been named after the Danish physicist, Hans Christian Ørsted, who in 1820 discovered the relationship between electric currents and magnetic fields. Ørsted was active in many fields and, among others, initiated the foundation of "Den Polytekniske Læreanstalt", now the Danish Technical University.

Further information

Homepage: http://www.dmi.dk/projects/oersted/

Appendix C

The Ørsted Satellite

Appendix D

Estimated characteristics of a strongly collimated CPD

D.1 The strongly collimated CPD

The strongly collimated E1 detector is represented in Figure D.1: In this tentative design, the "sliced collimator" was replaced by a massive conical collimator along the whole particle path. The three collimator elements are replaced by a 1.475 *cm* long conical

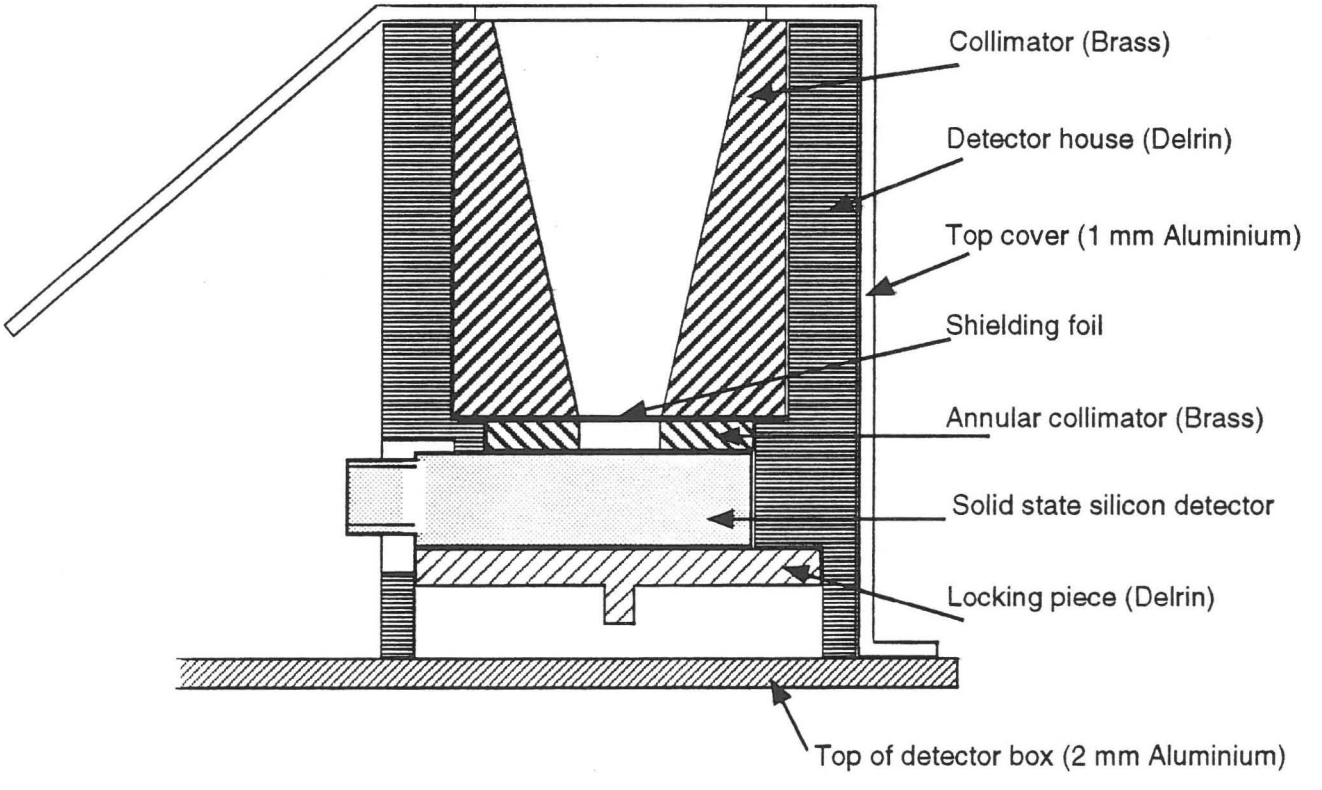

Figure D.1: The strongly collimated CPD detector element E1.

collimator having 0.25 *cm* inner radius at the sensor side, and 0.915 *cm* inner radius at the aperture side. The outer radius at both side is 1.2 *cm*.

The effect of this change was to eliminate all the "false" peaks which resulted from the sliced collimator and replace them by a solid tail of energies deposited by all the particles which hit the conical collimator. This tentative design would greatly improve the unfolding of real data from the raw measurements.

D.2 The detection efficiency of the strongly collimated CPD

By comparison of Figures D.2 to D.7 with Figures 2.11 to 2.16, one can notice that the only changes in the detection efficiency function are that it does not display steep gradients anymore and its values are slightly lower than their actual CPD counterparts. This soft variation leads to more precise results when calculations involving integral and derivative of the efficiency functions are concerned.

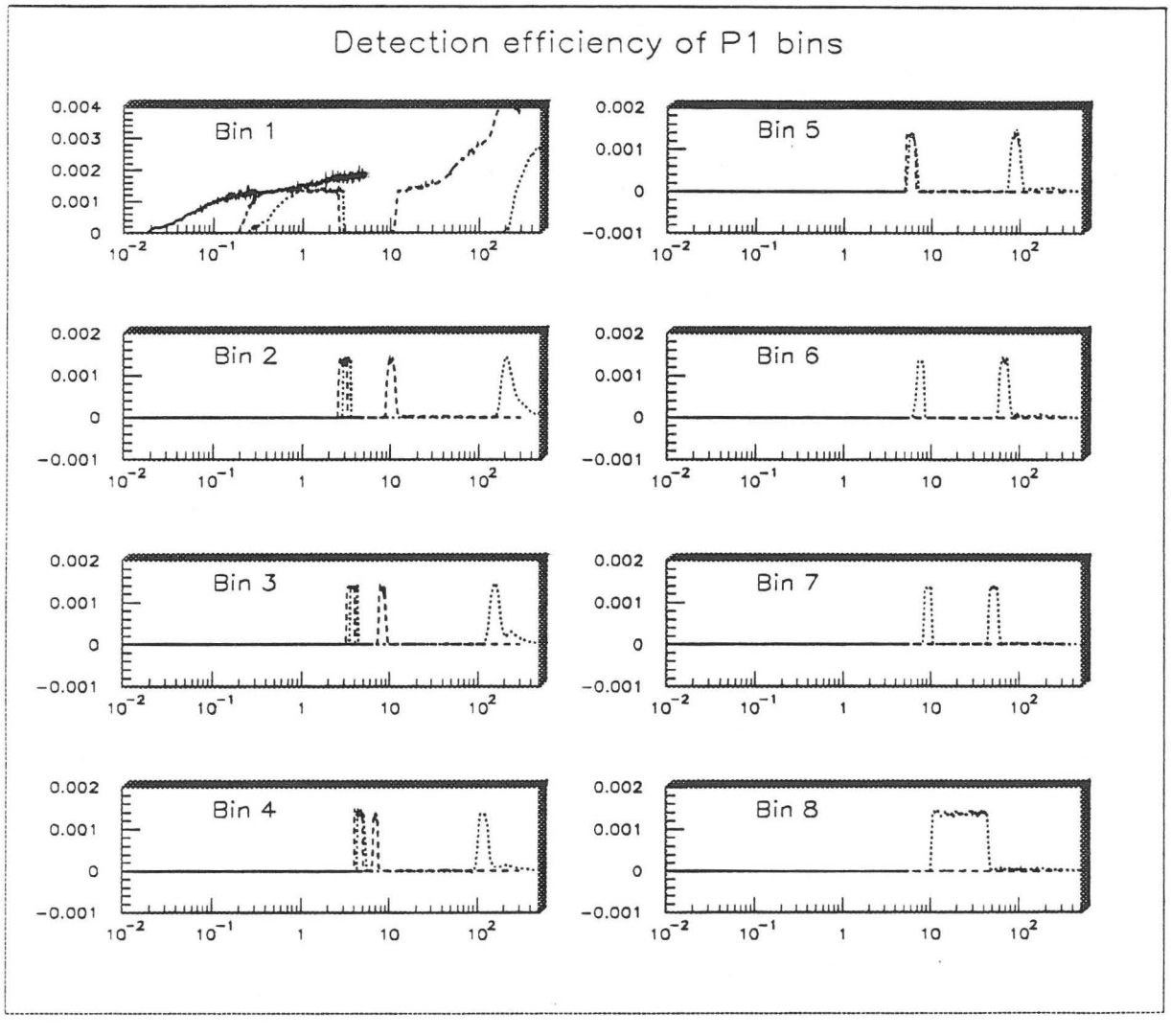

Figure D.2: Detection efficiency of the modified P1 detector subunit, as a function of incident particle energy. Solid, dashed and dotted lines are for electrons, protons and α-particles, respectively. To be compared with Figure 2.11.

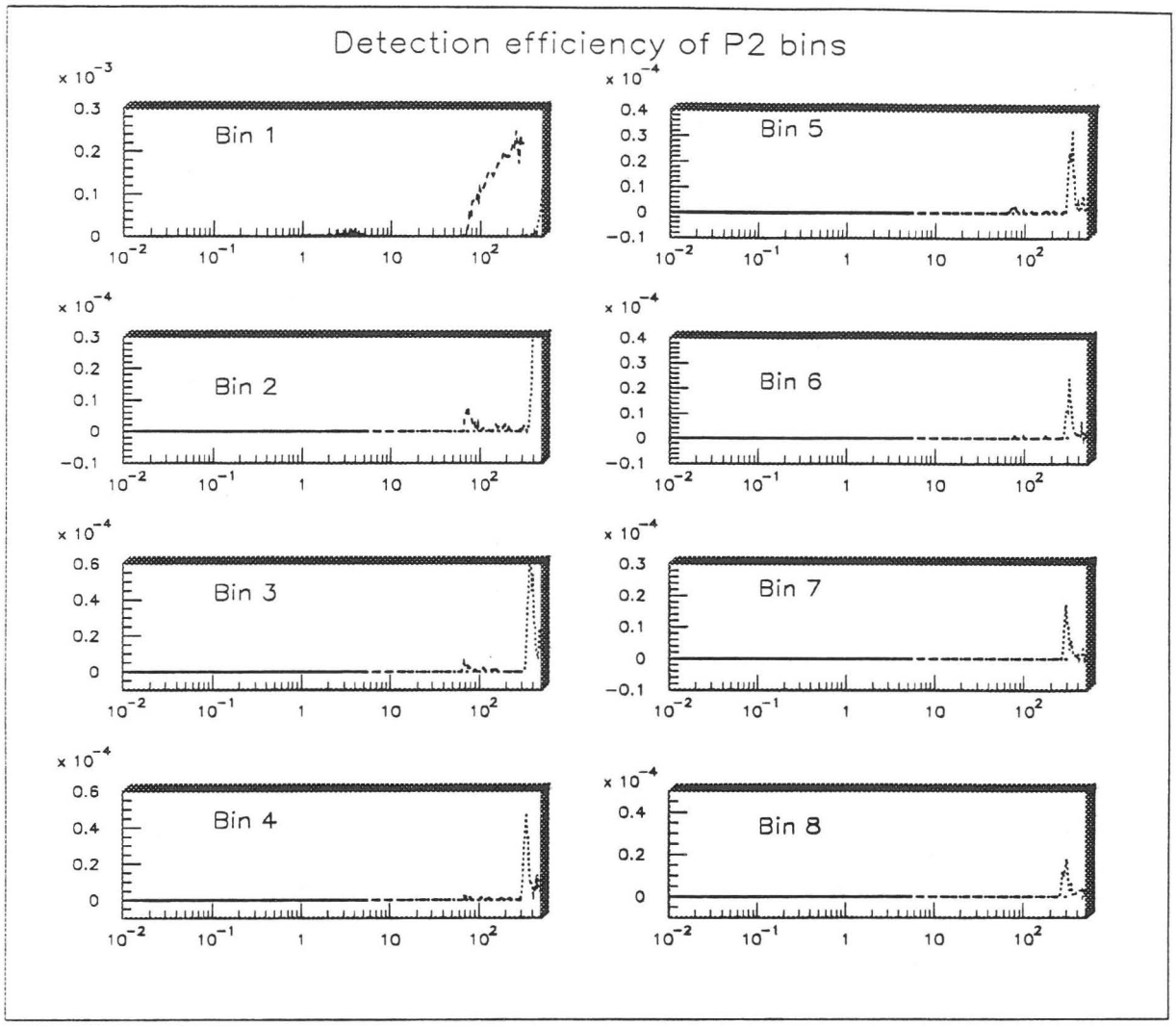

Figure D.3: Detection efficiency of the modified P2 detector subunit, as a function of incident particle energy. All the particles reache the CPD through the up-looking entries. Solid, dashed and dotted lines are for electrons, protons and α-particles, respectively.

D.3 Discrimination features of the strongly collimated CPD

This is done to check whether a modified CPD can better discriminate among particles than the original one. The testing procedure is the same as described above.
Our conclusion is like the same based on the efficiency inspection: no significant improvment is brought by strongly collimating the CPD, provided that the efficiency function is well calculated in both cases.

Model and fit parameters:

Table D.1 contains the input and least squares fit parameters for this case.

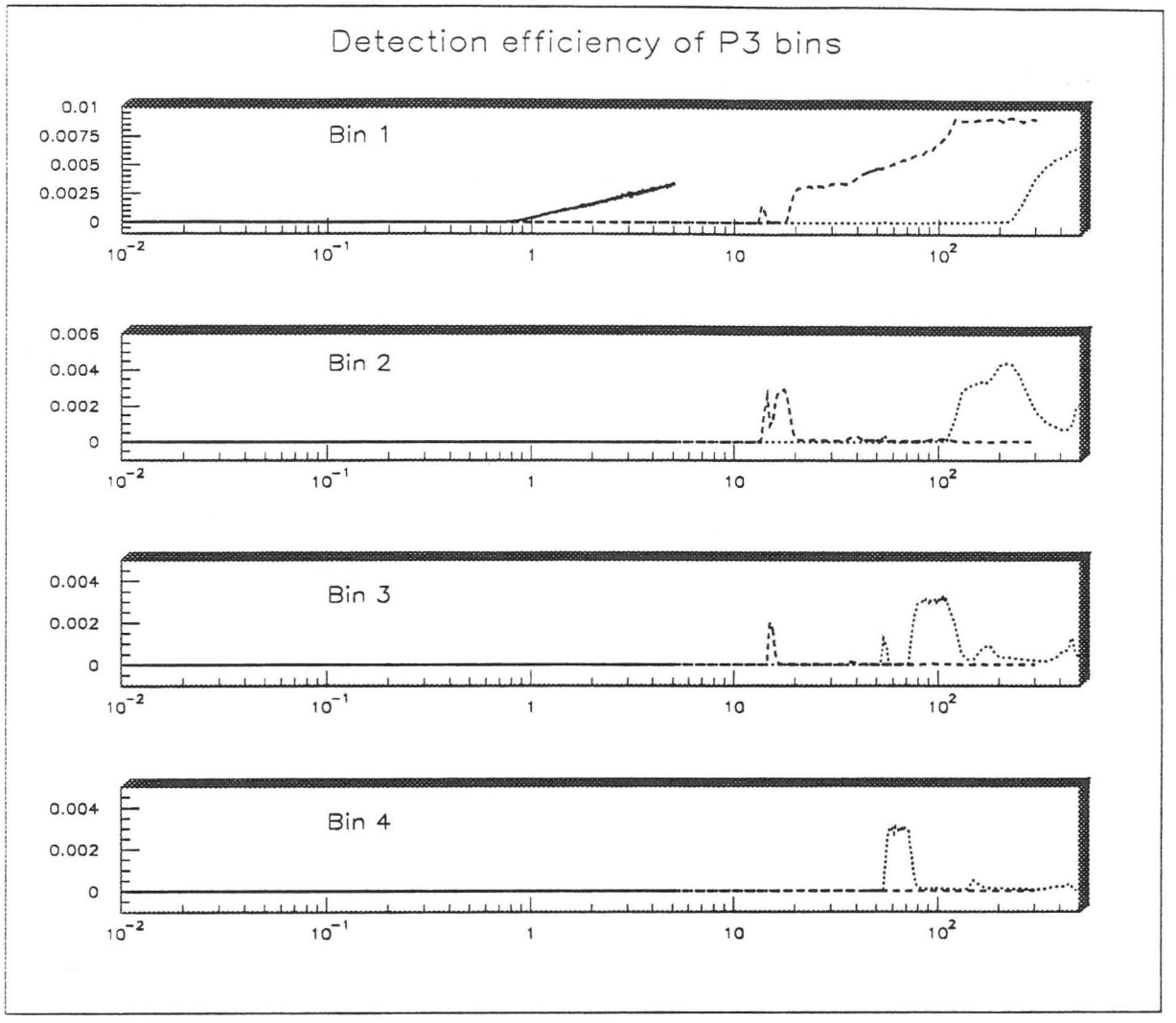

Figure D.4: Detection efficiency of the modified P3 detector subunit, as a function of incident particle energy. Solid, dashed and dotted lines are for electrons, protons and α-particles, respectively.

Calculated and simulated bin counts

Table D.2 contains the count rate obtained by use of Equation 2.2 and by a simulation with GEANT code.

Input/Output spectra

Figure D.8 shows the fit results (dashed line) to compare to input spectrum (smooth line) for the strongly collimated CPD.

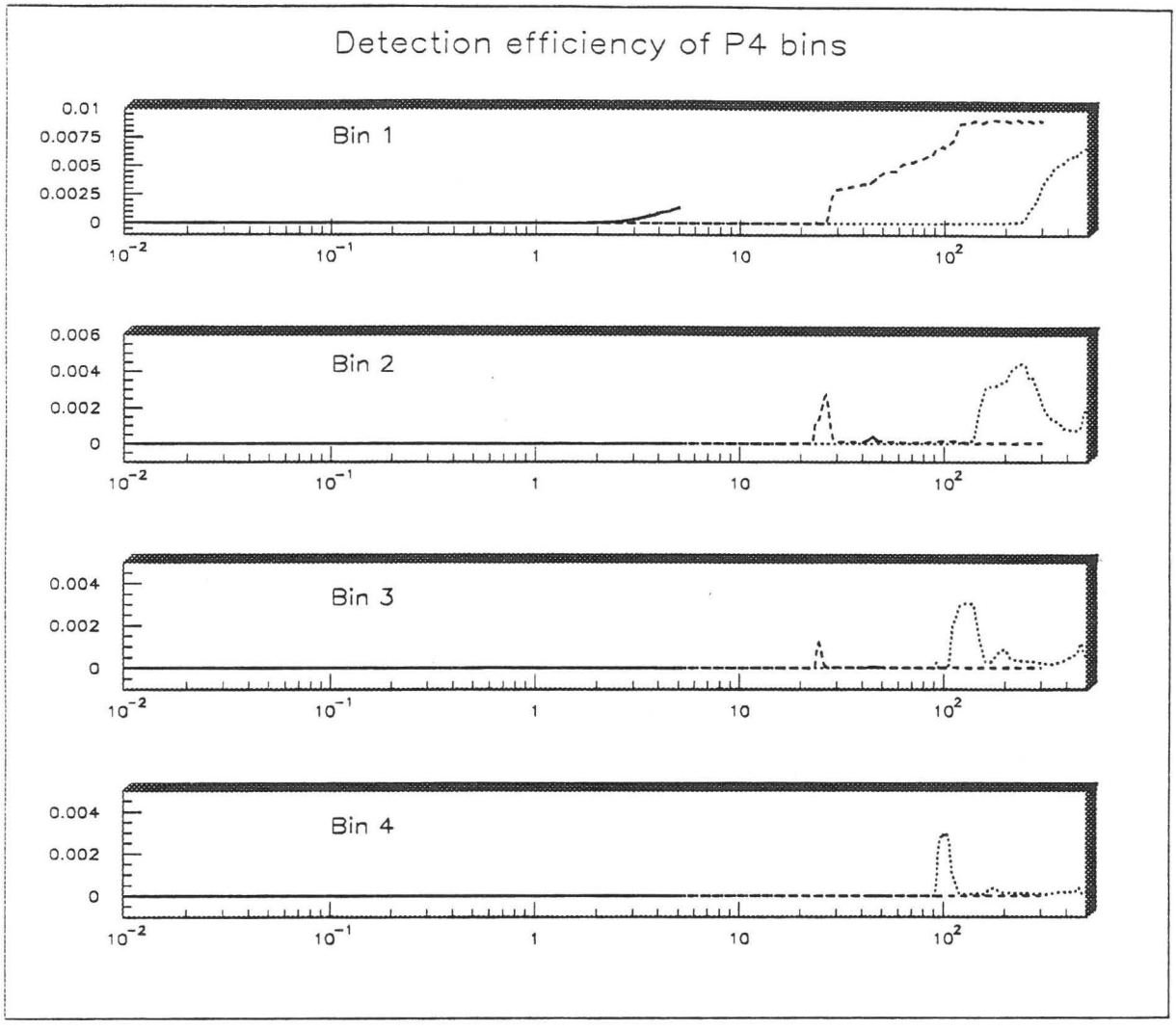

Figure D.5: Detection efficiency of the modified P4 detector subunit, as a function of incident particle energy. Solid, dashed and dotted lines are for electrons, protons and α-particles, respectively.

Particle	C_k $(1/(s\ cm^2\ sr\ (MeV)^{(1-\gamma_k)})$		γ_k		$J^k(E > E_{min})$ $(1/s\ cm^2\ sr)$	
	Model	Fit	Model	Fit	Model	Fit
Electron	13000	15980	1.001	1.144	80911	127452
Proton	9500	7010	1.85	1.76	79035	52955
α	7900	470	2.	2.72	78984	14340

Table D.1: Model and fit parameters for the strongly collimated CPD testing.

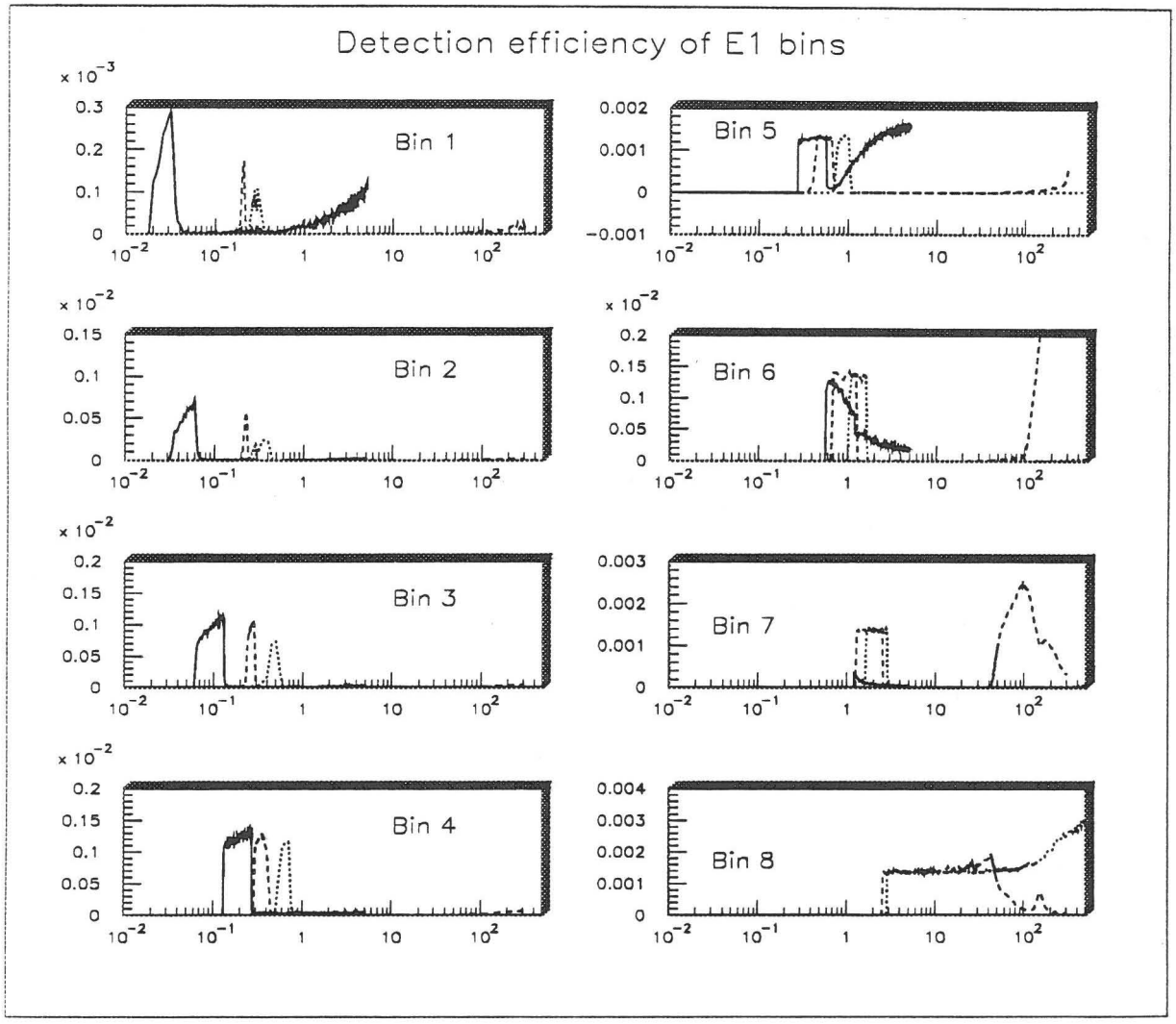

Figure D.6: Detection efficiency of the modified E1 detector subunit, as a function of incident particle energy. Solid, dashed and dotted lines are for electrons, protons and α-particles, respectively.

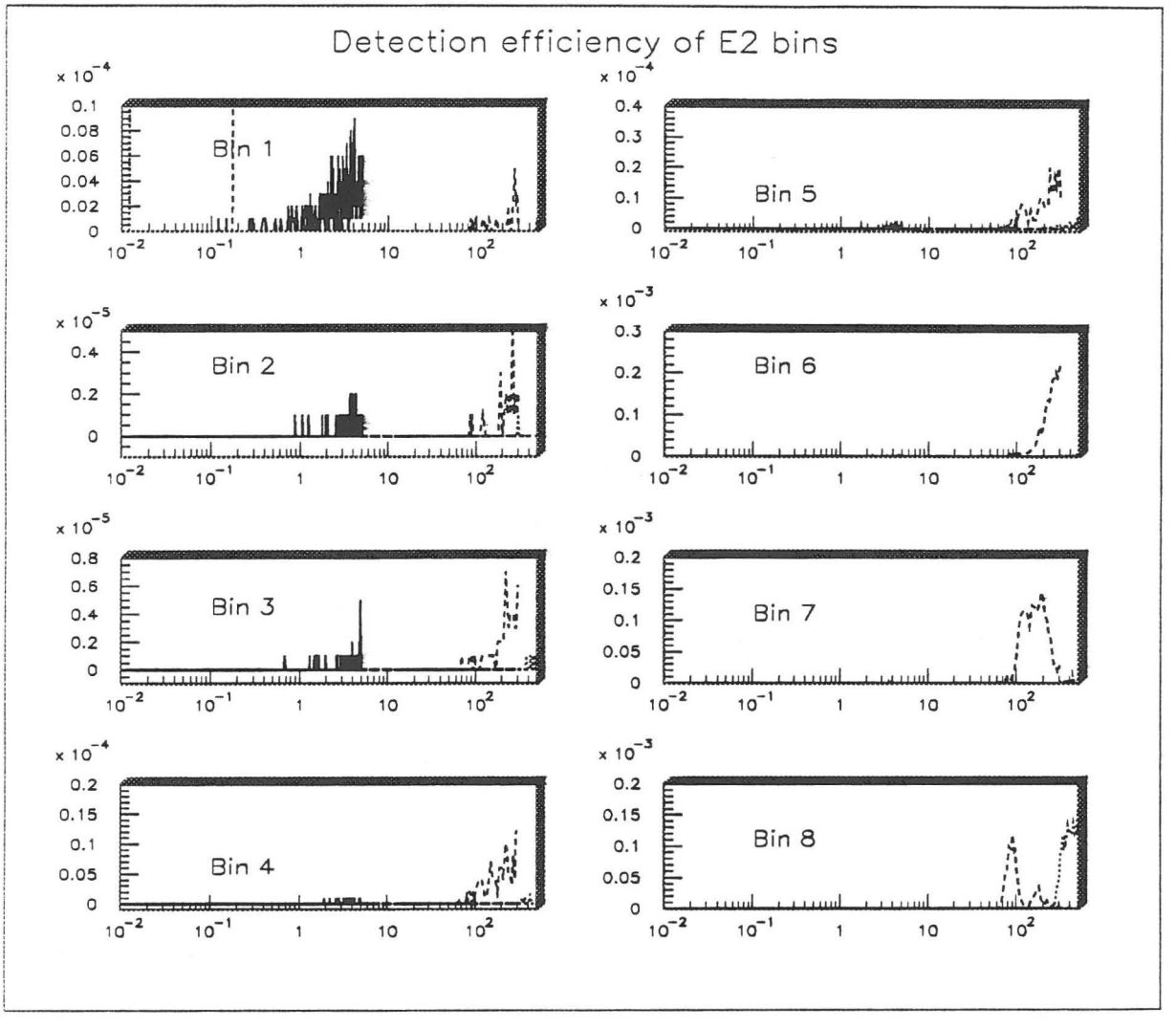

Figure D.7: Detection efficiency of the modified E2 detector subunit, as a function of incident particle energy. All the particles reache the CPD through the up-looking entries. Solid, dashed and dotted lines are for electrons, protons and α-particles, respectively.

Equation 2.2			Simulated		
Detector	Bin	Counts	Detector	Bin	Counts
P1	1	4997	P1	1	4890
	2	59		2	95
	3	66		3	62
	4	55		4	51
	5	40		5	41
	6	12		6	13
	7	10		7	9
	8	26		8	35
P2	1	0	P2	1	1
	2	0		2	0
	3	0		3	0
	4	0		4	0
	5	0		5	0
	6	0		6	0
	7	0		7	0
	8	0		8	0
P3	1	1456	P3	1	1438
	2	27		2	38
	3	10		3	10
	4	3		4	4
P4	1	322	P4	1	304
	2	11		2	15
	3	4		3	6
	4	1		4	1
E1	1	101	E1	1	123
	2	143		2	293
	3	396		3	600
	4	768		4	920
	5	1669		5	1840
	6	818		6	944
	7	342		7	295
	8	345		8	348
E2	1	1	E2	1	2
	2	0		2	0
	3	0		3	1
	4	0		4	0
	5	0		5	0
	6	0		6	1
	7	0		7	0
	8	0		8	0

Table D.2: Calculated and Simulated count rate for the strongly collimated CPD.

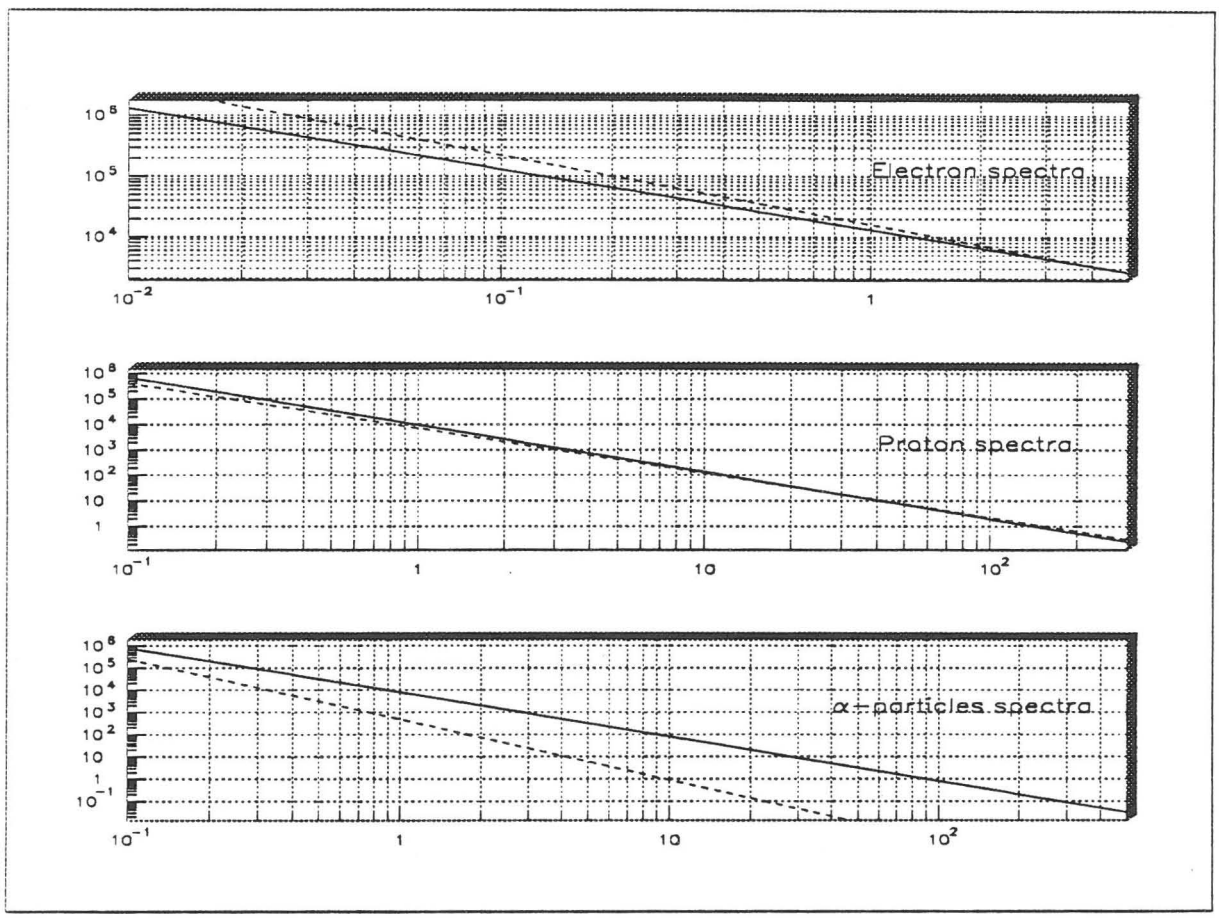

Figure D.8: Comparison between the model spectrum (smooth line) and the least squares fit spectrum (dashed line). The curves represent the probability density function (ordinate) as a function of the particle incident energy (abscissa).